

INFORMATION TO USERS

This manuscript has been reproduced from the microfilm master. UMI films the text directly from the original or copy submitted. Thus, some thesis and dissertation copies are in typewriter face, while others may be from any type of computer printer.

The quality of this reproduction is dependent upon the quality of the copy submitted. Broken or indistinct print, colored or poor quality illustrations and photographs, print bleedthrough, substandard margins, and improper alignment can adversely affect reproduction.

In the unlikely event that the author did not send UMI a complete manuscript and there are missing pages, these will be noted. Also, if unauthorized copyright material had to be removed, a note will indicate the deletion.

Oversize materials (e.g., maps, drawings, charts) are reproduced by sectioning the original, beginning at the upper left-hand corner and continuing from left to right in equal sections with small overlaps. Each original is also photographed in one exposure and is included in reduced form at the back of the book.

Photographs included in the original manuscript have been reproduced xerographically in this copy. Higher quality 6" x 9" black and white photographic prints are available for any photographs or illustrations appearing in this copy for an additional charge. Contact UMI directly to order.

U·M·I

University Microfilms International
A Bell & Howell Information Company
300 North Zeeb Road, Ann Arbor, MI 48106-1346 USA
313/761-4700 800/521-0600

Order Number 9303402

Massive ice interactions with offshore structures

Lu, Mingchi, Ph.D.

University of Alaska Fairbanks, 1992

U·M·I

300 N. Zeeb Rd.
Ann Arbor, MI 48106



MASSIVE ICE INTERACTIONS WITH
OFFSHORE STRUCTURES

A
THESIS

Presented to the Faculty of the University of Alaska
in Partial Fulfillment of the Requirements
for the Degree of

DOCTOR of PHILOSOPHY

By
Mingchi Lu, B.S., M.S.

Fairbanks, Alaska

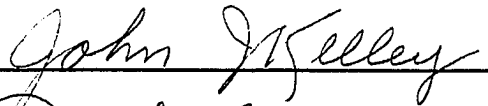
May, 1992

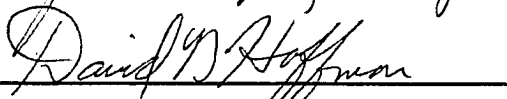
MASSIVE ICE INTERACTIONS WITH
OFFSHORE STRUCTURES

By

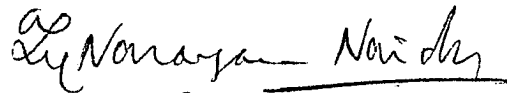
Mingchi Lu

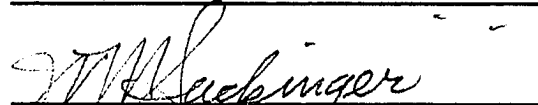
RECOMMENDED:



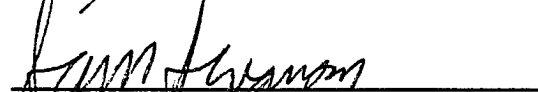








Advisory Committee Chair

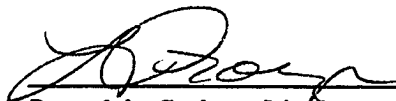


Department Head

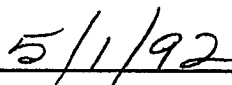
APPROVED:



Dean, College of Natural Science



Dean of the Graduate School



Date

ABSTRACT

The interaction between a multiyear sea ice floe of variable thickness, and an offshore structure, has been examined using a 3-dimensional finite element method. Elastic response within the ice floe was assumed initially, and a uniform loading of the ice floe by the adjacent pack ice was used. As an example of the results for a frozen boundary condition at the ice/structure contact zone, with a central region of the ice floe having its thickness reduced to 50% as compared to the floe thickness at the structure ($\Delta t/t=0.5$), tensile cracks first form at the top surface in the thinnest area of the floe. The total force on the structure was 108 MN, as compared with 1500 MN which would be present in the case of an ice floe of uniform thickness. Parameters varied were ice/structure contact zone (located in the centric or the eccentric region), the sliding boundary condition, two-dimensional ice thickness variation, variable ice elastic modulus as a function of depth, and viscoelastic ice behavior. Cases of rigid and of compliant structure and foundation were included.

In a second part of the study, the ice island loads acting upon a cylindrical rigid structure were analyzed by this 3-dimensional finite element method. A force of 6600 MN was computed to be acting on the structure with a maximum penetration distance of 8.2 m. A different theoretical method based upon multiyear ice field data resulted in a force of 336 MN and a maximum penetration distance of 75 m.

The ice forces on the structure are reduced by ice floe thickness variations, and also are affected by the geometries at the ice floe/structure and ice floe/pack ice boundaries. The reduced elastic modulus in the warmer, lower part of an ice sheet promotes ice bending failure and causes lower structure loads.

TABLE OF CONTENTS

	Page
List of Figures	vii
List of Tables	xiv
Acknowledgments	xvi
1 Introduction	1
1.1 Review of Massive Ice Features	1
1.1.1 <i>Annual Ridges</i>	3
1.1.2 <i>Multi-year Ridges</i>	4
1.1.3 <i>Ice Islands and Icebergs</i>	6
1.1.4 <i>Adjacent, Weaker Ice</i>	8
1.2 Offshore Structure Categories and Features	10
1.2.1 <i>Bottom-Founded Gravity Structures</i>	11
1.2.2 <i>Pile-Foundation Jacket Structures</i>	11
1.2.3 <i>Floating Structures</i>	12
1.3 Environment Driving Forces which Cause Ice-Structure Interactions	13
1.4 Ice/Structure Impacts and Research Emphasis	14
2 Computation Methods	18
2.1 Ice Floe/Structure Interaction Model	18
2.1.1 <i>Ice Floe Model</i>	21
2.1.2 <i>Parameters Used in the Calculations of the Ice Floe Model</i>	25
2.2 Ice Island/Structure Interaction Model	29
2.2.1 <i>Ice Island Model</i>	30
2.2.2 <i>Parameters Used in the Calculations of the Ice Island Model</i>	30
2.3 Mechanical Properties of Multiyear Ice and Failure Criterion	33

2.4	Computation Method	37
3	Stress Analysis of an Ice Floe against a Rigid Structure	41
3.1	Stress Analysis for One-Dimensional Ice Thickness Variation, Ice Structure Contact Zone Located in the Central Region	41
3.1.1	<i>Stress Analysis, Comparison with Two-Dimensional Finite-Element Method, and Experimental Results</i>	41
3.1.2	<i>Localized Maximum Ice Pressure on the Structure, and Load Reduction Factor</i>	43
3.1.3	<i>Deformation of the Ice Floe</i>	49
3.2	Examination of the Ice/structure Contact Zone Located in the Eccentric Region	51
3.3	Examination of the Sliding Boundary Condition	55
3.4	Examination of the Two-dimensional Ice Thickness Variation of $\Delta l/l$	58
3.5	Examination of Variable Elastic Modulus	62
3.6	Examination of the Effect of a Change of $t_1/t = 0.5$	64
3.7	Examination of Viscoelastic Ice Behavior	68
3.8	Results of Comparison by using other Failure Criteria	76
4	Analysis of an Ice Floe Acting against a Compliant Structure	78
4.1	Finite Element Model of the Structure and Foundation	78
4.2	Stress in the Ice Floe and Maximum Force Acting on the Structure	81
4.3	Total Force on the Structure as a Function of the Deformation of the Structure	87
4.4	Deformation of the Foundation	91
5	Analysis of Ice Island Forces on a Cylindrical Structure	98
5.1	Introduction	98

5.2	Theoretical Analysis of the Ice Island Loads Acting upon a Cylindrical Structure	99
5.3	Results for the Ice Island Loads by The Three-Dimensional Finite Element Method	116
6	Conclusions	127
	References	131
	Appendix: Computer Calculation Programs	138

LIST OF FIGURES

Figure		Page
1.1	Massive ice features along the Beaufort Sea coast of the Arctic Ocean	2
1.2	Cross sections through multiyear ice ridges (Kovacs, 1983)	5
2.1	Schematic diagram of a multiyear sea ice floe surrounded by the pack ice and impacting a vertical structure	19
2.2	Sloping-sided structure may present a near vertical face to advancing ice, (a) grounded rubble pile; (b) ice adhesion	20
2.3	Idealized uniformly-loaded multiyear sea ice floe model with a flat top and a one-dimensionally variable bottom in the central region of the floe thickness	22
2.4	Idealized uniformly-loaded multiyear sea ice floe model with a flat top and two-dimensionally variable bottom in the central region of the floe thickness	23
2.5	Two locations of ice/structure contact zone are considered in the calculations: (a) the structure is located in the center region and (b) the structure is located in the eccentric region of the end of the floe	24
2.6	The shear stress as a function of the normal stress in the friction tests of sea ice, from which the friction coefficient is obtained as the slope of the line (Tabata and Tusima, 1981)	26
2.7	(a) The finite element mesh of the ice floe in calculations; (b) arrangement of more meshes in the thinnest area of the floe and enlarged from the circle area in (a)	27
2.8	Schematic diagram of a ice island surrounded by pack ice and impacting a vertical structure	31

2.9	The finite element mesh of the ice island in calculations; more meshes are arranged in the ice island/structure contact zone and in the center region of the ice island to analyze the indentation	32
2.10	Mechanical properties of multiyear ice from Cox and Richter-Menge (1985), and Riska and Frederking (1987). (a) uniaxial compressive strength (Riska and Frederking, 1987); (b) uniaxial tensile strength (Cox and Richter-Menge, 1985)	34
2.11	The failure surface on a plane of principal stress (Riska and Frederking, 1987)	36
2.12	(a) 4-parameter fluid or Burger's model for a viscoelastic material. (b) Maxwell model; for this study the dashpot is assumed to follow Glen's Law, given by the equation (2-4)	38
2.13	Execution sequence of ADINA-IN, ADINA and ADINA-PLOT	39
3.1	Stress ratio (S_r) between the stress in the ice floe and the applied average pack ice compressive stress (P), is a function of x as shown in (c), in which the positions of top, middle and bottom are also defined	42
3.2	S_r distributions on the top surface of the floe; positive value means a tensile stress, which can be seen only in the thinnest area of the floe	44
3.3	Comparison of the results of the three-dimensional finite-element method with the experimental and theoretical results (Hallam et al., 1987), and the two-dimensional finite-element results (Takeuchi and Shapiro, 1989)	45
3.4	Schematic diagram of localized maximum ice pressure computed at the points A and B regions of the ice/structure contact zone, and maximum ice tensile stress computed at points C	46

3.5	Structure load reduction factor (R) as a function of the ice floe thickness irregularity	48
3.6	Deformed meshes of variable thickness and uniform thickness of the ice floe, and the largest displacements computed at the region of ice floe/pack ice zone	50
3.7	The angle of deflection of the ice floe is a function of ice floe thickness reduction ratio, in which the negative value means downward direction of the deflection, corresponding to the conditions of first failure of the ice floe	52
3.8	Schematic diagram of localized maximum ice pressure computed at the points A_1 regions of the ice/structure contact zone, and maximum ice tensile stress computed at points C_1 . Points B_1 show a smaller pressure	54
3.9	Schematic diagram of localized maximum ice pressure computed at the points A_2 regions of the ice/structure contact zone, and maximum ice tensile stress computed at points C_2	56
3.10	Schematic diagram of maximum ice tensile stress computed at points C_3 . Points B_3 show a compressive stress	60
3.11	S_{rm1} and S_{rm2} distributions on the top surface of the floe, for the case of $\Delta l/l = 0.5$. The positive value means a tensile stress, which can be seen only in the thinnest area of the floe	61
3.12	Schematic diagram of localized maximum ice pressure computed at the points A_4 regions of the ice/structure contact zone, and maximum ice tensile stress computed at points C_4	63
3.13	(a) the loading condition was taken as an averaged global pack ice compressive stress; $t_1/t=1$; (b) the loading condition was taken as a	

half thickness of the ice floe for the averaged global pack ice compressive stress; $t_1/t=0.5$	65
3.14 Schematic diagram of localized maximum ice pressure computed at the points A_5 regions of the ice/structure contact zone, and maximum ice compressive stress computed at points B_5 for variable-thickness ice floe	66
3.15 Stress ratio S_r as a function of time in seconds for $\Delta t/t=0.65$ and $t_1/t=0.5$; time step is equal to 200 seconds. S_{rt} is obtained from the top surface of the ice floe, and S_{rb} is obtained from the bottom surface of the ice floe	69
3.16 Strain rate as a function of time for $\Delta t/t = 0.65$ and $t_1/t = 0.5$; time step is equal to 200 seconds. Strain rate was in $Sec.^{-1}$	70
3.17 Stress ratio S_r as a function of strain rate for $\Delta t/t = 0.65$ and $t_1/t = 0.5$; time step is equal to 200 seconds	71
3.18 Stress ratio S_r as a function of time for $\Delta t/t=0.5$ and $t_1/t=0.5$, time step is equal to 200 seconds. S_{rt} is obtained from the top surface of the ice floe, and S_{rb} is obtained from the bottom surface of the ice floe	73
3.19 Strain rate as a function of time for $\Delta t/t = 0.5$ and $t_1/t = 0.5$, time step is equal to 200 seconds. Strain rate was in $sec.^{-1}$	74
3.20 Stress ratio S_r as a function of strain rate for $\Delta t/t = 0.5$ and $t_1/t = 0.5$, time step is equal to 200 seconds	75
4.1 Finite element model of the structure and the foundation	79
4.2 The tensile stress in the ice floe at point C (Figure 4.3) as a function of time for variable thickness of $\Delta t/t=0.5$. Time of fracture of the floe was 3 seconds	82

4.3	Schematic diagram of localized maximum ice pressure computed at the points A and B regions of the ice/structure contact zone, and maximum ice tensile stress computed at points C	83
4.4	The compressive stress in the ice floe at points A and B (Figure 4.3) as a function of time for uniform thickness of $\Delta t/t=0.0$. The time of fracture of the floe was 7.5 seconds	84
4.5	The forces acting on the structure as a function of time for $\Delta t/t=0.5$	85
4.6	The forces acting on the structure as a function of time for $\Delta t/t=0.0$	86
4.7	(a) Ice forces acting on the structure as a function of deformation of the structure for the case of $\Delta t/t=0.5$; (b) displacement of the structure at point D (Figure 4.8) as a function of time	88
4.8	The results of displacements in Figures 4.7 and 4.9 are located at points D in the ice/structure contact zone	89
4.9	(a) Ice forces acting on the structure as a function of deformation of structure for the case of $\Delta t/t=0.0$; (b) displacement of the structure at point D (Figure 4.8) as a function of time	90
4.10	The vertical and horizontal deformation of the foundation for the case of $\Delta t/t=0.5$. The horizontal axis of the figure presents the width of the foundation as shown in Figure 4.1	92
4.11	The vertical and horizontal displacements at point F_1 (Figure 4.8) as a function of time for the case of $\Delta t/t=0.5$, (a) vertical displacement; (b) horizontal displacement	93
4.12	The vertical and horizontal deformation of the foundation for the case of $\Delta t/t=0.0$. The horizontal axis of the figure presents the width of the foundation as shown in Figure 4.1	95

4.13	The vertical and horizontal displacements at point F_1 (Figure 4.8) as a function of time for the case of $\Delta t/t=0.0$, (a) vertical displacement; (b) horizontal displacement	96
5.1	Simplified interaction geometry for analytic model of progressive penetration	100
5.2	The penetration distance x as a function of time elapsed t for four different initial speed V_0 of the ice island, in which the mass was from the ice island alone, and the added mass was not taken into account	104
5.3	The speed of the ice island $V(t)$ as a function of the penetration distance x , and as a function of the time elapsed t	105
5.4	Geometry for added mass calculation (Marcellus and Morrison, 1982)	107
5.5	The penetration distance x as a function of time elapsed t for four different initial speed V_0 of the ice island, in which the added mass was taken into account	109
5.6	The ice island forces as a function of penetration distance x , in which the added mass was not taken into account	110
5.7	The ice island forces as a function of penetration distance x , in which the added mass was taken into account	111
5.8	The ice island forces as a function of time elapsed t , in which the added mass was not taken into account	112
5.9	The ice island forces as a function of time elapsed t , in which the added mass was taken into account	113
5.10	The processes of the formation of the ice powder in the ice island structure contact zone, where the ice failure formed when the ice island impacted the structure	118

5.11	The maximum ice island forces acting on the structure as a function of the maximum penetration distance, in which the final time was 5 seconds	120
5.12	The maximum ice island forces acting on the structure as a function of the maximum penetration distance, in which the final time was 100 seconds	121
5.13	The the penetration distance as a function of time elapsed, in which the final time was 5 seconds	122
5.14	The penetration distance as a function of time elapsed, in which the final time was 100 seconds	123
5.15	The maximum force of 6600 MN reached by one typical run of the program for the final time of 100 seconds, as a function of time elapsed	125

LIST OF TABLES

Table	Page
2.1	Parameters used in the calculations of the ice floe model. 29
2.2	Parameters used in the calculations of the ice island model. 33
3.1	Applied global pack ice compressive stress P , localized maximum ice pressure, load reduction factor R , and total forces on structure versus $\Delta t/t$, corresponding to the conditions of first ice failure. 49
3.2	Displacements in x , y and z directions, and angle of deflection (θ) (Fig. 3.7) of the floe at point a' (Fig. 3.3) of the floe/pack ice contact zone, corresponding to the conditions of first ice failure. 51
3.3	Results given for the ice/structure contact zone located in the eccentric region of the one end of the ice floe. 53
3.4	Results given by the sliding boundary condition in the ice/structure interface. 57
3.5	Results given by two-dimensional ice thickness variation on stress analysis, in which $\Delta t/t=0.5$ was assumed. 58
3.6	Results given by the loading condition of a change of $t_1/t=0.5$. 67
3.7	Results comparison with two failure criteria. 77
4.1	Parameters used in the calculations for the structure and foundation. E_s and E_f : Young's modulus of the structure and foundation; ν_s and ν_f : Poisson's ratio of the structure and foundation; M_s and M_f : mass density of the structure and the foundation 80
5.1	Results for the maximum force, the maximum penetration distance and maximum time elapsed for the ice island model of $3 \text{ km} \times 2.5 \text{ km} \times 20 \text{ m}$. 114

5.2 Results for the maximum force, the maximum penetration distance and maximum elapsed time for the ice island model of 2.5 km × 2.0 km × 15 m.

115

ACKNOWLEDGEMENTS

I would like to express my sincere appreciation to Prof. William M. Sackinger, my advisor and chairman of the thesis advisory committee, for his advice, encouragement and support. I especially want to thank the members of the advisory committee, Prof. J. Kelley, Prof. D. Hoffman, Prof. S. Li and Prof. H. Tanaka for their guidance and encouragement. Thanks are also extended to Dr. Martin O. Jeffries, and Messrs. T. Takeuchi, Hu Yongxiang and Fei Tong for their advice and help on the research and computer program.

I deeply thank all my family, my father and mother, for their encouragement and support throughout my graduate studies. A special thanks is expressed to my wife, Shen Yan and my daughter, Lu Lu, for their support during this investigation.

The research was funded by the Geophysical Institute, University of Alaska, Fairbanks, which is gratefully appreciated.

CHAPTER 1

Introduction

Sea ice forces on offshore structures are the dominant design loads for ocean oil drilling platforms under most Arctic conditions. The stress analysis of multiyear sea ice, with an irregular thickness, and ice island of uniform thickness, as they contact offshore structures, are the main concerns in this study. Therefore, it is necessary to describe: (1) the massive ice features in the Arctic Ocean, (2) offshore structure categories, (3) environment driving forces causing ice-structure interaction, and (4) ice/structure impacts and research emphasis, in this first chapter.

1.1 Review of Massive Ice Features

Massive ice features have been studied by many researchers (Kovacs, 1983; Sackinger and Stringer, 1983; Sinha, 1983a, 1983b; Weeks and Mellor, 1984; Sackinger, 1985; Ashby and Duval, 1985; Ashby and Hallam, 1986; Hallam, 1986; Mellor, 1986; Weeks and Ackley, 1986; Hallam and Nadreau, 1987; Sanderson, 1988), including data on physical size, ice type, and small-sample mechanical properties. The sea ice characteristics in the Arctic Ocean are schematically shown in Figure 1.1 as described by Gerwick and Sakhuja (1985). Offshore structures deployed in any portion of the Arctic Ocean must be designed and operated to withstand forces generated by: i) interaction of the structure with multiyear ice features, and ii) rare ice features, such as ice floes and ice island fragments. The following section gives a description of these ice features.

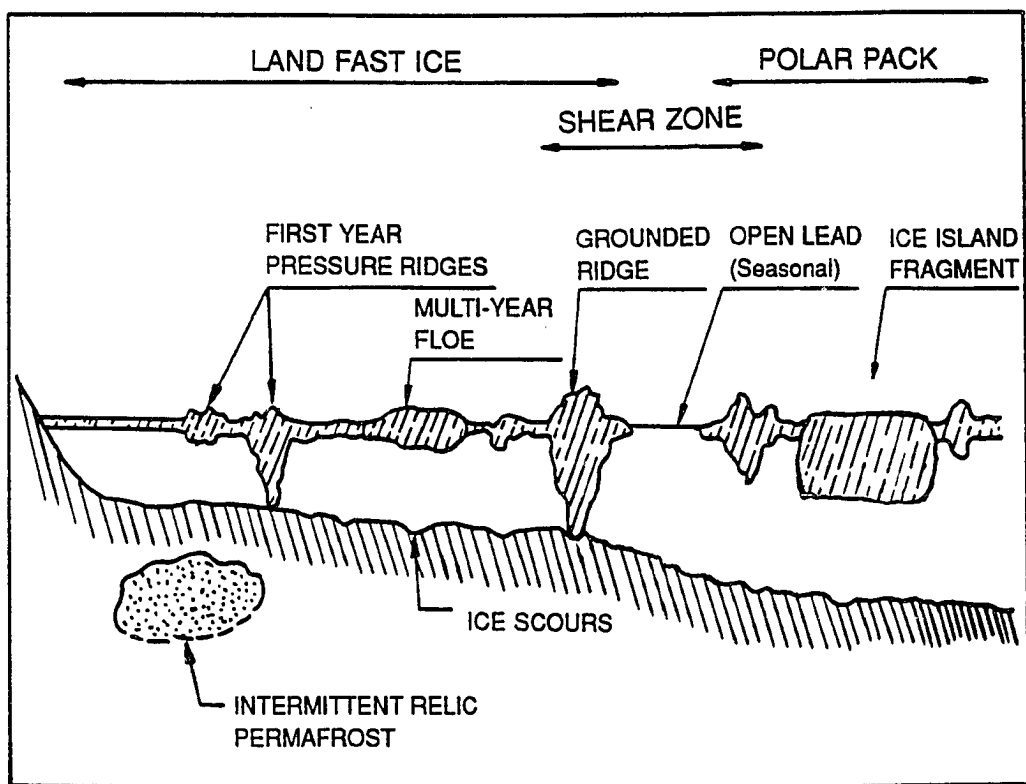


Fig. 1.1. Massive ice features along the Beaufort Sea coast of the Arctic Ocean.

1.1.1 Annual Ridges

Annual ice ridges result from compressional and shearing motions between adjacent annual ice floes, and also at structures or at coastal boundary regions. Annual ice generally has a thickness of up to 2.5 m (Sanderson, 1988). Under dynamic environmental conditions, ice action often occurs and this leads to fracture, ridging and rafting (Sanderson, 1988).

A compression ridge may take place at the boundary of two plates already separated by the growth of tensile cracks. A ridge is formed as two sheets of ice are driven towards each other, by a process of crushing and flexural failure, and is generally highly irregular in direction and in height. Ridges have surface *sails* above sea level and underwater *keels* below sea level.

The magnitude of the sail and keel in a ridge is a function of the thickness of the ice from which the ridge formed, and of the amount of ice which was failed during formation of the ridge. The forces required to form a ridge involve a combination of forces required physically to fracture the ice and forces required to uplift or down-thrust the resulting blocks against the forces of gravity and buoyancy (Parmerter and Coon, 1972).

A shear ridge is formed by left or right lateral movement. It is normally strikingly straight, since the process of shear tends to remove boundary zone irregularity. Shear ridges may be several kilometers long and generally have near-vertical walls consisting of finely-pulverised ice. They are rarer than compression ridges. A shear ridge may form either from relative movement of two separated sheets of ice, or conceivably from a compression ridge if the direction of relative motion changes after initial formation (Sanderson, 1988).

1.1.2 Multi-year Ridges

Multi-year ridges are annual ridges which have survived one or more summer melt seasons. Multi-year ice is formed in the second year, and may be subject to intermittent dynamic action, as well as summer melting and refreezing. New ridges may be formed by compressive stresses, while old ridges become smoothed by melt action into surface hummocks. Multi-year ice is fresher (lower salinity) than first-year ice since brine inclusions have drained due to gravity during the summer warming processes. Surface melt pools collect in depressions and may drain away, or if not, will refreeze in the following winter season; and if the winter season is cool enough and the ice thin enough, continuing additional freezing would occur at the bottom surface of thin multiyear ice (Sanderson, 1988).

“Multi-year ice in the Arctic generally is thought to reach an equilibrium thickness of about 2 - 6 m , when annual melting just equals annual freezing” (Sanderson, 1988). Multiyear ice often appears, on close examination of cores, to show a recognisable annual layer structure. Annual refrozen layers formed are generally about 30-50 cm thick, and a typical undeformed floe may contain about 10 annual layers. If the floe has been located in a region of intense dynamic pack conditions, then it would show no stable stratification of annual layers and is likely to display dramatic variations in thickness. Ridges on a multi-year floe may have surface sails of 5 m height or more above sea level and keels of up to 50 m depth below, while on the same floe, thin areas only one or two meters thick may coexist (Sanderson, 1988; Li and Sackinger, 1991).

The horizontal extent of the keel is normally greater than that of the sail, as seen in Figure 1.2, where thin areas of only 2-3 m thickness are encountered on the same floe. An example of a major multi-year ridge offshore of north-west Greenland is described by Sanderson (1988) which showed a distinctive feature in the middle of a multi-year ice floe of estimated average thickness of 6 meters. The

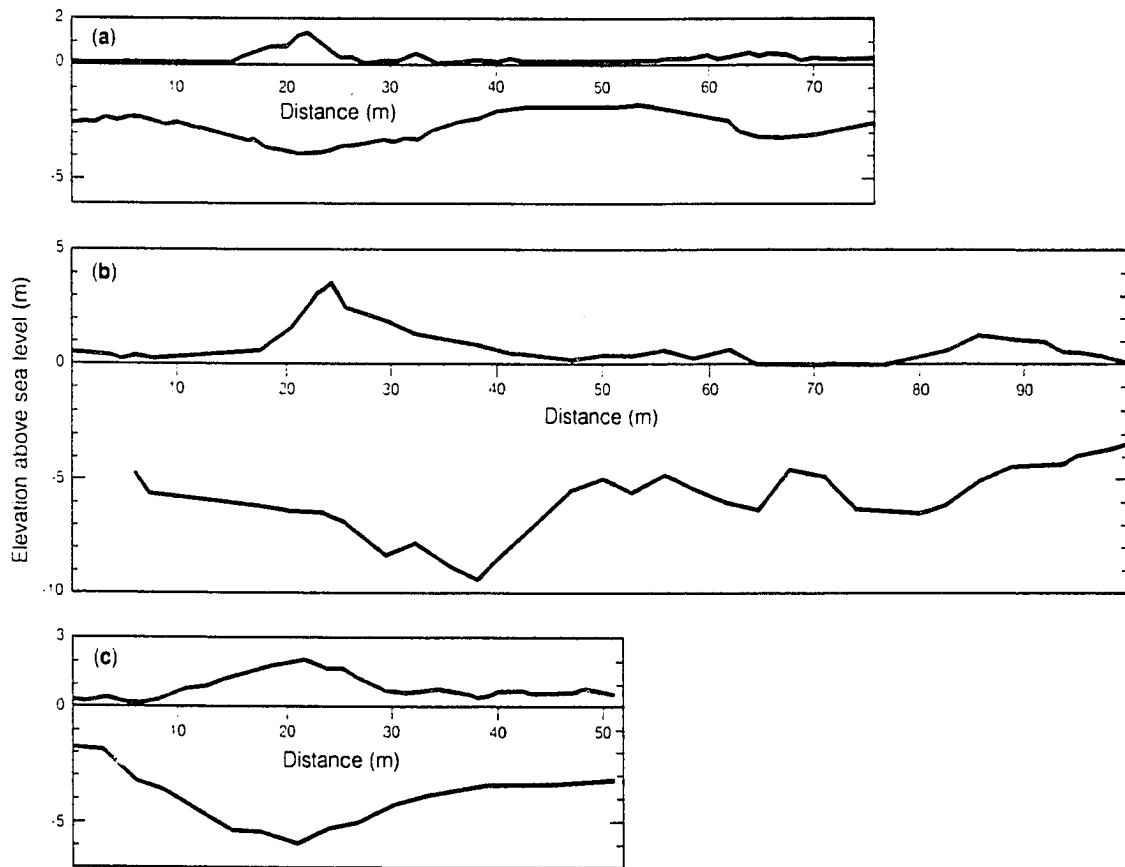


Fig. 1.2. Cross sections through multiyear ice ridges (Kovacs, 1983).

ridge itself had a freeboard of approximately 4 meters, and the depth below sea level was estimated to be 12-15 meters. As a general rule, studies in the Beaufort Sea and Chukchi Sea have shown that the depth of the keel is approximately 3.3 times the height of the sail above sea level (Kovacs, 1983; Sanderson, 1988).

1.1.3 Ice Islands and Icebergs

Ice islands and icebergs are formed by calving of glaciers and floating ice shelves. Icebergs are sometimes approximately cubical (diameter to thickness ratio of between 1:1 and 1:2); these are referred to as blocky icebergs. Another type of iceberg is the tabular iceberg, which has a length-to-thickness ratio of up to 10:1 (produced by calving from a glacier). Icebergs may last for several years, and they undergo major melting at their lower and upper surfaces as they drift into warmer waters and higher air temperatures. Two further classifications of icebergs are divided by the melt process: *dome* icebergs and *drydock* icebergs. A *dome* iceberg is generally formed by immersed surfaces melting so severely that the iceberg becomes unstable and inverts, exposing rounded, smoothly-melted surfaces. A *drydock* iceberg is heavily eroded at the upper surface by sun and wind, and generally exhibits peaks and a highly irregular spikey surface (Sanderson, 1988).

The tip of the iceberg can only be seen above the sea level; most parts of the iceberg lie beneath the surface. The draft and underwater shape of an iceberg is difficult to predict. The forces acting on the icebergs are difficult to analyze, too, as compared with the forces acting on a floe of sea ice. A large floe of sea ice experiences wind drag at its upper surface and current drag at its lower surface, and the drag forces involved are essentially proportional to the surface area of the floe. Because the floe is very large, edge effects are often ignored and the area available for drag is the same at the upper surface as at the lower surface. In contrast, the drift of an iceberg (especially a blocky one) is dominated by edge effects, because

its submerged sides present a very considerable area to the effects of current. The movement of an iceberg is generally determined by local sea currents in the top 100-200 m of the sea, but is also affected by wind conditions (Sanderson, 1988).

Ice islands are also called tabular icebergs, but they are large ice masses, the largest ice features in the Arctic Ocean, and have been observed with thicknesses of up to 60 m and lateral dimensions of up to approximately $40 \times 40 \text{ km}^2$.

Ice islands are composed of low salinity ice with a correspondingly-high compressive strength as compared to sea ice. They originate by calving from the ice shelves of northern Ellesmere Island and Axel Heiberg Island. They are carried along the coast of the Canadian Archipelago by sporadic reversals of the natural circulation of the winds of the Beaufort Gyre, then continue to circulate in the Beaufort Gyre until entering the transpolar drift stream, emerging soon thereafter from the Fram Strait into the North Atlantic (Sackinger and Jeffries, 1986).

The largest of the ice islands produced during the 1983 calving from the Ward Hunt Ice Shelf was called Hobson's Choice Ice Island, which is roughly rectangular in shape, has a surface area of 26.0 km^2 , a mean thickness of 42.5 m, and a mass of approximately $7.0 \times 10^{11} \text{ kg}$ (Jeffries et al., 1988). In the examination of the trajectories of Hobson's Ice Island (Yan, 1986), three different classes of movements were noted. These were large movements (10 km/day typically) in the southwest direction along the coastline; moderate movements (1 - 10 km/day) in two sequentially opposite directions along the coastline, and small ($< 1 \text{ km/day}$) random movements in any direction. These random small movements may have been random positioning errors, or also possibly the result of small tidally-driven movements.

Ice islands have been drifting in the Arctic Ocean and may subject future offshore oil production platforms to a large environmental lateral force. Such ice islands are relatively rare in comparison with multi-year ice; however, they are

potentially more dangerous if encountering a structure. It is desirable to take ice islands into account in future offshore engineering developments in the Arctic regions.

1.1.4 Adjacent, Weaker Ice

The extreme thickness variations are presented from the cross sections of multi-year ridges (Figure 1.2). Multi-year ice meltponds form in summer on top of the ice from meltwater from adjacent ridges. This meltpond region absorbs sunlight efficiently (Maykut, 1986) and causes thinner ice to exist between the multi-year ridges. Such a region is of low strength, and limits the forces transmitted to offshore structures by multi-year ice.

For an ice island, the shelf ice thickness can be much larger than the thickness of sea ice thickness attached to the shelf ice. The sea ice is of two types, multiyear landfast sea ice (MLSI) and multiyear pack ice (MYPI). Jeffries and Sackinger (1989) assume that the MLSI is about 20 years old, as much as 10 m thick, and comprises fresh, brackish, and sea ice layers. The MYPI is composed of consolidated ice rubble and floes welded together by refreezing meltwater, and is estimated to be 5-6 m thick (Jeffries and Sackinger, 1989). Because of the greater water drag of an ice island, due to its deep keel of as much as 40 meters, and also because of the large Coriolis force on the moving ice island resulting from its great mass per unit area, there is a differential velocity between pack ice and an ice island. Tension events, new ice in adjacent leads, and frequent ridge-building along the ice island boundary are probably responsible for the formation of the MYPI.

The MLSI and MYPI are considered to be integral parts of old, drifting ice islands and they may remain attached to the shelf ice component. In 1984 an MLSI floe of about 12 km length and about 5 km width broke out of Yelverton

Bay just west of the Milne Ice Shelf. Yelverton Bay remains a potential source of many such MLSI floes. These thick floes are most hazardous to offshore structures in water depths as shallow as 10 meters. After one circuit of the Beaufort Gyre, however, thinning of these floes reduces their thickness to a value closer to the average multiyear pack ice thickness (Sackinger et al., 1991).

Four categories of features of sea ice are discussed above. Specific conditions of the environment affect engineering choices. Annual ice of thickness 1-2 meters, ridges to heights of perhaps 23 meters and depths of 25 meters all may be found near shorelines and fixed structures. The moving ice exerts substantial lateral force on fixed structures; multiyear ice has been detected with keel depths to 47 meters (Lyon, 1967). The deepest keels of multiyear ridges so far observed in the Arctic have been up to 50 meters. One parameter which has often been used to calculate forces on structures in regions of multiyear ice is the thickness distribution of multiyear ridge keels (Sackinger, 1985). Of considerable interest is the consolidated thickness of the old multiyear ridge keel. Consolidation involves summer melting of ice in the ridge sails, the water from which drains down into the ridge core until it reaches the ocean surface where negative temperatures prevail and refreezing takes place. The spaces and channels available for draining the meltwater into the ridge core gradually close themselves by this refreezing, and there is a limiting depth of consolidation in a very old multiyear ridge, below which there may be only a very gradual formation of thin layers of new ice. Data presented by Kovacs (1983) show that this takes place at a depth of 5.5 to 7 meters, while additional data (Voelker et al., 1981) shows this at a depth of 5 to 12 meters. On the basis of some 28 ridges, it appears that a maximum consolidated ice thickness of 12 meters is a reasonable preliminary value for purposes of structure design (Sackinger, 1985). Finally, the thickest category of ice hazard is the ice island, at 45 to 50 meters

thickness. Large ice islands (9 to 35 km in length) are released only infrequently. As they progress around the Arctic Ocean, there is a finite probability that they will interact with a fixed offshore structure. A computer simulation of ice island movement in the Arctic Ocean was conducted by Li and Sackinger (1991), in which a total of 776 ice island trajectories were used, over a generation interval of 1000 years. Two basic patterns of ice island trajectories can be seen from these random trajectories. The first pattern is a short trajectory near the northern side of Axel Heiberg and Ellesmere Islands, directed to an ejecting route at north Greenland or Nares Strait, which is only about 14% probable. The second pattern is the clockwise circulation or gyre pattern, in a large scale, covering the Beaufort Sea. Most ice island trajectories are in this pattern, with a frequency of 86%. There is a common character in both trajectory patterns, in which the large-scale trajectories consist of many small loops, either clockwise or anti-clockwise as discussed by Li and Sackinger (1991).

1.2 Offshore Structure Categories and Features

The offshore oil industry's hope of discovery of oil and gas in Arctic regions has resulted in many innovative concepts for offshore structures that may withstand the severe ice environment of the region. Some of them have been constructed, (Tarsiut N-44, constructed in 1981 in 22 meters of water; Single Steel Drilling Caisson (SSDC) at Uviluk P66, in 33 meters of water in 1983; Global Marine Concrete Island Drilling Structure (CIDS), in 1984; and C. R. I. and Molikpaq) (Sanderson, 1988; Gerwick, 1986; Jefferies et al., 1985). Similar ideas would be considered in planning future oil exploration and production structures for the Arctic.

1.2.1 Bottom-Founded Gravity Structures

Bottom-founded gravity structures have a low-pressure foundation system to transmit ice force reactions to the sea floor. They may have vertical walls or sloping walls at sea level. Within the general category of bottom-founded platforms, gravity structures are often used in the exploration phase in shallow water (13 meters to 30 meters) because of their ease of relocation.

Global Marine's Concrete Island Drilling Structure (CIDS) was used in the Alaskan Beaufort Sea, and was first placed on the Exxon Tract northwest of Harrison Bay. It is a typical bottom-founded mobile gravity structure and was installed in 1984. In the same year, another gravity structure, Molikpaq, was also seated on location in the Beaufort sea. Both CIDS and Molikpaq were towed in convoy (Gerwick, 1986).

The caisson-retained island structures are also within the categories of bottom-founded gravity structures, which rely on a sand or gravity berm built up from the sea bed to within some 5 meters of the waterline, which then has placed on it a steel or concrete caisson structure. The caisson provides the principal defence against ice action. The first of these structures to be constructed was Tarsiut N-44, constructed in 1981 in 22 meters of water. (Sanderson, 1988). Some of these structures rely on surrounding rubble piles or artificially created ice pads for protection against ice action (Gerwick, 1986).

1.2.2 Pile-Foundation Jacket Structures

These are bottom-mounted structures, which have a reduced number of legs or perhaps just one cylindrical support at sea level, and are permanently affixed to the sea floor by pilings driven into the seabed. These were the first fixed offshore structures to be built for sea ice conditions (Buslov and Krahl, 1983; Gerwick, 1986).

These structures have been used for many years in Cook Inlet, Alaska. During the mid-1960s, 14 offshore structures were built in Cook Inlet. The structures are fairly conventional, though ice-strengthened, piled steel jacket structures, providing a platform for drilling and oil production operations. The platforms are supported by four cylindrical steel legs, and cross-bracing members are in general confined to levels well below the water line, to avoid problems with build-up of ice rubble. The structures are oriented in such a direction, with respect to the prevailing ice motion in the channel, that in general only two legs are subjected to significant ice interaction (Sanderson, 1988).

Considerable conceptual design effort has been utilized in order to reduce the ice forces. In the Unocal monopod, the narrow column (only one cylindrical support leg) presents a minimum face to the ice and is intended to reduce ice forces acting on the structure. The application of these types of structures for Arctic Ocean locations have been complicated by the extreme ice loads, such as those due to multiyear floes or short heavy ridges. These may be reduced by the narrowness of the structure. Also, the question of the potential problems of dynamic amplification under continuous ice crushing need to be resolved.

1.2.3 Floating Structures

Floating structures may be divided into moored and dynamically-positioned types. For deeper waters, floating structures have been developed, which generally resemble the caisson structures and are built of steel, concrete, or a combination of the two. They may be permanently or temporarily moored with high-capacity anchors. The possibility of using dynamically-positioned vessels in the Arctic has also been considered (Buslov and Krahl, 1983).

A non-typical floating structure is the Kulluk exploratory drilling platform, designed to work in moderate sea ice. It is an inverted cone, so that the ice is

broken and deflected downward. This structure is built of steel and has been deployed in the Canadian Beaufort Sea (Gerwick, 1986).

Floating structures have a limited capability to resist ice forces, set by the design of high-capacity moorings and anchors, since the forces in heavy ice are almost an order of magnitude higher than those experienced from wave forces in such locations as the North Sea (Gerwick, 1986). They may be the most realistic approach for exploration at increased water depths. However, they can be built to withstand loosely-packed ice floes and, under some conditions, can be moved to avoid thick ice features (Buslov and Krahl, 1983).

1.3 Environment Driving Forces which Cause Ice-Structure Interactions

The actual structural design of all arctic offshore projects is dominated by lateral forces from sea ice. Winds, ocean currents and waves are included in environmental driving forces which cause ice-structure interactions. In addition, motions and stresses may be caused by secondary driving forces, such as contact with other ice masses which themselves have been driven by primary environmental driving forces.

Most techniques for calculating ice loads on structures assume that sufficient driving force is available to cause failure of the "design" ice feature as it comes in contact with a structure. Wind and current are the dominant factors influencing motions and forces in the ice field. A boundary layer stress is applied by air flow over the rough top surface of the ice cover. The drag force of wind and current is conventionally expressed in terms of the fluid velocity u_z at a certain standard distance z from the drag surface. Steady-state drag forces are proportional to the square of velocity, and the general expression for the shear stress τ_f due to fluid flow is $\tau_f = \rho_f C_f u_z^2$ where ρ_f is fluid density and C_f is the drag coefficient. The

drag coefficient depends upon the surface roughness of the ice and also on the reference height z at which velocity measurements are taken (Sanderson, 1988).

A wind blowing over the sea generates gravity waves; the pressure fluctuates. Similarly a wind blowing over a continuous ice cover can create flexural-gravity waves (Wadhams, 1986). The ice flexure associated with such waves is normally coupled by the oscillating atmospheric pressure field transmitted into the water column. Theoretical predictions by Mills (1972) suggest that an oscillating atmospheric pressure field can also create ice flexure and coupled wave motion in the elastic ocean foundation of the ice sheet. A result by Wadhams (1986) on the effect of ice in waves shows that for short wavelength waves most of the energy is transported by the ice, while for long wavelength waves most of the energy transport occurs in the water.

For a large ice sheet it may be considered that a geostrophic flow due to sea surface tilt, as discussed by McPhee (1982), provides a shear stress on the submerged portion of the ice. The Coriolis effect acting upon the ice changes the direction of motion of the ice. Particularly for a huge ice mass, the Coriolis force significantly affects the motion of the ice, since the Coriolis force is directed at 90 degrees from the direction of ice movement (Lu, 1988). The environmental driving forces are important for the realistic estimation of the effects of ice floe interaction with structures.

1.4 Ice/Structure Impacts and Research Emphasis

Both theoretical and experimental investigations concerning severe problems associated with ice forces on structures have been addressed by many researchers, which may be divided into studies of vertical structures (Määttänen, 1981; 1983; Bercha et al., 1985; Cox, 1985; Hocking et al., 1985; Sanderson and Child, 1986;

Sanderson, 1984, 1988; Duthinh, 1989; Engelbrektsson, 1989; Johnson and Prodanovic, 1989; Takeuchi and Shapiro, 1989), and sloping structures (Gold, 1977; Frederking, 1980; Croasdale, 1980; Ashton, 1986).

Dynamic ice pressures depend on the velocity of the moving ice, and also may depend substantially on the design and shape of the structure concerned. Important factors are surface slope, ice contact zone stress concentrations, degree of structural dynamic response, and formation of a surrounding rubble pile. For instance, a sloping-side structure is used to fail ice in flexure. Under the correct operating conditions this results in significant reductions in load, especially for relatively thin ice. However, for the sloping-sided structures of both upward-breaking and downward-breaking cones, the possibility exists that ice will fail to clear sufficiently quickly around the structure. So, a vertical-contact or random-angled ice face will be presented to advancing ice, and the global force on the structure may approach that range for a normally expected vertical-walled structure. Thus the purpose of reducing ice loads by making a slope on the structure is not inevitably obtained and large total load may occur on the structure, as in the case of the vertical-walled structure. "The technique of reduction of ice load with a sloping-sided structure, of course, has already been successfully used by the floating Kulluk structure" (Gerwick, 1986).

Furthermore, the interaction dynamics must include the structure dynamic response. Many structures, especially those constructed of steel, show significant dynamic response and vibration when the ice interaction occurs. Ice interaction can lead to short-lived high-amplitude vibrating loads being transmitted to the foundations. This can be especially serious in poor soil conditions where partial local liquefaction may take place (Sanderson, 1988). For analysis of interaction dynamics, an additional complexity is the variation of the strength of ice with strain rate. As a result of this effect, the force exerted by an ice floe on a structure

varies with the relative velocity between the ice floe and the structure, leading to a complicated dynamic interaction.

Ice floe impact can be a governing condition for design of an Arctic offshore structure. A rational analysis of the problem requires that dynamic interaction between the structure and the ice floe be considered, in order to get realistic estimations of ice forces, structure displacements, and foundation deformations.

Many of the vibration responses in analysis of interaction dynamics are not well understood, and many of them are still not analyzed and solved.

Multiyear ice pressure ridges and thick hummock floes or ice islands are the most severe ice formations that Arctic offshore structures will have to resist. It is well known that the thickness of multiyear ice floes is quite variable, as discussed by Kovacs (1983). The ice fails at a particular location when the internal stresses at that location exceed the strength of the interacting ice. Because of the stress variations due to thickness variation, the surface hummocks or the bottom roughness of the ice floes affects ice failure, and a complicated and interested problem is presented, in which the stresses in the thinner ice will be amplified with respect to those in a uniform-thickness ice floe (Hallam et al., 1987; Takeuchi and Shapiro, 1989).

The zone of contact between a massive ice feature and the face of a structure is a zone of stress concentration and progressive ice failure, as well. Ice failure takes place after the stress/strain relationship has progressed beyond the linear elastic region in these zones of stress concentration.

To allow a convenient treatment of the geometry of ice/structure boundaries, fracture zone boundaries, and non-uniform ice thickness, the impacts between a multiyear sea ice floe and a offshore structure have been studied in this thesis. A 3-dimensional finite element computational technique was used to examine the effects of ice floe geometry, boundary conditions, ice properties, and other variables

on the stress which can be transmitted through a floe with either an irregular thickness or a uniform thickness. A time-variable formulation which allows for structure vibration as it interacts with a massive ice feature was also used. Elastic deformation of the structure wall, and viscoelastic deformation of seafloor sediments beneath the structure, were handled by the same finite-element method. The ice island/structure interaction effects upon the ice island loads were also analyzed using both the method of three-dimensional finite-element computation and also a separate theoretical formulation. Practical computation results useful in the consideration of offshore structures design for Arctic Ocean regions are given.

CHAPTER 2

Computation Methods

2.1 Ice Floe/Structure Interaction Model

A multi-year ice floe, driven against a vertical face offshore structure by the pack ice surrounding it, is considered in this study, as schematically shown in Figure 2.1. The use of the vertical structure face is justified, because a sloping structure depends critically on efficient clearing of ice from its sloping side. If a rubble field, floating or grounded, develops around the structure, then the sloping sides of the structure are replaced by random faces of the rubble ice, as described by Sanderson (1988), and as shown in Figure 2.2. The study in this thesis concentrates on a vertical interaction boundary, or a vertical sided structure, to be more exact, as it is considered to be the condition for maximum force on the structure.

The maximum ice force acting on the structure is calculated from the global pack ice compressive stress required to cause the ice to fail somewhere in the floe. This depends on some combination of the uniaxial compressive strength of the ice, the velocity and thickness of the ice floe, the geometry of the ice/structure boundary and other factors. In most maximum ice force calculations presented before, the ice thickness was taken as a constant. However, it is known that the surface underneath multi-year ice is highly irregular due to refreezing of leads, and ridging (Kovacs, 1983), as well as snow drift thickness variations which affect accretion of new ice layers. As one objective of this study, to examine the influence of the bottom roughness of ice sheets on the loads which can be transmitted from ice to offshore structures, the geometric variables of the ice floe models used in the calculations were chosen as follows.

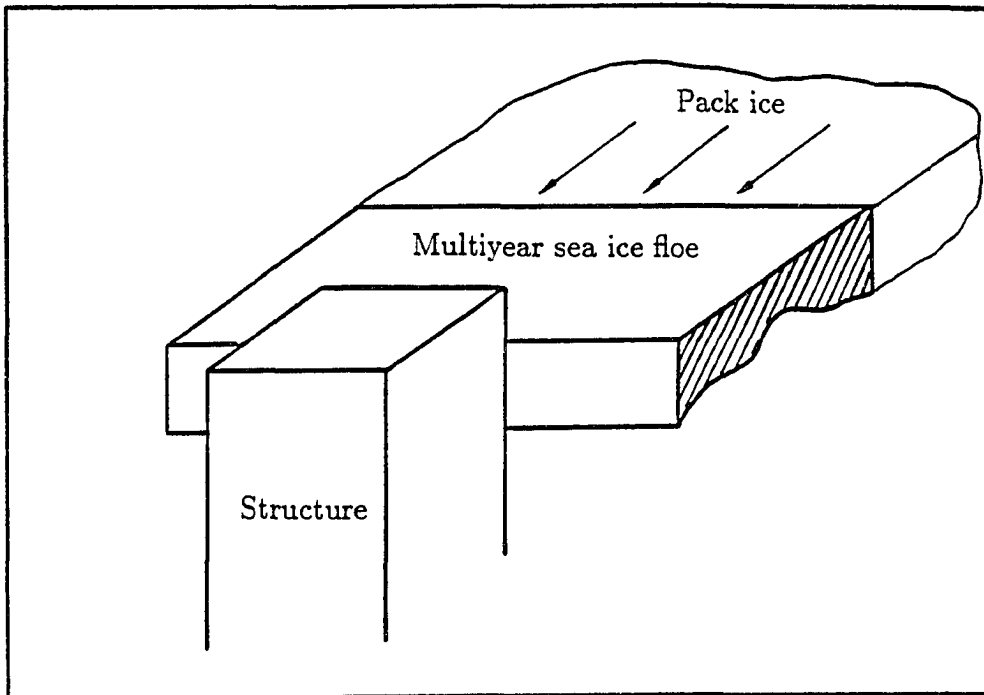
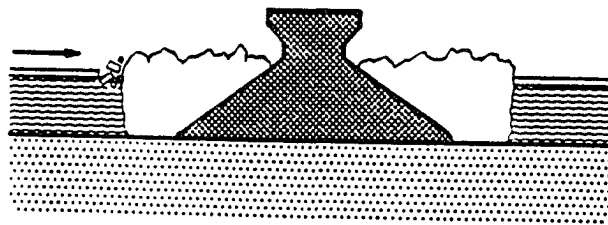
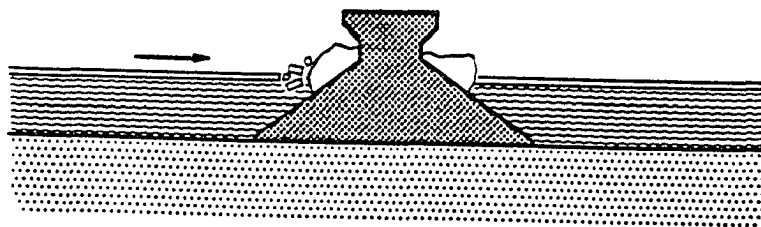


Fig. 2.1. Schematic diagram of a multiyear sea ice floe surrounded by the pack ice and impacting a vertical structure.



(a)



(b)

Fig. 2.2. Sloping-sided structure may present a near vertical face to advancing ice, (a) grounded rubble pile; (b) ice adhesion.

2.1.1 Ice Floe Model

From a basic ice/structure interaction model as shown in Figure 2.1, the multi-year ice floe was assumed to be a 50 m by 50 m square. The floe was an elastic or viscoelastic solid with a flat top and a variable bottom, resting on an elastic foundation as shown in Figure 2.3 and 2.4. The maximum thickness of the ice floe was taken as 6 m. In Figure 2.3, the magnitude of the thickness variation in one-dimension was expressed as the ratio $\Delta t/t$. In Figure 2.4, the amplitude of the thickness variation in two-dimensions was expressed as the ratio $\Delta l/l$, in which $\Delta t/t$ is taken as 0.5. The loading condition in the calculations is the averaged global pack ice compressive stress (P), in which $t_1/t=0.5$ and $t_1/t=1$ were used to examine the pattern of the eccentric loading of the free end of the ice floe.

The width of the structure was taken as 25 m. Two positions of the ice/structure contact interface were analyzed. First, the structure was located in the center region of the end of the ice floe, and secondly, it was located in the eccentric region, as shown in Figure 2.5. Two different boundary conditions at the ice/structure interface were analyzed: A fixed, adfreeze-bonded interface with the rigid structure, and a sliding boundary condition at the rigid structure. Two friction models are available in ADINA, the computer program which is described in detail in Paragraph 2.4 below. These are frictionless, and infinite friction. The friction law selected is satisfied in a global sense over each individual contactor segment. The conditions of tension release, sliding (when the friction coefficient, $\mu = 0$) or sticking (when $\mu=\infty$) for every segment in the contact region is determined during each iteration. In this study, the sliding condition with the friction coefficient of $\mu=0$ was considered in many cases. Tabata and Tusima (1981) presented results showing that the friction coefficients between sea ice and marine structures depend upon the roughness of the structure coating materials. Most of the materials show friction coefficients with sea ice ranging from 0.017 to 0.046. The materials

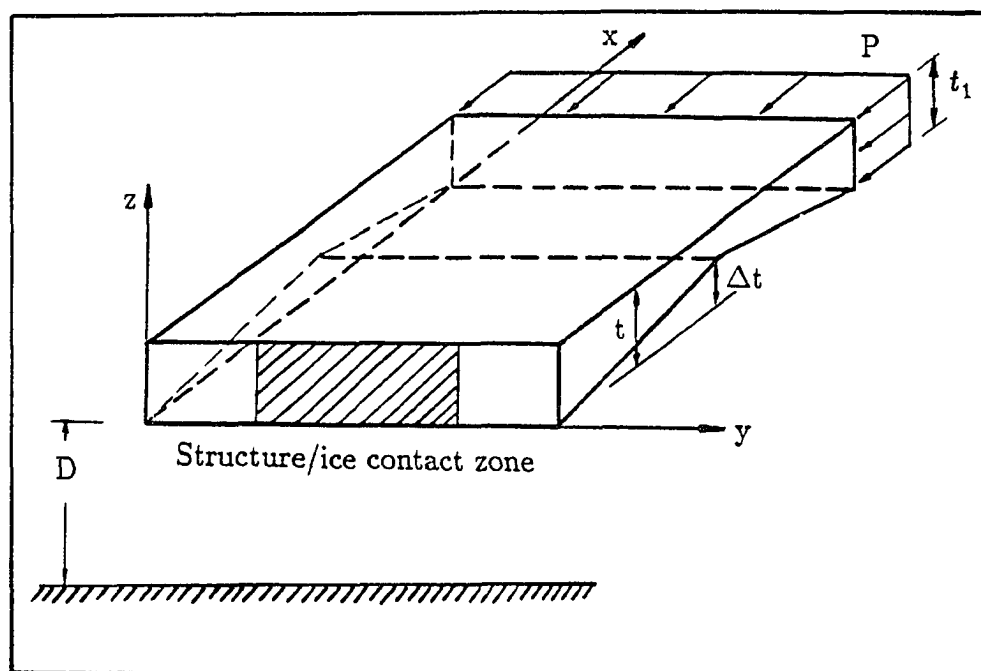


Fig. 2.3. Idealized uniformly-loaded multiyear sea ice floe model with a flat top and a one-dimensionally variable bottom in the central region of the floe thickness.

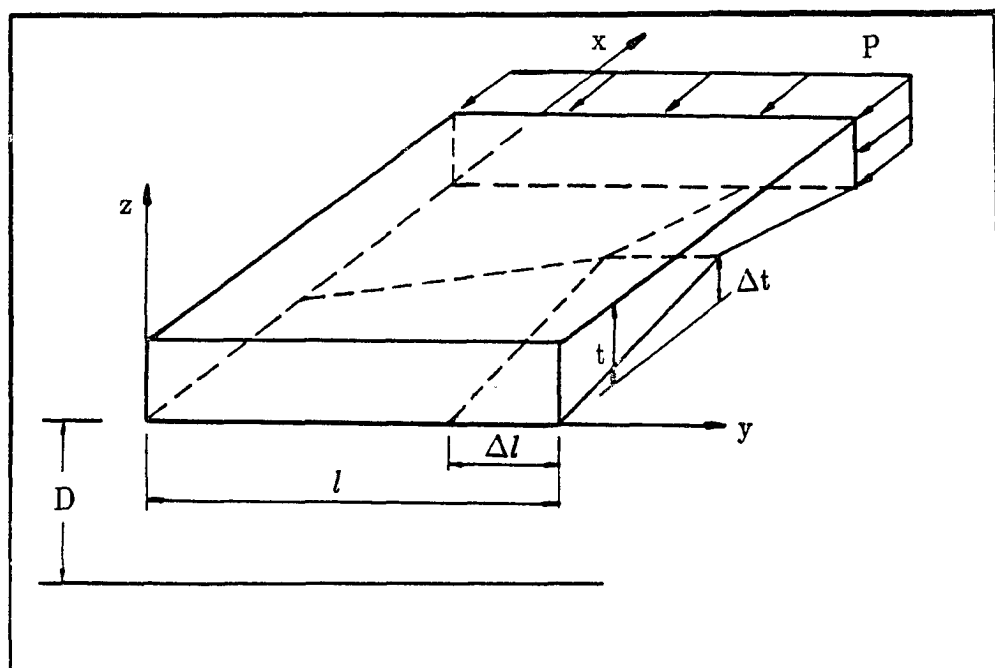


Fig. 2.4. Idealized uniformly-loaded multiyear sea ice floe model with a flat top and two-dimensionally variable bottom in the central region of the floe thickness.

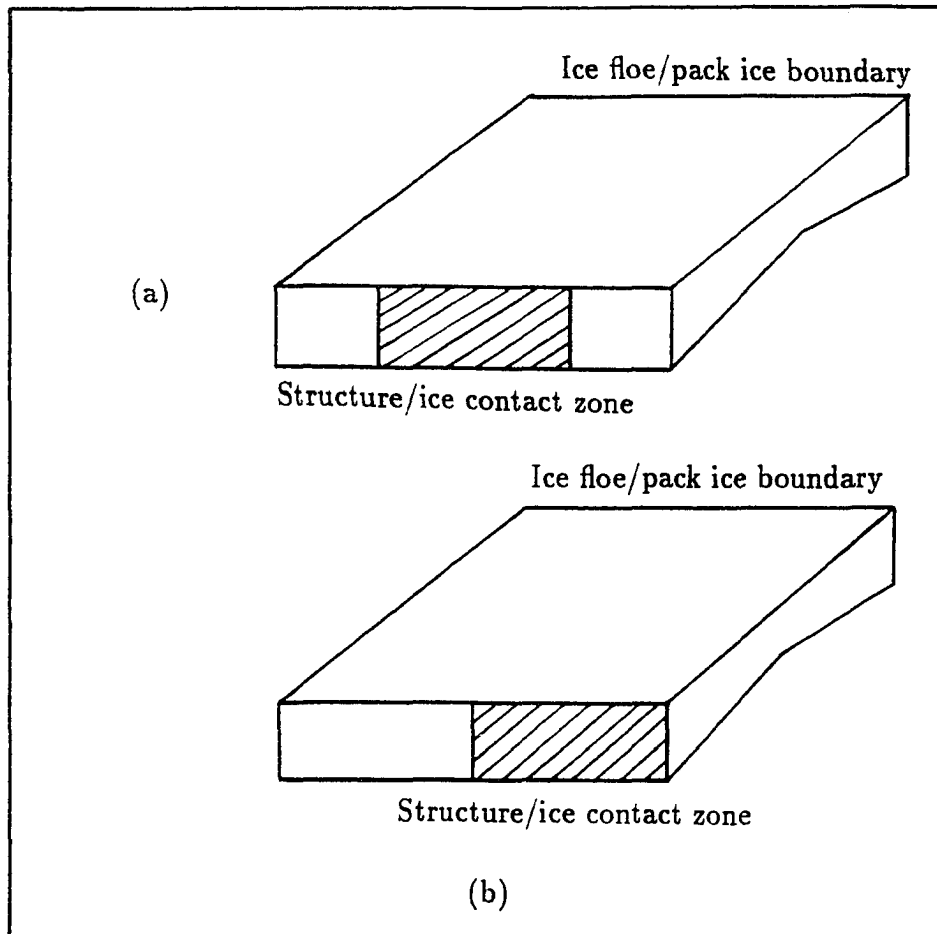


Fig. 2.5. Two locations of ice/structure contact zone are considered in the calculations: (a) the structure is located in the center region and (b) the structure is located in the eccentric region of the end of the floe.

Epomarine, IBMA (Isobutylmethacrylate) and PMMA (polymethylmethacrylate) show a smaller friction coefficient, ranging from 0.017 to 0.020, which is almost the same value as that of smooth stainless steel. Copolymer of CRREL (Polycarbonate + Polysiloxane), Vini-Bon-100 (Vinylchloride + Vinylacetate), SD_2-X (Polydimethylsiloxane), PTFE (Teflon) and Inerta-160 show coefficients from 0.027 to 0.033 as shown in Figure 2.6. In Figure 2.6 the shear stress is given as a function of the normal stress in the friction tests of sea ice, and the friction coefficient is obtained as the slope of the line (Tabata and Tusima, 1981). Some materials showed a high friction behaviour, such as Tar-epoxy (Kansai Paint Co.), Polymer Sealant, Kanpeglass and Vellox-140, with friction coefficients of 0.046, 0.14, 0.20 and 0.43, respectively (Tabata and Tusima, 1981). Therefore, the friction coefficient of $\mu=0$ used in our study is a reasonable approximation for the materials which showed small friction coefficients, such as Epomarine, IBMA and PMMA.

Buoyancy was represented by spring elements beneath the model ice floe, so that the restoring force was proportional to the vertical displacement. In the initial configuration, the model satisfied hydrostatic equilibrium.

The finite element mesh of the ice floe is shown in Figure 2.7. In the middle area of the ice floe was the finest grid area, a region in which more nodes were arranged to get more detailed and accurate results as shown in Figure 2.7 (b).

2.1.2 Parameters Used in the Calculations of the Ice Floe Model

Parameters of the ice floe model, and the variables used in the calculations, are shown in Table 2.1. The ice thickness amplitude variation in one-dimension, $\Delta t/t$, was divided into 5 groups. In each group the evaluation was done individually to subsequently compare and analyze the effects of a change in $\Delta t/t$. The ice thickness variation in two-dimensions, $\Delta l/l$, was divided into 3 groups, in which

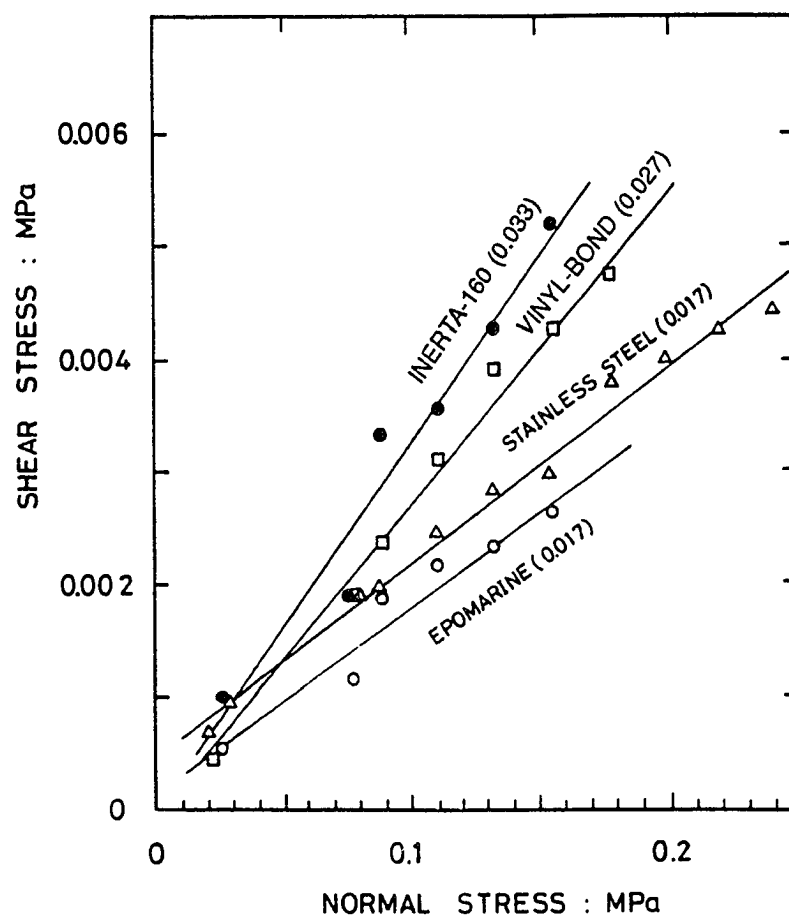


Fig. 2.6. The shear stress as a function of the normal stress in the friction tests of sea ice, from which the friction coefficient is obtained as the gradient of the line (Tabata and Tusima, 1981).

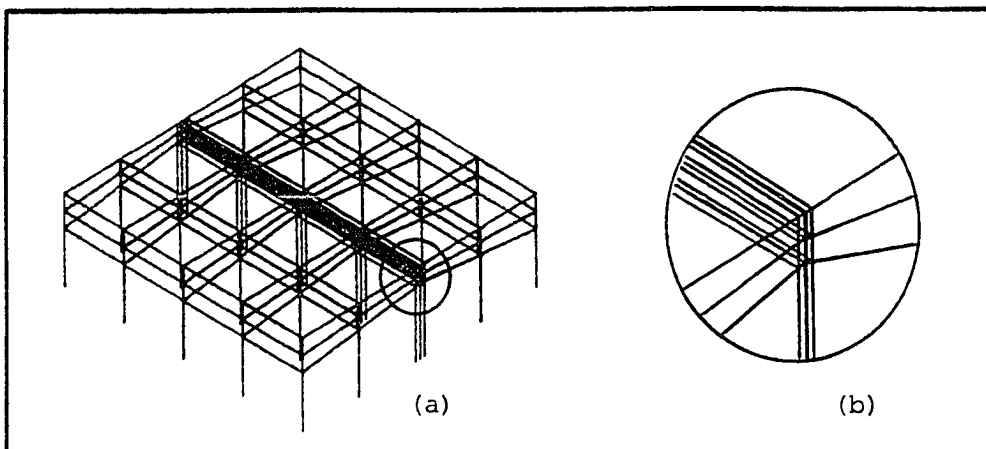


Fig. 2.7. (a) The finite element mesh of the ice floe in calculations; (b) arrangement of more meshes in the thinnest area of the floe and enlarged from the circle area in (a).

the $\Delta t/t$ is taken as 0.5. In each group the evaluation was also done to analyze the effects of two-dimensional ice thickness variation for a change of $\Delta l/l$.

The loading condition was represented by $t_1/t = 1$, in which t_1 was the vertical extent over which the averaged global pack ice compressive stress was applied, as shown in Figure 2.3, in the ice floe/pack ice contact zone. A second condition was for $t_1/t=0.5$, in which the vertical zone over which the averaged global pack ice compressive stress was applied was only half of the thickness of the ice floe. This examined a vertically-eccentric loading for the averaged global pack ice compressive stress in the ice floe/pack ice contact zone.

The elastic modulus of the ice was assumed in most calculations to be constant through the floe, with a value of 6 GPa. The constant modulus values of 4 GPa and 8 GPa were also applied to give a examination of influence of different magnitude of the elastic modulus. However, the effect of an elastic modulus variable with depth is of practical interest, because the modulus decreases with increasing temperature, as discussed by Cox and Richter-Menge (1985). Since temperature increases with depth, modulus decreases with depth. Therefore, the elastic modulus value was used at the top surface of the ice floe, 6 GPa, and elastic modulus at the bottom of the ice floe was taken as 3 GPa in specific calculations to examine the effects of different elastic module. A crystallographic study for the anisotropy of natural sea ice (Wang, 1979) showed that sea ice at different locations could be quite different in structure. However, very few data are available for multiyear ice. Following conventional usage (Mellor, 1983), a value of 0.3 was adopted for Poisson's ratio. The applied average pack ice compressive stress (P) was assumed to vary initially in 0.5 MPa increments for each value of $\Delta t/t$, to examine and compare results with previous work. It subsequently was found that more exact applied global stresses were needed to find the first failure condition in the ice floe; global stresses are to

TABLE 2.1. Parameters used in the calculations of the ice floe model.

t : Maximum ice thickness; $\Delta t/t$: ice thickness amplitude variation in one-dimension; $\Delta l/l$: ice thickness amplitude variation in two-dimensions in which $\Delta t/t = 0.5$; t_1/t : loading condition; E : constant elastic modulus; E_t : variable elastic modulus at the top surface of the floe; E_b : variable elastic modulus at the bottom of the floe; ν : Poisson's ratio; P : applied global ice compressive stress; D : water depth.

t (m)	6
$\Delta t/t$	0.0,0.4,0.5,0.65
$\Delta l/l$	0.25,0.5,0.75
t_1/t	0.5,1.0
E (GPa)	4,6,8
E_t (GPa)	6
E_b (GPa)	3
ν	0.3
P (MPa)	variable values
D (m)	16

be discussed later. Finally, as shown in Table 2.1, the water depth was taken as 16 m.

In the calculations including a compliant structure and foundation, most of the parameters of the ice floe model were the same as those used for a rigid structure, as shown in Table 2.1. The foundation was considered as a viscoelastic medium, which will be discussed more in Chapter 4.

2.2 Ice Island/Structure Interaction Model

Ice islands surrounded by pack ice are the largest ice features in the Arctic Ocean. They are large masses of flat, low-salinity ice with a correspondingly-high compressive strength as compared to sea ice. The ice island/structure interaction

model is shown in Figure 2.8, which is another main model in this study, used to analyze the indentation of ice island against a rigid structure. A three-dimensional finite element method, and another theoretical method, were used.

2.2.1 Ice Island Model

The ice island was taken to be a 3000 m by 2500 m rectangular shape, with a uniform thickness of 20 m. A rigid structure with a diameter of 150 m was assumed in these calculations. The finite element mesh of the ice island model is shown in Figure 2.9. More nodes were arranged in the area of the ice island/structure contact zone to obtain more accurate calculation results from the indentation of the ice island against the structure. Ice powder and fragments produced in the area where local ice failure occurred was treated during the calculations. The ice powder was generated initially at the contact area when the ice island strikes the structure. This zone progressively grows in area and in extent. Stresses will be transmitted through the ice powder to the ice island/structure boundary according to relationships which will be discussed in more detail in Chapter 5.

2.2.2 Parameters Used in the Calculations of the Ice Island Model

Parameters of the ice island model, and variables used in the calculations, are shown in Table 2.2. The ice island thickness was taken as a constant of 20 m. Elastic modulus and Poisson's ratio were 7 GPa and 0.3. The applied global pack ice compressive stress was assumed to vary initially in 0.5 MPa increments for each condition of ice island indentation into the structure. Water depth was taken as 35 m. The parameters used in the separate theoretical analysis for the ice island/structure interaction were the same as those used in the finite element method approach. More discussion on both the theoretical and the finite element method calculations are presented in Chapter 5.

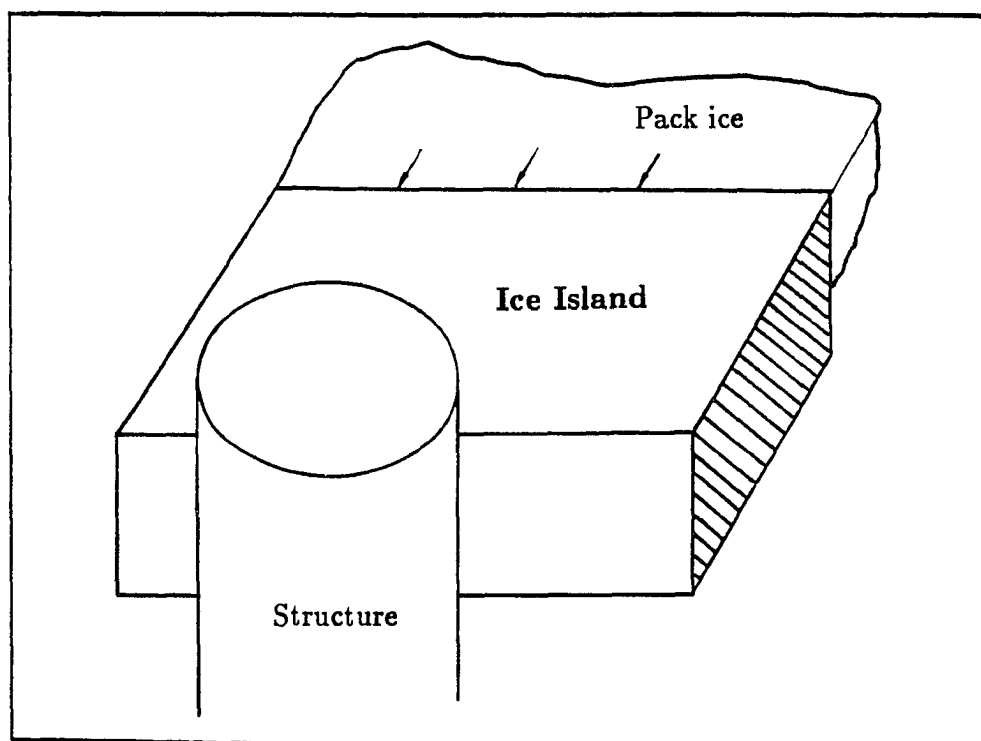


Fig. 2.8. Schematic diagram of a ice island surrounded by pack ice and impacting a vertical structure.

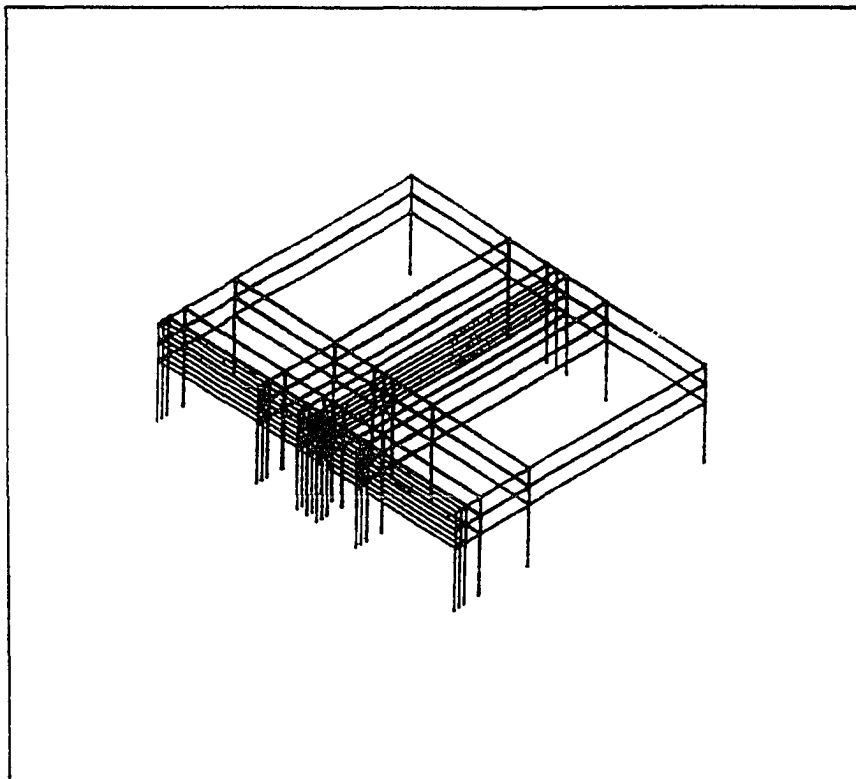


Fig. 2.9. The finite element mesh of the ice island in calculations, more meshes are arranged in the ice island/structure contact zone and in the center region of the ice island to analyze the indentation.

TABLE 2.2. Parameters used in the calculations of the ice island model.

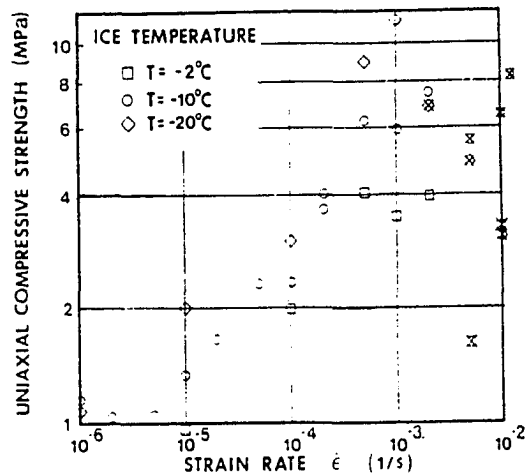
t_s : ice island thickness; E_s : constant elastic modulus; ν : Poisson's ratio; P: applied global ice compressive stress; D: water depth.

t_s (m)	20
E (GPa)	7
ν	0.3
P (MPa)	variable values
D (m)	35

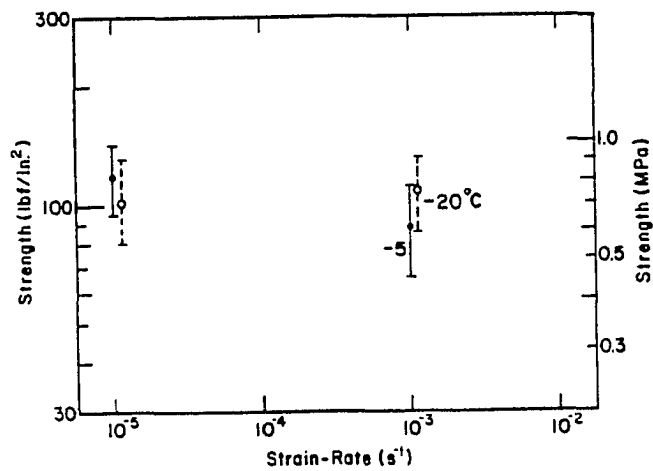
2.3 Mechanical Properties of Multiyear Ice and Failure Criterion

Ice is not purely elastic, viscous or plastic, and so does not readily lend itself to classical engineering analysis. When a stress is applied to a sample of ice, it displays a combination of responses: it shows an instantaneous elastic response, then begins to creep. In addition, ice is an extremely brittle material, but if the applied stress is high enough or is applied for long enough, then ice deforms by ductile creep. The mechanical properties of the ice are strongly dependent upon loading conditions, as well as upon types of ice, the ice temperature, salinity, and other variables.

The measurements and results for the properties of ridged multiyear ice for the compressive strength and tensile strength of the ice were done by Cox and Richter-Menge (1985), and Riska and Frederking (1987), as are shown in Figure 2.10. Their data, for the range of variables indicated, show that the uniaxial compressive strength and tensile strength are relatively insensitive to the loading rate. Accordingly, 1 MPa for the tensile strength and 8 MPa for the compressive strength were adopted for use in this study, in which the ice is treated either as an elastic or viscoelastic continuum. A more complete failure criterion given by Riska



(a)



(b)

Fig. 2.10. Mechanical properties of multiyear ice from Cox and Richter-Menge (1985), and Riska and Frederking (1987). (a) uniaxial compressive strength (Riska and Frederking, 1987); (b) uniaxial tensile strength (Cox and Richter-Menge, 1985).

and Frederking (1987), based upon multi-axial test results, was also used in this study. The failure function $f(\sigma)$ in their criterion is given by

$$f(\sigma) = F_{11}I_1 + \frac{1}{3}(G_{1111} + 2G_{1122})I_1^2 + 4G_{1212}J_2 \quad (2-1)$$

where F_{11} , G_{1111} , G_{1122} and G_{1212} are coefficients determined by test results using the Tsai-Wu criterion (Riska and Frederking, 1987). They showed that F_{11} is in the range of 0.736 to 0.988 MPa^{-1} , G_{1111} is 0.137 to 0.417 MPa^{-2} , G_{1122} is -0.024 to -0.188 MPa^{-2} , and $G_{1212}=0.5(G_{1111}-G_{1122})$. The first invariant of stress, I_1 , is given by

$$I_1 = \sigma_{11} + \sigma_{22} + \sigma_{33} \quad (2-2)$$

and J_2 is the second invariant of the deviatoric stress, given by

$$J_2 = [(\sigma_{11} - \sigma_{22})^2 + (\sigma_{22} - \sigma_{33})^2 + (\sigma_{33} - \sigma_{11})^2] \frac{1}{6} + \sigma_{12}^2 + \sigma_{23}^2 + \sigma_{31}^2 \quad (2-3)$$

where σ_{ij} ($i, j=1, 2, 3$) are the stress components. The surface $f(\sigma)=1$ is called the failure surface or envelope, and Figure 2.11 shows the failure surface with the $\sigma_1 - \sigma_2$ plane ($\sigma_3=0$) (Riska and Frederking, 1987).

For the purposes of analysis, the properties of the ice using a 4-parameter fluid or Burger's model is shown in Figure 2.12 to describe the range of behavior. In the model, the individual spring and dashpot elements may be either linear or nonlinear, and the strain of the lead spring represents the instantaneous elastic response of the material to an applied load. The spring and dashpot in parallel provides a time-dependent elastic strain which is totally recovered upon removal of the load. Time-dependent elastic strain is represented on strain-time curves for

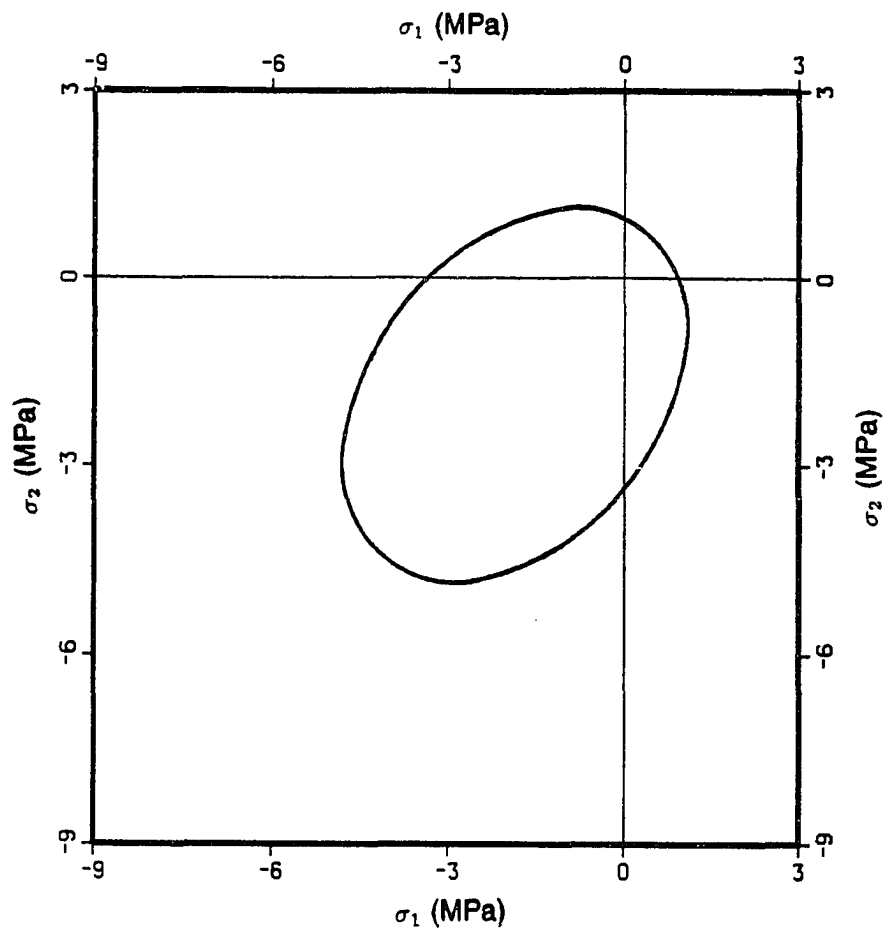


Fig. 2.11. The failure surface on a plane of principal stress (Riska and Frederking, 1987).

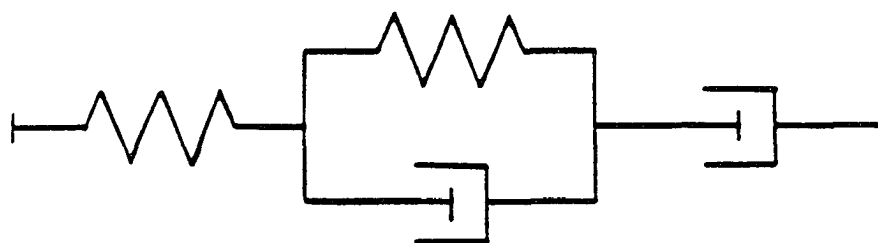
constant stress as the primary creep stage. The remaining dashpot gives the time-dependent, permanent strain (secondary or steady state creep on the strain-time curve for constant stress). The equations for these and other models and loading conditions were given in Mellor (1983). In calculations, the material response can be represented by the Maxwell model (Figure 2.12), which consists of a spring and dashpot in series. This assumption is used in the viscoelastic case, in which the response of the dashpot to a constant stress is described by the nonlinear Glen's law for the flow of the ice,

$$\frac{d\varepsilon}{dt} = A\sigma^B \quad (2-4)$$

where ε is strain, t is time, σ is stress, and A and B are constants, which are described in detail in section 3.7 of Chapter 3.

2.4 Computation Method

The calculations were conducted using the program "Automatic Dynamic Incremental Nonlinear Analysis" (ADINA) (ADINA R & D Inc., 71 Elton Ave., Watertown, MA 02171, USA). It is a general finite element program and composed of three programs: (1) ADINAIN for creating input data, (2) ADINA for calculation, and (3) ADINAPLOT for displaying both the input and output data. A flow chart of the steps required to run the calculations on ADINA are illustrated in Figure 2.13. A complete program by ADINA for one of the examples of the ice floe model, some programs in VAX to analyze and plot the results from ADINA, and the program by FORTRAN in VAX used in the theoretical analysis of ice island loads acting on a rigid cylindrical structure, all can be found in the Appendix.



BURGER'S MODEL

(a)



MAXWELL MODEL

(b)

Fig. 2.12. (a) 4-parameter fluid or Burger's model for a viscoelastic material. (b) Maxwell model; for this study the dashpot is assumed to follow Glen's Law, given by the equation (2-4).

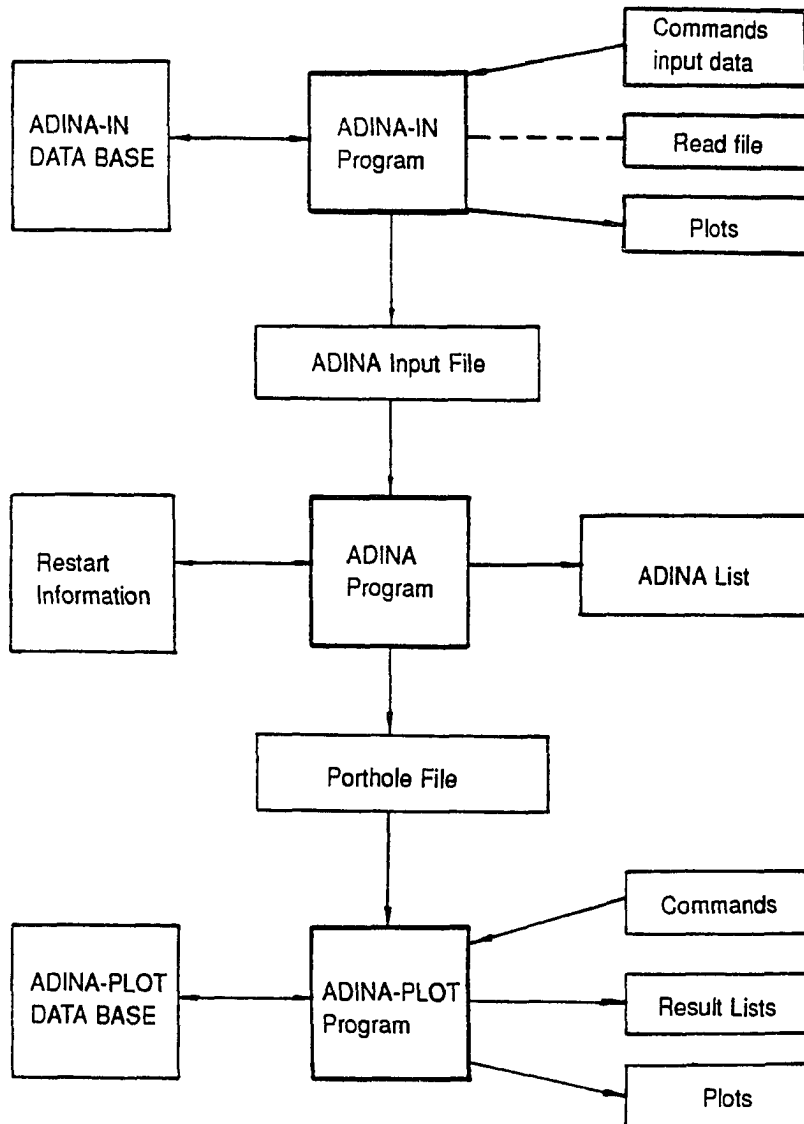


Fig. 2.13. Execution sequence of ADINA-IN, ADINA and ADINA-PLOT.

All of the results and analyses by three-dimensional finite element methods, for all models, are divided into three parts to be described in this thesis. They are **Chapter 3-Stress Analysis of an Ice Floe against a Rigid Structure**, in which two boundary conditions (fixed and sliding) were considered using all of the parameters shown in Table 2.1; **Chapter 4-Deformation and Stress Analysis of the Structure and the Foundation**, for the results of the ice floe model with compliant structure and viscoelastic foundation; **Chapter 5-Analysis of the Ice Island Loads Acting upon a Cylindrical Structure**, in which both theoretical and finite element methods were used; the ice powder and fragments were treated and analyzed in the calculations with the finite element method. The conclusions are presented in **Chapter 6**.

CHAPTER 3

Stress Analysis of an Ice Floe against a Rigid Structure

The results in this Chapter were calculated using all of the parameters shown in Table 2.1 for the ice floe model with a rigid structure, in which two boundary conditions were assumed: a fixed boundary condition, in which a multiyear ice floe is adfreeze-bonded to the structure; and a sliding boundary condition, in which the multiyear ice floe can slide at the ice/structure contact zone.

3.1 Stress Analysis for One-Dimensional Ice Thickness Variation, Ice Structure Contact Zone Located in the Central Region

3.1.1 Stress Analysis, Comparison with Two-Dimensional Finite-Element Method, and Experimental Results

Some results of calculations by the three-dimensional finite-element method for the stress distribution along the x-direction on the top, middle and bottom surface, in the middle of the ice floe in the y-direction, are presented in Figure 3.1. The results for a one-dimensional variable thickness of $\Delta t/t = 0.5$ and the uniform thickness of $\Delta t/t = 0.0$, are shown. The quantity S_r is the dimensionless stress in the plane along the centerline of the floe, shaded in Figure 3.1 (c), which has been normalized by dividing by the applied global compressive ice stress. Results are presented for the same applied global ice stress of $P=0.5$ MPa, so that the comparison can be made to analyze the effects of variable thickness. It is obvious that the stress in the thinnest area of the top surface of the variable-thickness ice floe (along line a-a') is a tensile stress as shown in Figure 3.1 (a). (Negative values of S_r mean compressive stress.) The maximum computed tensile value of S_r is 2.6 along line a-a', which means the tensile strength of ice (1 MPa approx.) would be

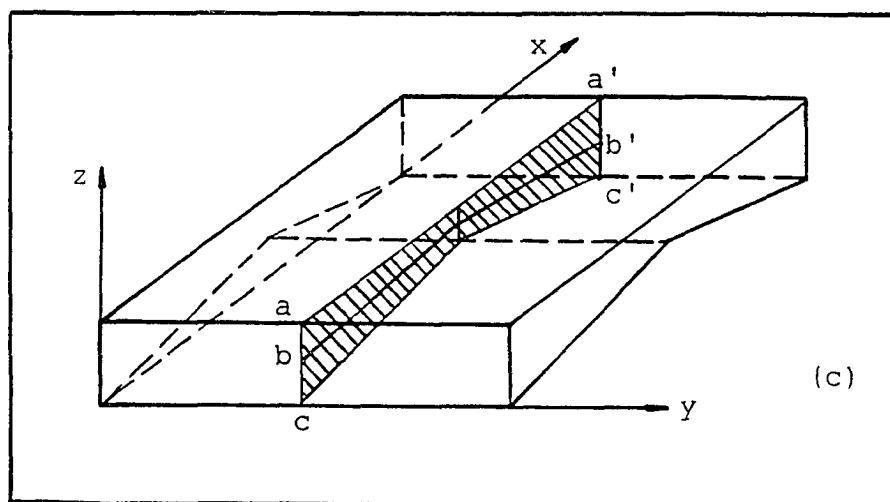
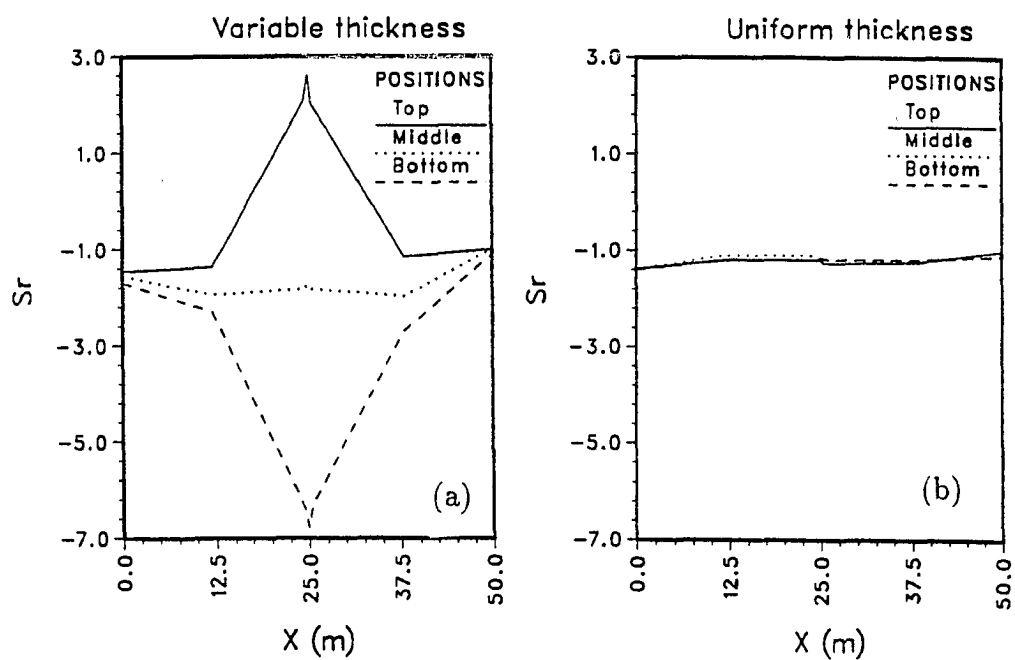


Fig. 3.1. Stress ratio (S_r) between the stress in the ice floe and the applied average pack ice compressive stress (P), is a function of x as shown in (c), in which the positions of top, middle and bottom are also defined.

exceeded (Hallam et al., 1987). Tensile failure at this location in the floe actually takes place at an applied global ice compressive stress value of 0.36 MPa, as will be discussed below. Along the line b-b', S_r is negative, indicating compression. Along the line c-c', S_r is strongly negative, reaching -7.0. The compressive strength of multiyear ice at -5°C and loading rates of 10^{-5} s^{-1} (Cox et al., 1984) would be exceeded for most multiyear ice types. Another view of the value of S_r as a function of x and y direction on the top surface of the ice floe is shown in Figure 3.2, in which the positive value (tensile stress) occurred only in the thinnest area of the ice floe. It is clear that bending is localized in the thinnest area of the ice floe, consistent with Hallam et al. (1987). The results for one-dimensional variable thickness of $\Delta t/t=0.4$ and 0.65 are similar to $\Delta t/t = 0.5$ (They will be summarized in Figure 3.3 for the stress factor S_r for the different ratio of $\Delta t/t$). However, for a uniform-thickness ice floe, the stress is compressive along lines a-a', b-b', and c-c', with $S_r \cong -1.4$, as shown in Figure 3.1 (b); bending is insignificant.

The stress factor S_r along a-a' in the thinnest area of the ice floe is plotted as a function of ice floe thickness variation in Figure 3.3. It increases as the center thickness of the ice floe decreases. Our three-dimensional results agree well with the two-dimensional calculations of Takeuchi and Shapiro (1989) and the experimental data and theoretical solution of Hallam et al. (1987).

3.1.2 Localized Maximum Ice Pressure on the Structure, and Load Reduction Factor

The calculated values of applied global compressive stress needed to cause the first failure in the ice floe for different ratios of $\Delta t/t$ are shown in Table 3.1. (Compressive strength of ice was assumed and taken as 8 MPa from Hallam et al., 1987). For $\Delta t/t = 0.0$, a uniform-thickness ice floe, the ice first failure occurred at points A and B of the structure/ice contact zone as shown in Figure 3.4, as a compressive stress failure. An average pack ice compressive stress of 5.0 MPa

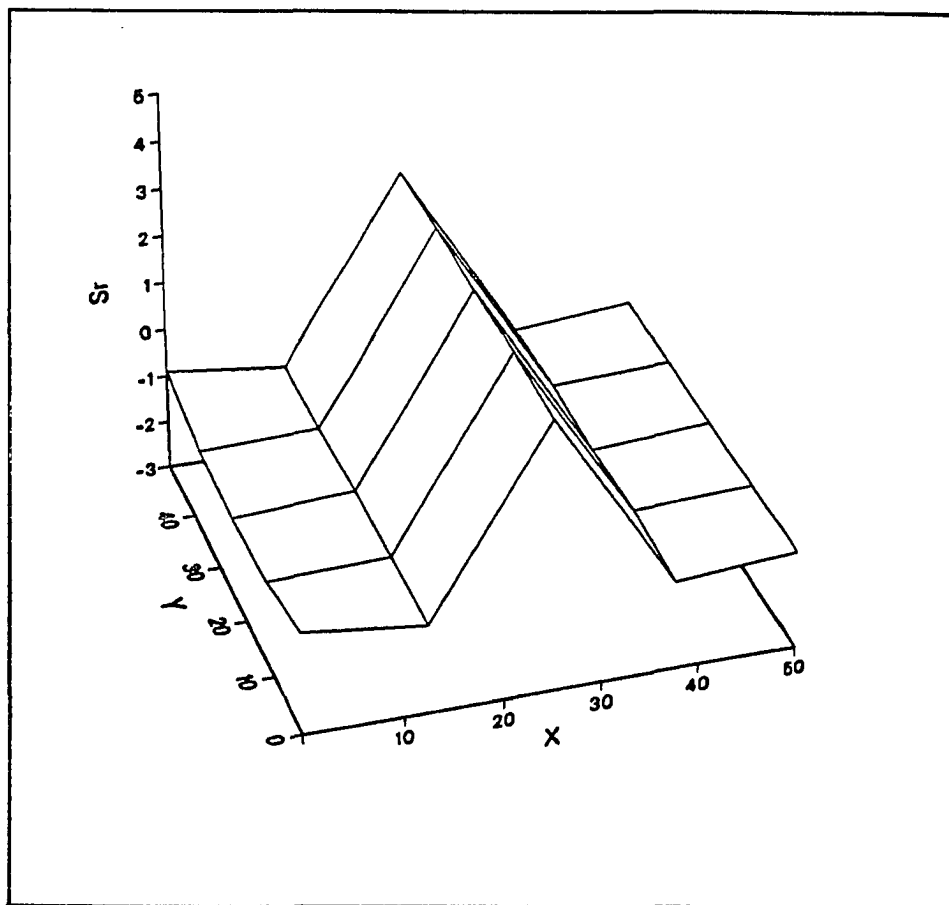


Fig. 3.2. S_r distributions on the top surface of the floe; positive value means a tensile stress, which can be seen only in the thinnest area of the floe.

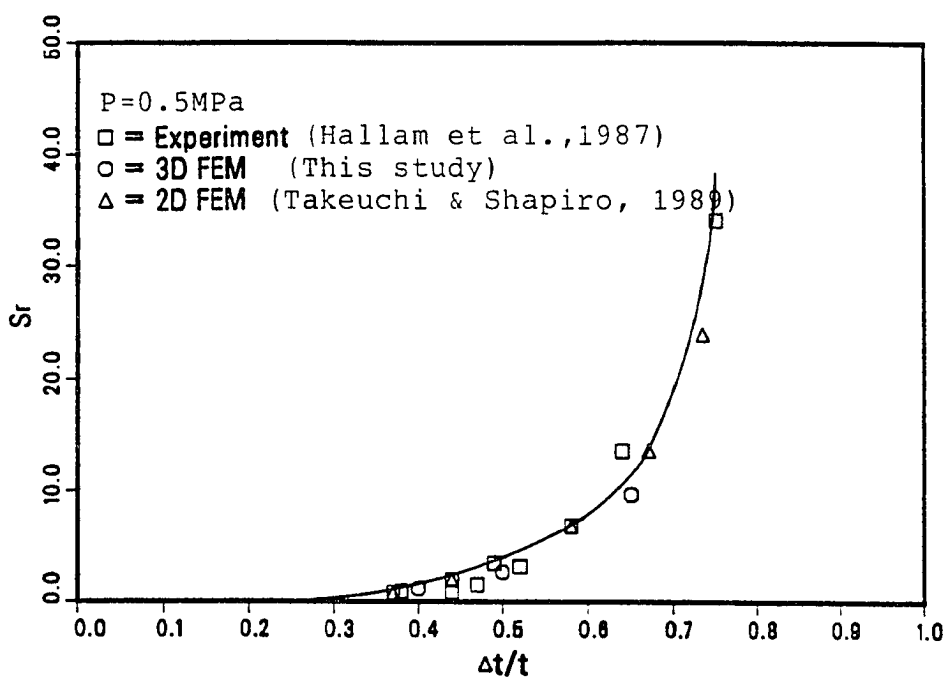


Fig. 3.3. Comparison of the results of the three-dimensional finite-element method to the experimental and theoretical results (Hallam et al., 1987), and the two-dimensional finite-element method results (Takeuchi and Shapiro, 1989). The stress increase factor S_r on the top surface at the thinnest area of the ice floe is presented as a function of ice floe thickness variation.

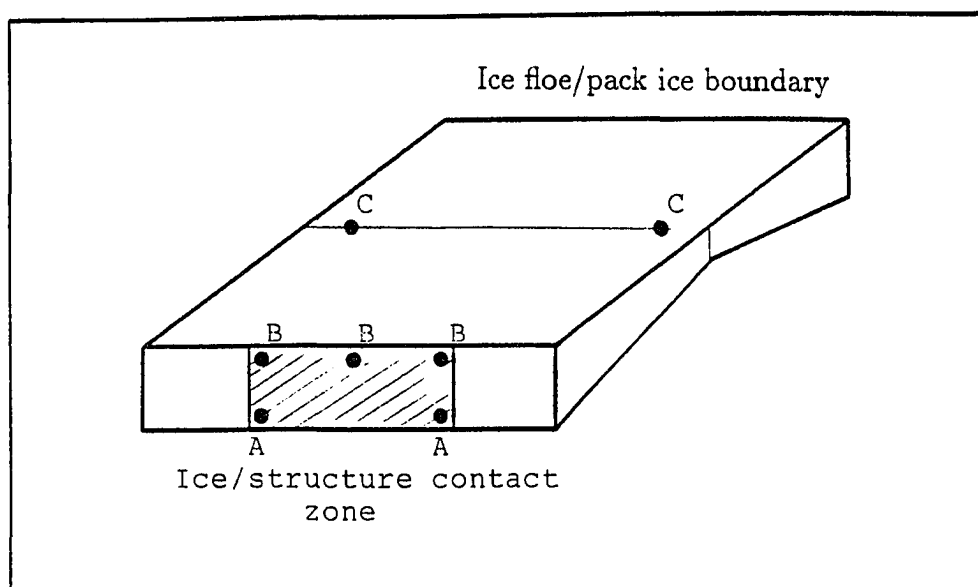


Fig. 3.4. Schematic diagram of localized maximum ice pressure computed at the points A and B regions of the ice/structure contact zone, and maximum ice tensile stress computed at points C.

caused this failure. The total force acting on the structure was 1500 MN, when this failure occurred.

For $\Delta t/t = 0.4$, a variable-thickness ice floe, tensile cracks first formed at the upper surface, at the points C (Figure 3.4) of the thinnest area of the floe, and the average pack ice compressive stress of 0.91 MPa caused these failures. The maximum localized ice pressure on the structure when the ice first failed was computed at points A and B of the structure/ice contact zone. These values were defined as P_b and P_t and are shown in Table 3.1. The pressure computed at points A was 1.61 times larger than the average pack ice compressive stress (P). The total force acting on the structure was 273 MN, as compared with 1500 MN which would be present for $\Delta t/t=0.0$; thus a structure load reduction factor of 5.5 was obtained.

For $\Delta t/t = 0.5$ and 0.65 , average pack ice compressive stresses of 0.36 MPa and 0.12 MPa were needed to cause the first tensile failure at the top surface in the thinnest area (points C) of the ice floe. The localized maximum pressures on the structure are shown in Table 3.1, in the same positions A and B as for $\Delta t/t = 0.4$. The total force acting on the structure was 108 MN for $\Delta t/t = 0.5$ and 36 MN for $\Delta t/t = 0.65$. Thus, the structure load reduction factors (R) are 13.9 for $\Delta t/t = 0.5$ and 41.7 for $\Delta t/t=0.65$. The structure load reduction factor as a function of $\Delta t/t$ is plotted in Figure 3.5, from which it is interesting to note that the larger the ice floe thickness variation, the smaller the total force acting on the structure.

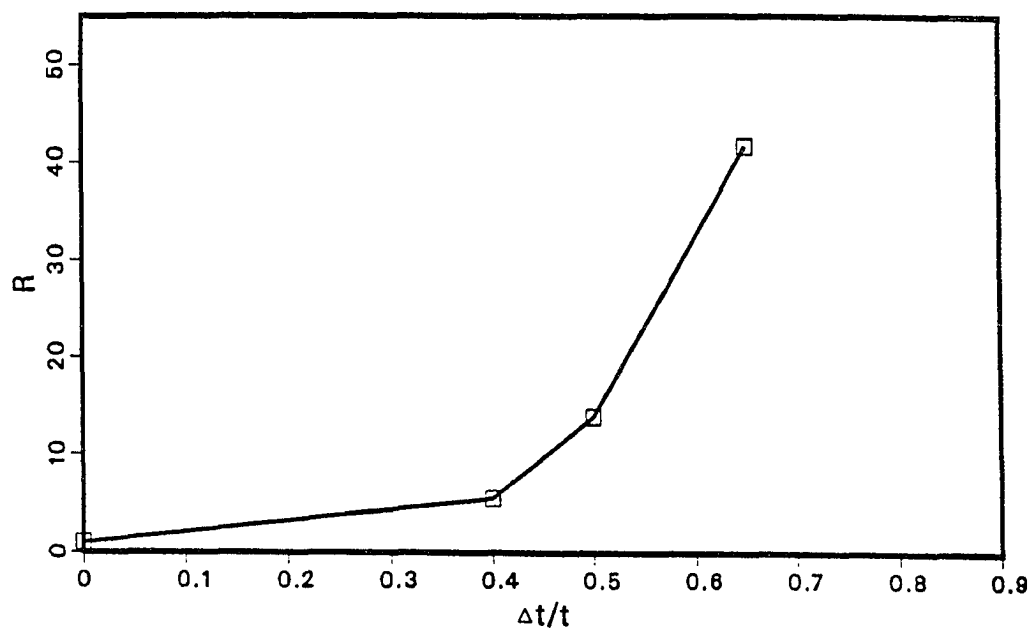


Fig. 3.5. Structure load reduction factor (R) as a function of the ice floe thickness irregularity.

TABLE 3.1. Applied global pack ice compressive stress P , localized maximum ice pressure, load reduction factor R , and total forces on structure versus $\Delta t/t$, corresponding to the conditions of first ice failure.

P_{lb} and P_{lt} are the localized maximum ice pressure at points A and B of the structure/ice contact zone as shown in Figure 3.4.

$\Delta t/t$	0.0	0.4	0.5	0.65
P (MPa)	5.0	0.91	0.36	0.12
P_{lb} (MPa)	8.04	1.72	0.71	0.25
P_{lt} (MPa)	8.04	1.59	0.64	0.22
Total forces (MN)	1500	273	108	36
Reduction factor R	1.0	5.5	13.9	41.7

3.1.3 Deformation of the Ice Floe

The deformations of the ice floe under an applied pack ice compressive stress, when the ice floe first failed, were also given by the results of the three-dimensional finite-element method. Both variable-thickness and uniform-thickness ice floes were considered. The results in terms of deformed meshes are shown in Figure 3.6, which provides a view of deformation of the ice floe and the contrasting differences between a variable-thickness and uniform-thickness ice floe. The largest displacements occurred at the boundaries of the ice floe with the pack ice zone. For a uniform thickness ice floe, displacements were $\Delta x = -0.047$ m, $\Delta y = 0.00$ m and $\Delta z = -0.0006$ m as shown in Table 3.2. The largest displacement occurred in the x-direction.

However, for a variable-thickness ice floe, large displacements occurred in both x and z directions. Values of $\Delta x = -0.0084$ m, $\Delta y = 0.00$ m and $\Delta z = -0.023$ m, were calculated, for $\Delta t/t = 0.5$. The displacement is even larger in the z-direction than in the x-direction, which means that the bending occurred on the top surface of the ice floe, allowing a displacement downward in the z-direction, corresponding

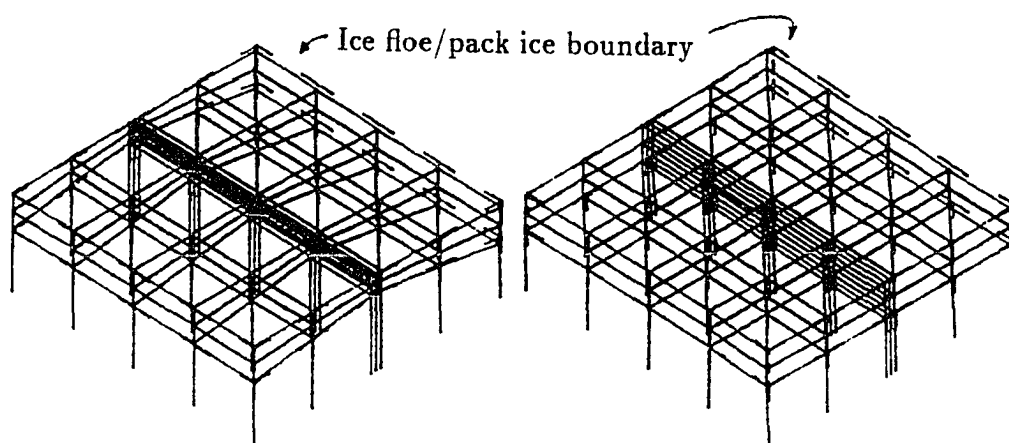


Fig. 3.6. Deformed meshes of variable thickness and uniform thickness of the ice floe, and the largest displacements computed at the region of ice floe/pack ice zone.

TABLE 3.2. Displacements in x, y and z directions, and angle of deflection (θ) (Fig. 3.7) of the floe at point a' (Fig. 3.3) of the floe/pack ice contact zone, corresponding to the conditions of first ice failure.

$\Delta t/t$	0.0	0.4	0.5	0.65
Δx (m)	-0.047	-0.016	-0.0084	-0.0052
Δy (m)	0.00	0.00	0.00	0.00
Δz (m)	-0.0006	-0.034	-0.023	-0.018
θ (degrees)	-0.0007	-0.039	-0.026	-0.021

to the condition of first tensile failure. Similar results are shown in Table 3.2 for $\Delta t/t=0.4$ and 0.65 . The downward deflection of the ice floe at the ice floe/pack ice boundary, as a function of ice floe thickness variation, is presented in Figure 3.7 and Table 3.2. The negative value means a downward direction of displacement, corresponding to the conditions of first tensile fracture for the variable-thickness ice floe.

3.2 Examination of the Ice/structure Contact Zone Located in the Eccentric Region

As discussed above, the stress analysis was given by an ice/structure contact zone located in the central region at the end of the ice floe (Figure 2.5 (a)). It is well worth considering the effects of an ice/structure contact zone, which is located in the eccentric region of the end of the ice floe, and the stress that can then be transmitted to the structure through the floe. Results were obtained by using the same parameters used in the section 3.1. However, the ice/structure contact zone was located in the eccentric region as shown in Figure 2.5 (b). Results are shown in Table 3.3.

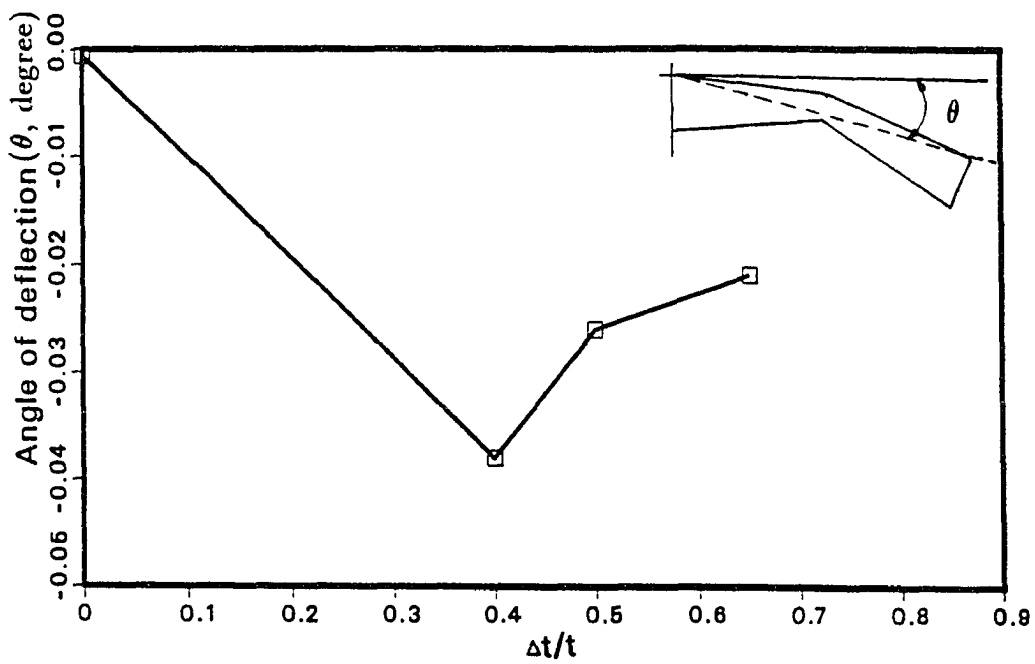


Fig. 3.7. The angle of deflection of the ice floe is a function of ice floe thickness reduction ratio, in which the negative value means downward direction of the deflection, corresponding to the conditions of first failure of the ice floe.

TABLE 3.3. Results given for the ice/structure contact zone located in the eccentric region of the one end of the ice floe.

S_{rm} : maximum value of stress ratio on the top surface of the floe for the same applied global pack ice compressive stress of $P=0.5$ MPa; P_f : applied global pack ice compressive stress corresponding to the conditions of the ice first failure; F : total force acting on the structure. The values in the parentheses are from the prior results for case of the ice/structure contact zone located in the central region of the end of the floe.

$\Delta t/t$	0.0	(0.0)	0.4	(0.4)	0.5	(0.5)	0.65	(0.65)
S_{rm}	-1.5	(-1.4)	1.46	(1.2)	2.81	(2.6)	10.11	(9.3)
P_f (MPa)	4.4	(5.0)	0.79	(0.91)	0.33	(0.36)	0.09	(0.12)
F (MN)	1320	(1500)	237	(273)	99	(108)	27	(36)

It can be seen that the S_{rm} value of -1.5 was smaller than the value of -1.4 in the parentheses (the result from the prior case when the ice/structure contact zone was located in the central region of the floe). This was for $\Delta t/t = 0.0$ and the applied global ice stress of $P=0.5$ MPa, and means that larger compressive stress (0.75 MPa) occurred due to the eccentric boundary condition at points A_1 shown in Figure 3.8. The very small compressive stress (0.09 MPa) presented at points B_1 (Figure 3.8), even became a tensile stress when P increased to 4.4 MPa, corresponding to the ice compressive first failure at points A_1 due to the fixed boundary condition. The total force of 1320 MN acting on the structure was also smaller as compared with the value of 1500 MN in the parentheses.

For $\Delta t/t=0.4$, a variable-thickness floe, the S_{rm} value of 1.46 was larger than the value of 1.2 in the parentheses, which indicated a larger tensile stress in the thinnest area of the floe than that resulting from a ice/structure contact zone located in the central region (for the same applied global pack ice compressive stress of $P=0.5$ MPa). The applied global pack ice compressive stress of $P=0.79$

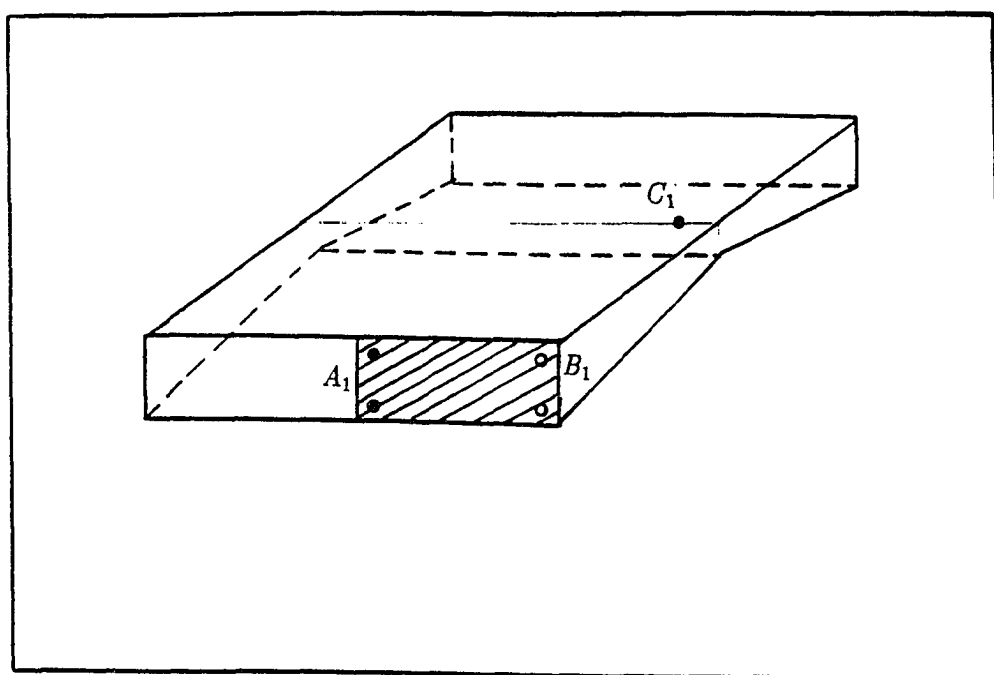


Fig. 3.8. Schematic diagram of localized maximum ice pressure computed at the points A_1 regions of the ice/structure contact zone, and maximum ice tensile stress computed at points C_1 . Points B_1 show a smaller pressure.

MPa was needed to cause the ice first tensile failure only at point C_1 (Figure 3.8). This was also smaller than the value of 0.91 MPa in the parentheses as shown in Table 3.3. The total force acting in the structure was 237 MN, which was smaller than 273 MN, the value in parentheses. The localized maximum ice pressure on the structure occurred at points A_1 (Figure 3.8), and was 2.01 MPa.

Similar results were obtained for $\Delta t/t=0.5$ and $\Delta t/t=0.65$ as compared with $\Delta t/t=0.4$, for the variable-thickness ice floe. At a lower applied stress, results showed a tensile failure in the thinnest area of the floe, as compared with a central region boundary condition for the ice/structure contact zone. Thus, a smaller global force was acting on the structure as shown in Table 3.3, and the ratios of global forces on the structure between eccentric and centric cases were 0.88, 0.87, 0.92 and 0.75, for $\Delta t/t=0.0$, $\Delta t/t=0.4$, $\Delta t/t=0.5$ and $\Delta t/t=0.65$, respectively.

3.3 Examination of the Sliding Boundary Condition

The examination of a sliding boundary condition, for which the ice floe could move up and down in the ice/structure contact zone, was obtained using the same parameters used in 3.1 except for the imposition of the sliding boundary condition. It is reasonable to consider a situation for which the ice floe was not frozen to the structure, as another possible condition for the ice/structure interaction analysis. The friction coefficient in the ice/structure interface was taken as $\mu=0.0$, a reasonable approximation as discussed in Chapter 2.

Results showed a slight change in the stress analysis as shown in Table 3.4. For a uniform-thickness ice floe of $\Delta t/t=0.0$, the same value of $S_{rm}=-1.4$ was seen, but a larger P_f of 5.6 MPa was needed to cause the ice first compressive failure. The smaller value of 5.0 MPa in parentheses was for the case of the fixed boundary condition, which was located at points A_2 shown in Figure 3.9. There was a change

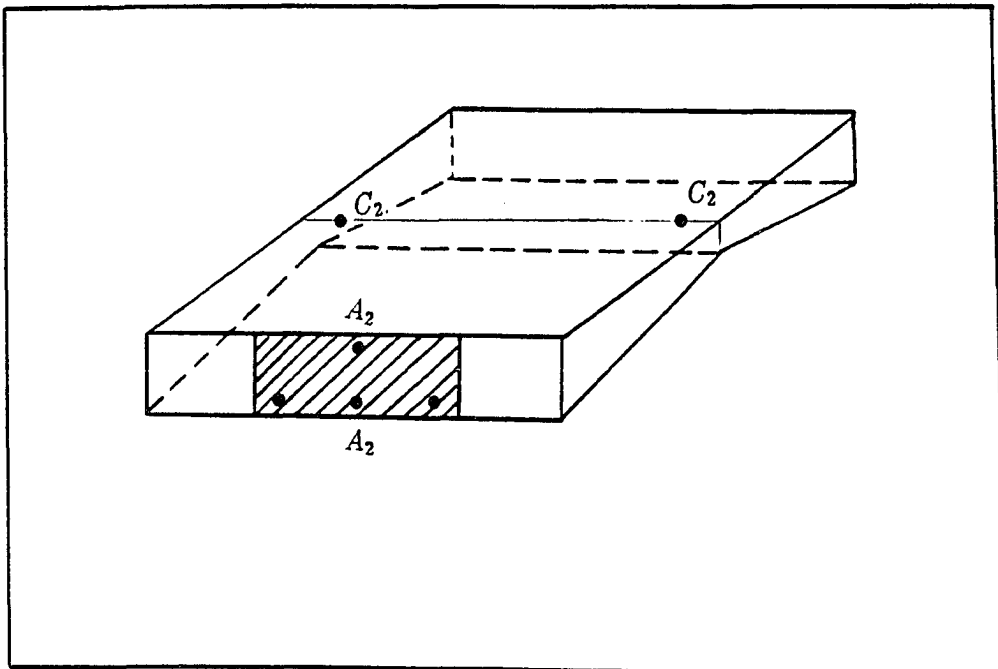


Fig. 3.9. Schematic diagram of localized maximum ice pressure computed at the points A_2 regions of the ice/structure contact zone, and maximum ice tensile stress computed at points C_2 .

TABLE 3.4. Results given by the sliding boundary condition in the ice/structure interface.

S_{rm} : maximum value of stress ratio on the top surface of the floe for the same applied global pack ice compressive stress of $P=0.5$ MPa; P_f : applied global pack ice compressive stress corresponding to the conditions of the ice first failure; F : total force acting on the structure. The values in the brackets are from the results for a fixed boundary condition.

$\Delta t/t$	0.0	(0.0)	0.4	(0.4)	0.5	(0.5)	0.65	(0.65)
S_{rm}	-1.4	(-1.4)	1.2	(1.2)	2.7	(2.6)	9.3	(9.3)
P_f (MPa)	5.6	(5.0)	1.12	(0.91)	0.38	(0.36)	0.13	(0.12)
F (MN)	1680	(1500)	336	(273)	114	(108)	39	(36)

as compared with Figure 3.4 for a fixed boundary condition. The total force of 1680 MN was also larger than the value of 1500 MN for the fixed boundary condition.

For a variable-thickness ice floe of $\Delta t/t=0.4$, S_{rm} was still the same value for same applied compressive pack ice stress of $P=0.5$ MPa. However, P_f was 1.12 MPa (larger than 0.91 MPa) when it caused the ice first tensile failure at the same points C_2 as shown in Figure 3.9. The total force acting on the structure was 336 MN, 1.23 times larger than 273 MN for the result in the case of a fixed boundary condition. The reason for the larger applied compressive pack ice stress needed to make the ice first failure could be caused by the upward displacement of the floe in the ice/structure contact zone for a sliding boundary condition. The results for $\Delta t/t = 0.5$ and $\Delta t/t = 0.65$ were similar results to $\Delta t/t = 0.4$ as shown in Table 3.4. Larger forces were acting on the structure than those found for a fixed boundary condition. The localized maximum ice pressure at points A_2 of the ice/structure contact zone, for a variable-thickness ice floe, corresponding to the conditions of first ice failure, was also larger than values found for a fixed boundary condition.

TABLE 3.5. Results given by two-dimensional ice thickness variation on stress analysis, in which $\Delta t/t=0.5$ was assumed.

The values in the brackets under $\Delta l/l=0.25$ were from the results by uniform-thickness floe, and under $\Delta l/l=0.75$ were from the results by one-dimensional thickness variation of $\Delta t/t=0.5$. P_f : applied global pack ice compressive stress corresponding to the conditions of the ice first failure; F: total force acting on the structure. S_{rm1} : the maximum ratio of tensile stress on the top surface of the floe to P of 0.5 MPa; S_{rm2} : the maximum ratio of compressive stress on the top surface of the floe to P of 0.5 MPa.

$\Delta l/l$	0.25	(0.25)	0.5	0.75	(0.75)
S_{rm1}	0.4	(-)	1.49	2.4	(2.6)
S_{rm2}	-1.4	(-1.4)	-1.32	-1.1	(-)
P_f (MPa)	3.2	(5.0)	0.76	0.45	(0.36)
F (MN)	960	(1500)	228	135	(108)

For example, for the case of $\Delta t/t = 0.5$, the maximum ice pressure was 0.76 MPa, which was larger than the value of 0.71 MPa found for a fixed boundary condition.

3.4 Examination of the Two-dimensional Ice Thickness Variation of $\Delta l/l$

It was important and convenient to make stress analysis, using this three-dimensional finite element method, for a two-dimensional ice thickness variation as shown in Figure 2.4. The parameters used in calculations were the same as in section 3.1 but with the inclusion of the two-dimensional ice thickness variation. The value of $\Delta t/t = 0.5$ was assumed in examining the effects of the two-dimensional ice thickness variation on the stress analysis.

Results are shown in Table 3.5. The values in the parentheses under $\Delta l/l = 0.25$ were from the earlier results for the uniform-thickness ice floe of $\Delta t/t = 0.0$. The values in the parentheses under $\Delta l/l = 0.75$ were from the earlier results for the

one-dimensional ice thickness variation of $\Delta t/t = 0.5$, to give a clear comparison with two-dimensional ice thickness variation results. The result for the case of $\Delta l/l = 0.25$ is very close to a uniform-thickness ice floe, but the tensile stress occurred on the top surface of the floe at the thinnest area because of the small thickness variation. The maximum ratio of S_{rm1} , the tensile stress on the top surface of the floe, to $P = 0.5$ MPa, was $S_{rm1} = 0.4$. The most uniform-thickness part of the floe showed compressive stress on the top surface of the floe. The maximum ratio of S_{rm2} , the compressive stress on the top surface of the floe to $P = 0.5$ MPa, was $S_{rm2} = -1.4$. The ice first tensile failure occurred at point C_3 as shown in Figure 3.10, and $P_f = 3.2$ MPa caused this failure. The total force was 960 MN, which was smaller than that for a uniform-thickness ice floe (1500 MN, the value in the parentheses). For $\Delta l/l = 0.5$, S_{rm1} was equal to 1.49 and tensile stress occurred in the thinnest area at point C_3 , as shown in Figure 3.10. The compressive stress occurred on the top surface of the floe at point B_3 in the uniform-thickness area with $S_{rm2} = -1.32$. The global pack ice compressive stress of $P_f = 0.76$ MPa was needed to cause the ice first tensile failure at point C_3 . The values of S_{rm1} and S_{rm2} on the top surface of the floe are plotted in Figure 3.11, for the case of $\Delta l/l = 0.5$. Positive values of S_{rm1} , mean tensile stress, occurred in the thinnest area of the floe, and negative values of S_{rm2} occurred only in the uniform-thickness area of the floe.

The case of $\Delta l/l = 0.25$ was close to the result for a one-dimensional ice thickness variation of $\Delta t/t = 0.5$, but a smaller value of $S_{rm1} = 2.4$ was found, as compared with $S_{rm} = 2.6$, the value in the parentheses from $\Delta t/t = 0.5$. This means that smaller tensile stress occurred at the top surface of the floe. Compressive stress occurred at point B_3 . There was no compressive stress on the top surface in the thinnest area for one-dimensional ice thickness variation of $\Delta t/t = 0.5$. A global

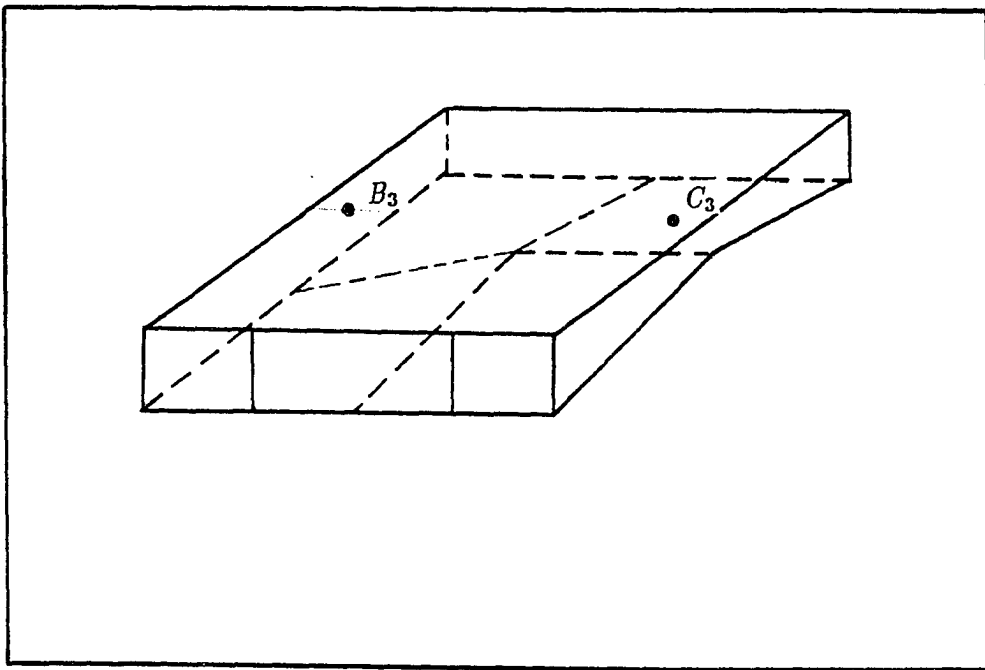


Fig. 3.10. Schematic diagram of maximum ice tensile stress computed at points C_3 . Points B_3 show a compressive stress.

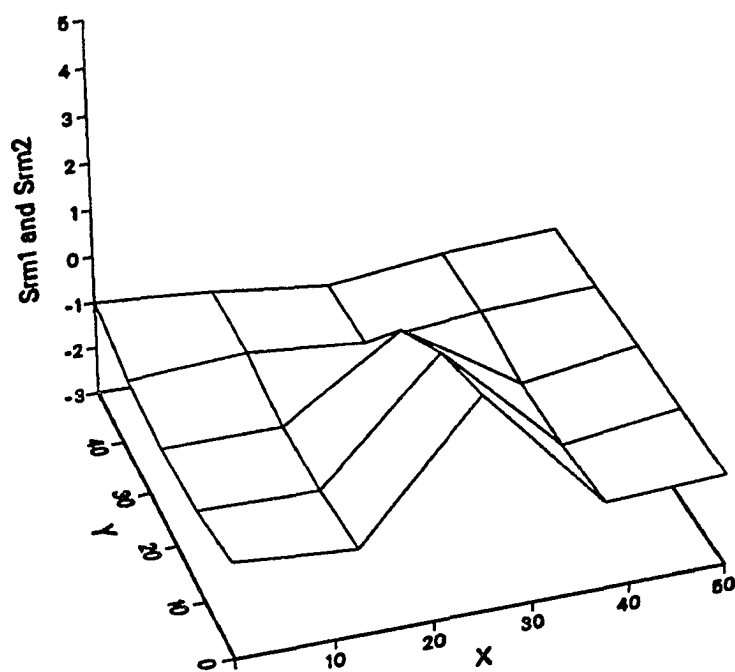


Fig. 3.11. S_{rm1} and S_{rm2} distributions on the top surface of the floe, for the case of $\Delta l/l = 0.5$. The positive value means a tensile stress, which can be seen only in the thinnest area of the floe.

pack ice compressive stress of $P_f=0.45$ MPa was needed to cause ice first failure at point C_3 . Total force acting on the structure was 135 MN.

3.5 Examination of Variable Elastic Modulus

For the calculation in section 3.1, the elastic modulus E of the ice was assumed to be a constant through the ice floe thickness dimension, with a value of 6 GPa. The examination of the effects of variations of the elastic modulus using the two-dimensional finite element method (Takeuchi, 1990) showed that the value of S_r changed very little, by less than 2.2%, as E was varied from 4 to 8 GPa. A similar result was shown in our calculations by using this three-dimensional finite element method. For that case, the value of S_r changed from 1.5% to 2.2%. However, the effect of an elastic modulus which is variable with depth is of practical interest, as discussed by Cox et al. (1984). Therefore, two results were obtained by using the three-dimensional finite element method. In two cases, the value of the elastic modulus was 6 GPa at the top surface and 3 GPa at the bottom of the ice floe, for both conditions of $\Delta t/t = 0.0$ and $\Delta t/t = 0.5$. For the case of $\Delta t/t = 0.0$, an uniform-thickness ice floe, first ice failure occurred at the top region at point A_4 , shown in Figure 3.12, at the ice/structure contact zone. An average pack ice compressive stress of 3.9 MPa caused this failure. This represented a 22% change as compared with the case for $E=6$ GPa which was constant from the top to the bottom of the ice floe. For the second case in which $\Delta t/t = 0.5$, (a variable-thickness ice floe), first tensile failure in the ice still occurred at the top surface of the thinnest area of the ice floe. The average pack ice compressive stress was only 0.25 MPa, representing a reduction of 30% as compared with the case of $E = 6$ GPa as a constant from the top to the bottom of the ice floe (in the same condition of $\Delta t/t = 0.5$). The comparison, in terms of total force on the structure, was 75

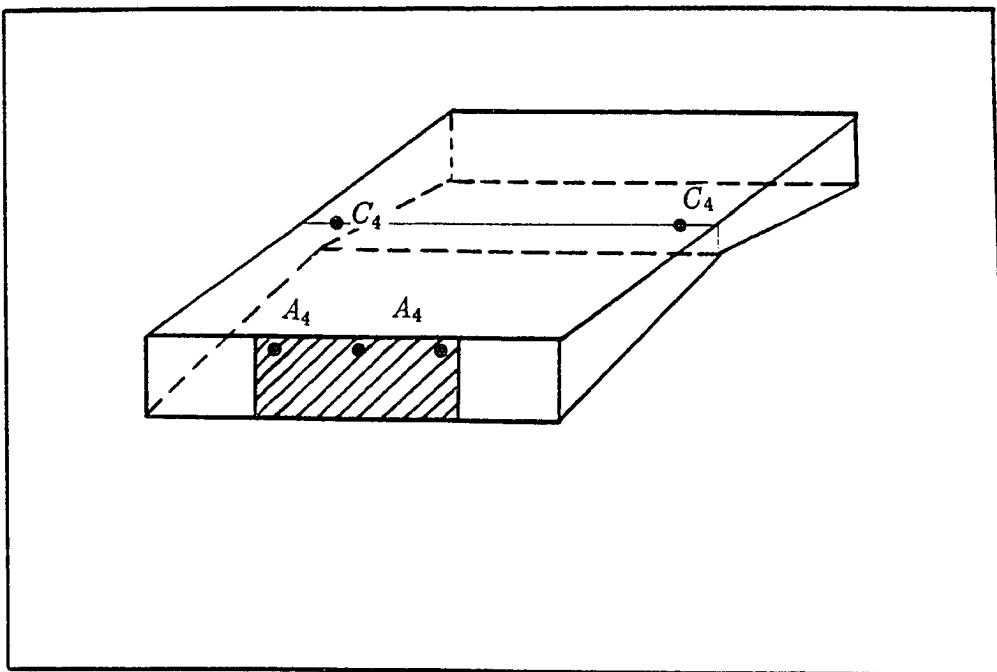


Fig. 3.12. Schematic diagram of localized maximum ice pressure computed at the points A_4 regions of the ice/structure contact zone, and maximum ice tensile stress computed at points C_4 .

MN as compared with 108 MN for $E = 6$ GPa (constant with depth). This is a reduction factor of 1.44, and the ratio of reduction as compared with the uniform thickness floe is a factor of 15.6. This may partially explain the disparity of results between model-scale tests and field tests for ice/structure interaction.

3.6 Examination of the Effect of a Change of $t_1/t = 0.5$

The results presented above were given for the pack ice/ice floe loading condition over the full vertical height, $t_1/t=1$, as shown in Figure 3.13 (a). The examination was also made of a change of $t_1/t=0.5$ as shown in Figure 3.13 (b), in which the vertical region over which the averaged global pack ice compressive stress was applied was taken as a half thickness of the ice floe. Results corresponding to the case of $t_1/t=0.5$, are shown in Table 3.6. The values in the parentheses are from the results for $t_1/t=1$. For an uniform-thickness floe of $\Delta t/t=0.0$, S_{rm} was -1.16, which means that a lower compressive stress occurred on the top surface of the floe for the same case of $P=0.5$ MPa, as compared with the result of $S_{rm} = -1.4$ for $t_1/t = 1$. The $P_f = 7.2$ MPa needed to cause the ice first failure at points A_5 , as shown in Figure 3.14, was 1.44 times larger than the value of $P_f = 5.0$ MPa for $t_1/t = 1$. However, the total force of $F = 1035$ MN acting on the structure for $t_1/t = 0.5$ was smaller than the value $F = 1500$ MN for $t_1/t=1$. Thus, the contact zone between the test floe and the pack ice can cause a reduced load on the structure. It is very interesting to note that for the variable-thickness floes with $\Delta t/t=0.4$ and $\Delta t/t=0.5$, there was no tensile stress at the top surface of the floe for $P=0.5$ MPa. In this case $S_{rm} = -1.1$ and $S_{rm} = -0.9$, respectively, as shown in Table 3.6. The $P_f = 4.6$ MPa and $P_f = 3.8$ MPa, respectively, for both cases of $\Delta t/t = 0.4$ and 0.5 , were needed to cause ice first failure at the bottom area of the floe in the

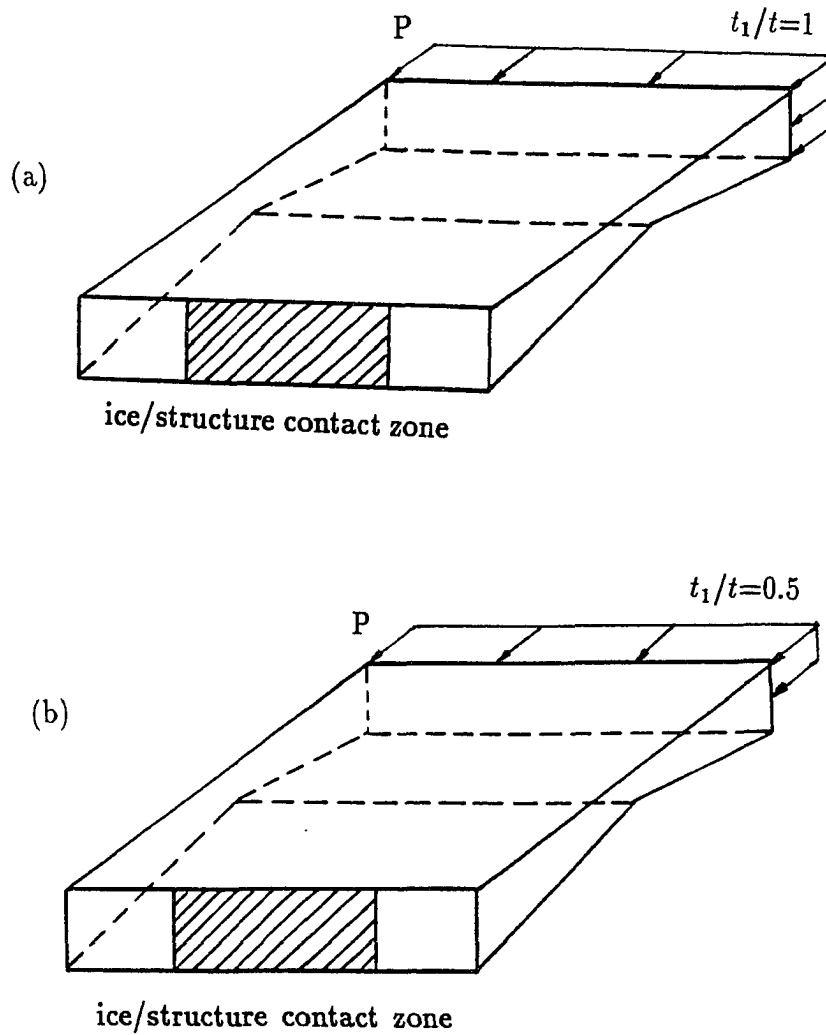


Fig. 3.13. (a) the loading condition was taken as an averaged global pack ice compressive stress; $t_1/t=1$; (b) the loading condition was taken as a half thickness of the ice floe for the averaged global pack ice compressive stress; $t_1/t=0.5$.

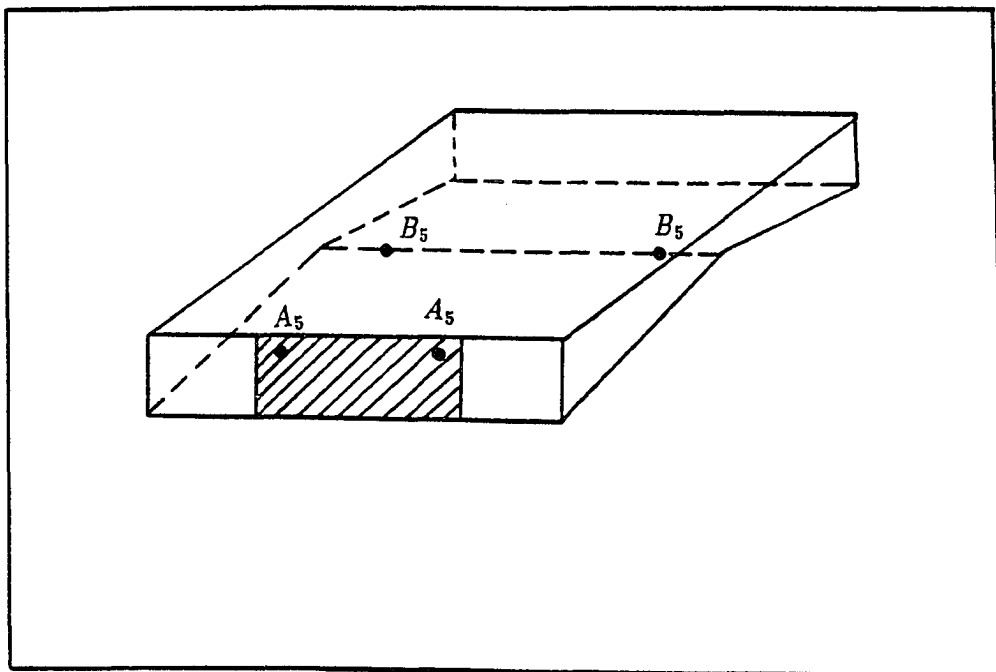


Fig. 3.14. Schematic diagram of localized maximum ice pressure computed at the points A_5 regions of the ice/structure contact zone, and maximum ice compressive stress computed at points B_5 for variable-thickness ice floe.

TABLE 3.6. Results given by the loading condition of a change of $t_1/t=0.5$.

The values in the brackets were from the results for $t_1/t=1$. P_f : applied global pack ice compressive stress corresponding to the conditions of the ice first failure; F: total force acting on the structure; S_{rm} : the maximum ratio of stress on the top surface of the floe to P of 0.5 MPa. (Negative value means a compressive stress).

$\Delta t/t$	0.0	(0.0)	0.4	(0.4)	0.5	(0.5)	0.65	(0.65)
S_{rm}	-1.16	(-1.4)	-1.2	(1.2)	-0.9	(2.6)	0.01	(9.3)
P_f (MPa)	7.2	(5.0)	4.6	(0.91)	3.8	(0.36)	2.9	(0.12)
F (MN)	1035	(1500)	690	(273)	570	(108)	435	(36)

thinnest area of point B_5 , as shown in Figure 3.14. The total force acting on the structure was $F = 690$ MN and $F = 570$ MN, respectively, which are 2.53 and 5.27 times larger than the results of $F = 273$ MN and $F = 108$ MN, respectively, for the case of $t_1/t=1$. Thus, the contact zone can cause an increased load as well, in some circumstances.

For $\Delta t/t=0.65$, when $P=0.5$ MPa, S_{rm} presents a slight tensile stress, the value being 0.01, much smaller than $S_{rm} = 9.3$ for $t_1/t=1$. However, $P_f = 2.9$ MPa, the value which caused ice first failure. Failure was located at the point B_5 , a compressive failure. (The tensile stress at the top surface of the floe in the thinnest area was not enough to cause tensile failure). The total force acting on the structure in this case was $F = 435$ MN, which was 12.1 times larger than the $F = 36$ MN for $t_1/t=1$. Still, a force reduction factor of 2.4 may be recognized for $t_1/t = 0.5$ as compared with a uniform-thickness floe with the total force $F = 1035$ MN as shown in Table 3.6.

3.7 Examination of Viscoelastic Ice Behavior

These calculations using the three-dimensional finite element method for viscoelastic ice behavior were done to extend the results of the two-dimensional finite element results (Takeuchi, 1990) to three dimensions. To examine the viscoelastic behavior of the ice floe, the applied pack ice compressive stress was assumed to be a long-term loading, such as that produced by an average wind stress. Creep will ultimately dominate the deformation, so that the elastic elements contribute only a minor amount to the total strain. In calculations for this type of loading, the material response can be assumed and represented by the Maxwell model as shown in Figure 2.10, which consists of a spring and dashpot in series, where the dashpot follows the nonlinear Glen's Law for the flow of ice with a constant stress:

$$d\varepsilon/dt = A\sigma^B$$

where ε is strain, t is time, σ is stress, and A and B are constants. Because there are no data available for the constants which are applicable to multiyear ice, the constants A and B for granular fresh ice (Sanderson, 1988) were used and taken as $A = 1.32 \times 10^{-25}(P_a)^{-3} \times (Sec)^{-1}$ and $B = 3$. The constant elastic modulus was taken as $E = 6$ GPa in the calculations. The creep stage of the deformation was assumed to take place at constant volume, for ease of computation.

The results of calculations done using the viscoelastic stress-strain law, for $\Delta t/t = 0.65$, are shown in Figure 3.15, Figure 3.16 and 3.17. In Figure 3.15, the quantities S_{rt} and S_{rb} are a function of time, and are the ratios between the stress on the top and bottom surface, respectively, in the thinnest area of the floe, to the applied global pack ice compressive stress of $P = 0.5$ MPa. Each time step was taken as 200 seconds. The loading condition was taken as $t_1/t = 0.5$. The value of S_{rt} at time $t = 0$ was the solution to the elastic problem which can be seen in Table 3.6. The value of $S_{rm} = 0.01$ for $\Delta t/t = 0.65$, and S_{rm} was the maximum ratio

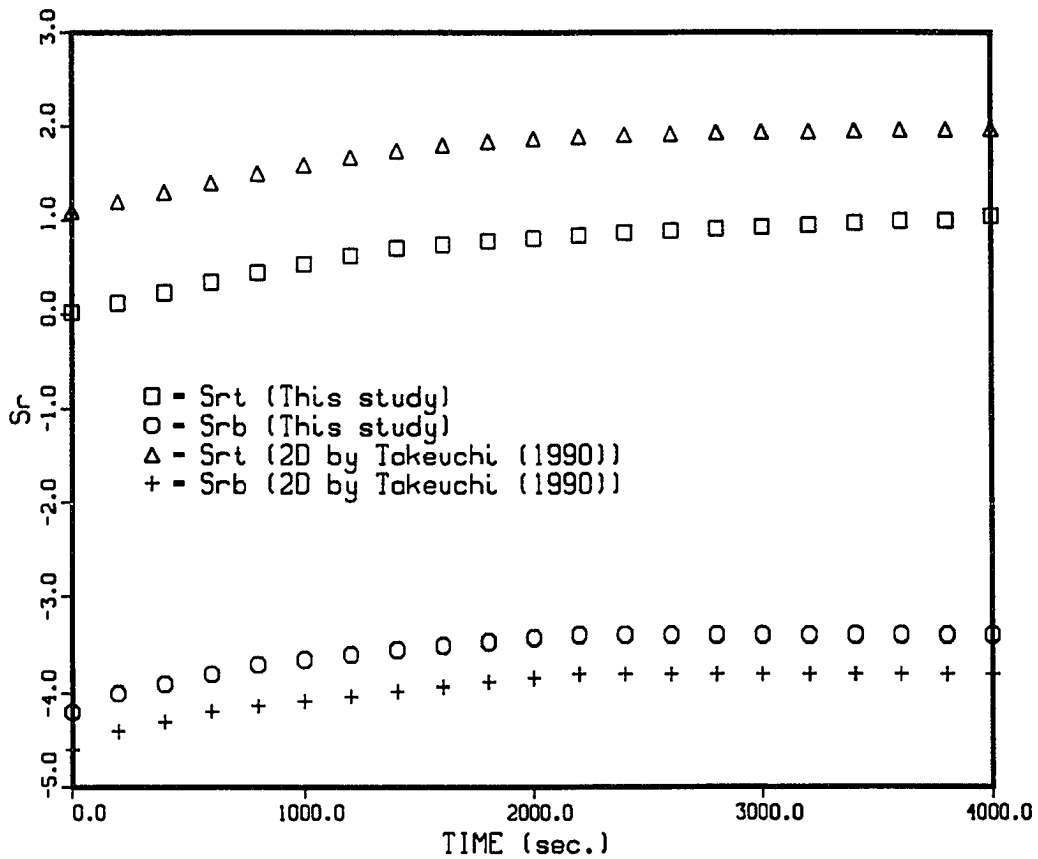


Fig. 3.15. Stress ratio S_r as a function of time in seconds for $\Delta t/t=0.65$ and $t_1/t=0.5$, time step is equal to 200 seconds. S_{rt} is obtained from the top surface of the ice floe, and S_{rb} is obtained from the bottom surface of the ice floe.

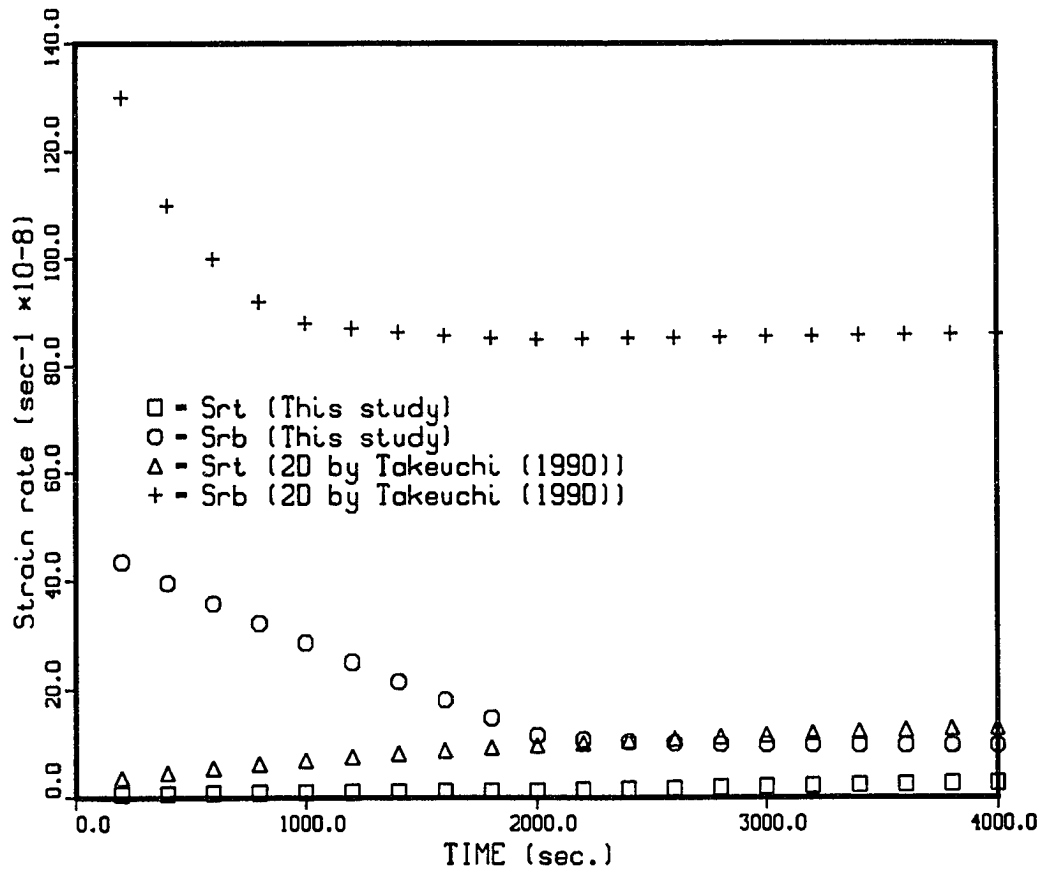


Fig. 3.16. Strain rate as a function of time for $\Delta t/t = 0.65$ and $t_1/t = 0.5$, time step is equal to 200 seconds. Strain rate was in $Sec.^{-1}$.

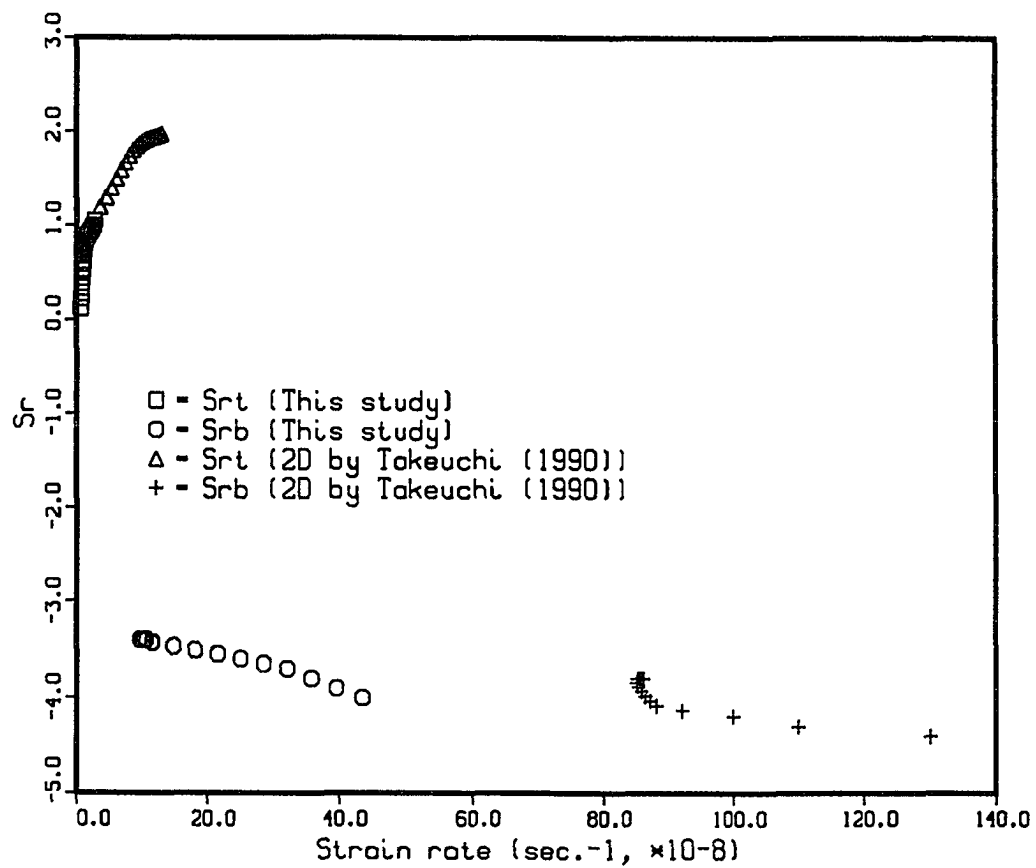


Fig. 3.17. Stress ratio S_r as a function of strain rate for $\Delta t/t = 0.65$ and $t_1/t = 0.5$, time step is equal to 200 seconds.

of stress on the top surface of the floe to $P = 0.5$ MPa for that elastic solution. Subsequent points in Figure 3.15 show the effect of creep deformation at each time step over the time intervals. The comparison was also made with earlier the two-dimensional results (Takeuchi, 1990) in Figure 3.15. The quantity S_{rt} is tensile and varies little from the elastic solution (at $t=0$), but is monotonically increasing at the end of the run at $t=4000$ seconds. A smaller tensile stress was found in this study than in the earlier two-dimensional computation, perhaps because of the thickness/roughness difference between the two studies. A value of $\Delta t/t = 0.667$ was used by Takeuchi (1990), but in this study, $\Delta t/t = 0.65$ was used. The tensile stress is expected to increase with the thickness/roughness increase.

In contrast, S_{rb} was compressive, and gradually decreased in magnitude throughout the run. It is possible that failure would eventually be initiated in compression at the base of the thin area of the floe, rather than in tension at the top.

In Figure 3.16 and 3.17, the strain rate is given as a function of time. Also, S_r is given as a function of strain rate, from the same simulation as produced the results in Figure 3.15. The highest strain rate reached in the calculations was about $43.5 \times 10^{-8} \text{sec}^{-1}$ as shown in Figure 3.16 and 3.17. This was a lower strain rate as compared with the results of Takeuchi (1990).

The summary is given in Figure 3.17 on the quantities S_{rt} and S_{rb} , as a function of strain rates, with the same time function (time step = 200 seconds, from $t=0$ to $t=4000$ seconds). The results for S_{rt} in this study showed smaller tensile stress at the top surface of the floe. For S_{rb} , this study showed smaller compressive stress on the bottom surface of the floe. Lower strain rates were also seen, as compared with the results by Takeuchi (1990). This perhaps was due to the thickness roughness difference of 0.017 as discussed before.

In Figure 3.18, 3.19 and 3.20, the results are shown of a calculation with the same value of $t_1/t = 0.5$, but with a smaller thickness variation of $\Delta t/t = 0.5$.

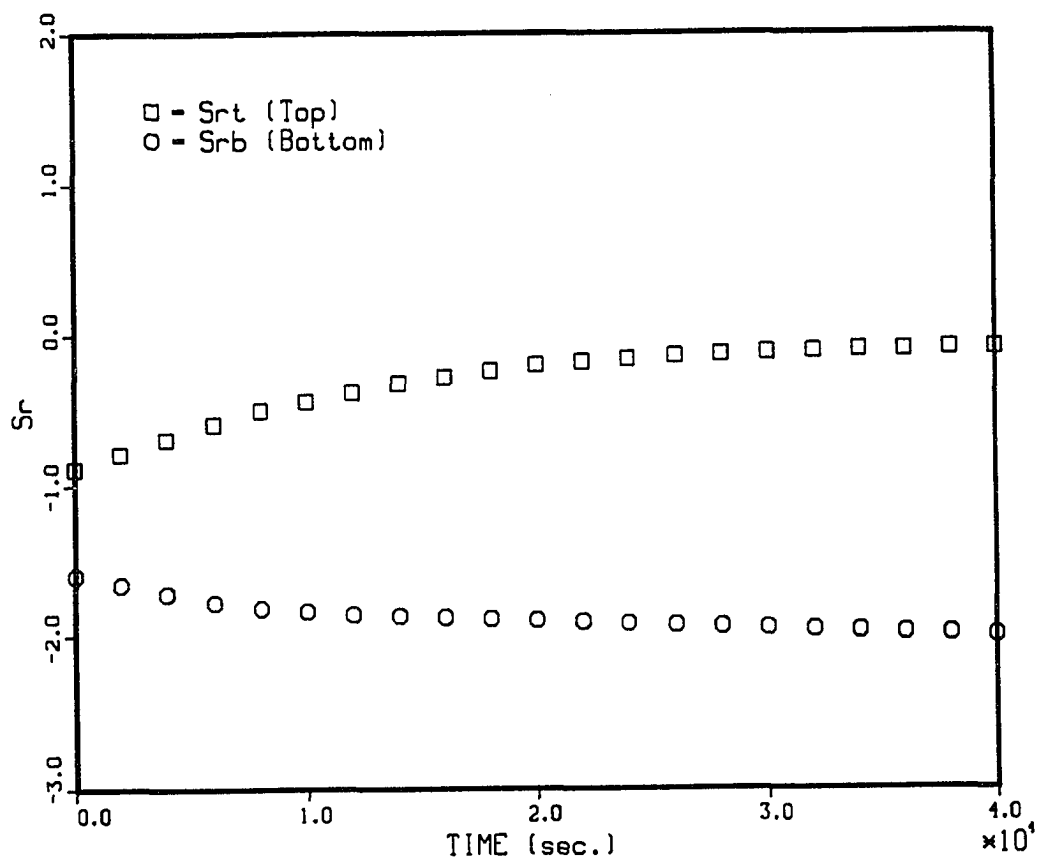


Fig. 3.18. Stress ratio S_r as a function of time for $\Delta t/t=0.5$ and $t_1/t=0.5$, time step is equal to 200 seconds. S_{rt} is obtained from the top surface of the ice floe, and S_{rb} is obtained from the bottom surface of the ice floe.

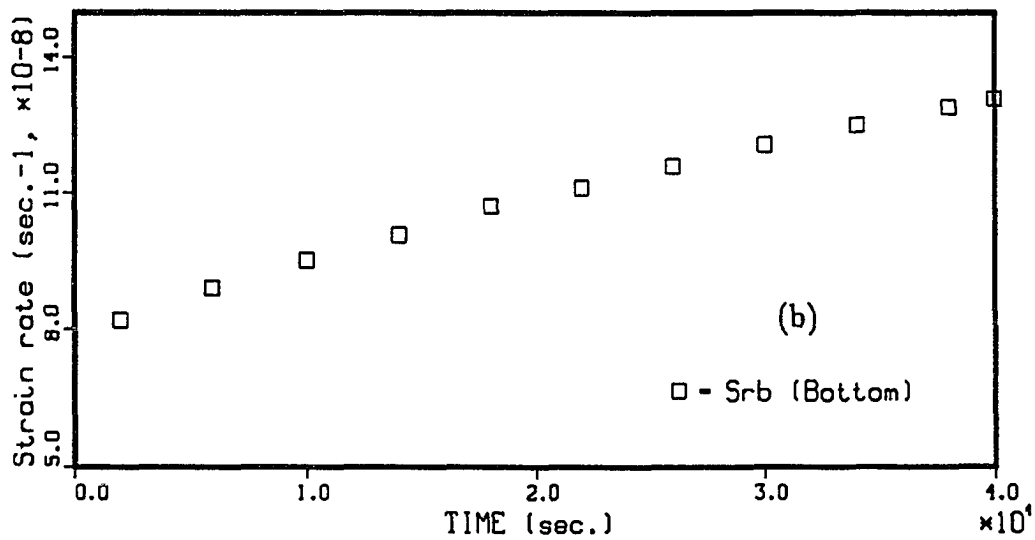
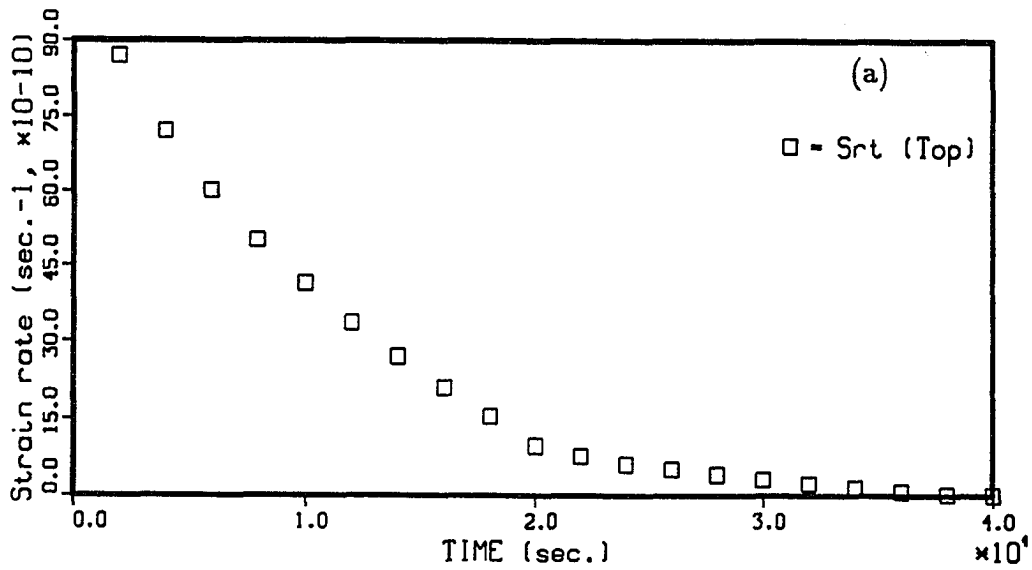


Fig. 3.19. Strain rate as a function of time for $\Delta t/t = 0.5$ and $t_1/t = 0.5$, time step is equal to 200 seconds. Strain rate was in sec.^{-1} .

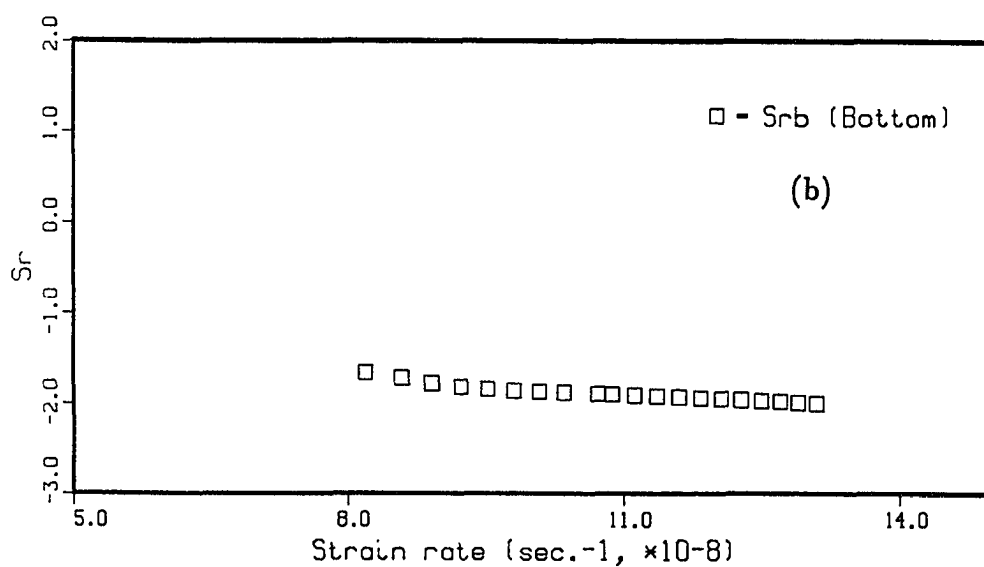
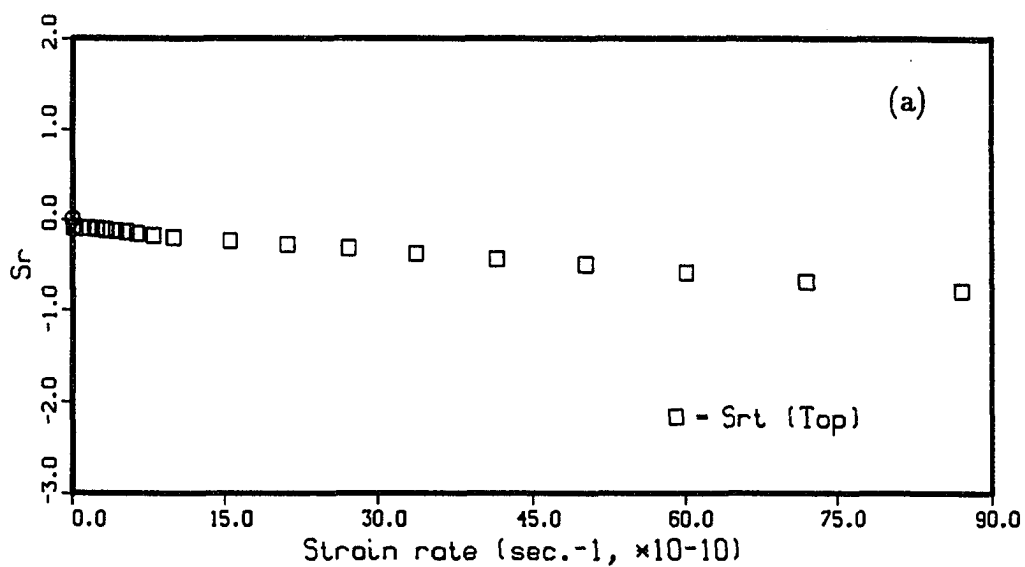


Fig. 3.20. Stress ratio S_r as a function of strain rate for $\Delta t/t = 0.5$ and $t_1/t = 0.5$, time step is equal to 200 seconds.

The S_{rt} and S_{rb} as a function of time were shown in Figure 3.18. S_{rt} was a compressive stress at $t = 0$ of $S_{rt} = -0.9$ and slightly increasing, but S_{rb} was slightly decreasing. Both had a lower strain rate (Figure 3.19) compared with the case of larger thickness variation of $\Delta t/t = 0.65$ (Figure 3.16). This may be caused by the decreased $\Delta t/t$ and slower strain rate. The ice floe would ultimately fail in compression.

In all cases of the calculations done using the viscoelastic stress-strain law, when the viscoelastic behavior is happening, the stresses in the floe depend on the viscoelastic material strains with time. The forces acting on the structure increase with time until the material fails. The material strains with time are the dominant factor in the analysis of the stress, under the condition of the applied global pack ice compressive stress.

3.8 Results of Comparison by using other Failure Criteria

The failure criteria used in most of this study were simply the maximum value of compression, 8 MPa, and the maximum value of tension, 1 MPa. One trial using a more complete failure criterion given by Riska and Frederking (1987), as discussed in Chapter 2, was done by applying equation (2-1). The averaged values of coefficients of F_{11} , G_{1111} , G_{1122} and G_{1212} given by Riska and Frederking (1987), were used, which are 0.862, 0.334, -0.106 and 0.22, respectively. The result shows a slightly smaller load acting on the structure than that found by using the simple failure criterion. This one trial comparison is for the case of $\Delta t/t = 0.0$, ice structure contact zone located in the central region, loading condition of $t_1/t=1$, constant elastic modulus of $E=6$ GPa, and fixed boundary condition. The results using this complex failure criterion showed that the total force acting on the structure was 1398 MN, which is smaller than the value of 1500 MN obtained with

TABLE 3.7. Results comparison with two failure criteria.

S_c : using simple failure criterion; C_c : using complex failure criterion by equation (2-1); F: total forces acting on the structure in MN; D: difference of total forces obtained by using both failure criteria; S: percent value for relationships between using S_c and C_c .

	S_c	C_c
F (MN)	1500	1398
D		102
S		6.8%

the simple failure criterion. The comparison is made in Table 3.7. The difference in the total force acting on the structure, using both criteria, is 102 MN. So, there is only a change of 6.8% by using a complex criterion, and the result is smaller than that obtained by using the simple criterion. If the calculations involved high values of $\Delta t/t$, and tensile stresses were dominant, the complex failure criterion could be expected to modify these results more significantly.

CHAPTER 4

Analysis of an Ice Floe Acting against a Compliant Structure

Results given for an ice floe interacting with a interaction of a rigid structure have been described in **Chapter 3**. It is of interest to consider an ice floe pushing against a compliant structure and foundation. A time-variable formulation was used. Elastic deformation of the structure wall, and viscoelastic seafloor sediment response beneath the structure, were assumed. Results for the deformation of the structure and the foundation were analyzed by the same finite-element method.

4.1 Finite Element Model of the Structure and Foundation

The finite element model of the structure and foundation is shown in Figure 4.1, in which the geometric sizes and foundation finite element meshes are also defined. The structure with a size of 25 m by 25 m, with an 11.0 m height beneath the bottom of the ice floe, was considered, and the ice floe thickness in the ice/structure contact zone was taken as 6 m, which is the same consideration as in Chapter 3. The distance of 11.0 m from bottom of the ice floe to the sea floor resulted from the water depth of 16 m. The $50m \times 50m \times 6m$ size of the floe was assumed. The density of sea water was 1028 kg/m^3 corresponding to the temperature of -1.7°C and salinity of 32 parts per thousand (Sanderson,1988). An averaged density for multiyear ice of 846 kg/m^3 (Cox and Richter-Menge, 1985) was used. The ice floe model incorporates a one-dimensional thickness variation as shown in Figure 2.3. Values of $\Delta t/t=0.0$, (a uniform-thickness ice floe), and $\Delta t/t=0.5$, (a variable-thickness ice floe), were used to determine the maximum force acting on the structure for both cases. The stress in the floe was also analyzed. The foundation with 40 m depth and 145 m width was taken, as shown in Figure 4.1.

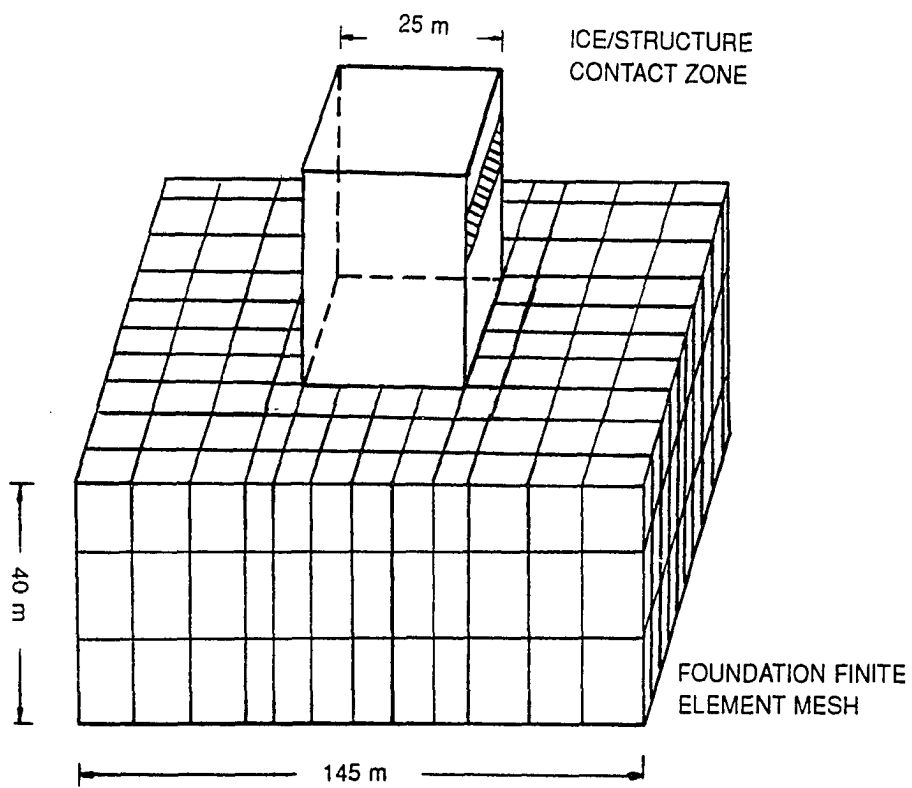


Fig. 4.1. Finite element model of the structure and the foundation.

TABLE 4.1. Parameters used in the calculations for the structure and foundation. E_s and E_f : Young's modulus of the structure and foundation; ν_s and ν_f : Poisson's ratio of the structure and foundation; M_s and M_f : mass density of the structure and the foundation

E_s (MPa)	2.0×10^4
ν_s	0.15
M_s (kg/m ³)	2450
E_f (MPa)	130
ν_f	0.333
M_f (kg/m ³)	1750

The parameters used in the calculations are the same as those shown in Table 2.1 for $\Delta t/t=0.0$ and $\Delta t/t=0.5$ for the ice floe model. Parameters for the structure and the foundation are presented in Table 4.1.

The elastic modulus E_s , Poisson's ratio ν_s and mass density M_s of the structure are taken as $E_s = 2.0 \times 10^4$ MPa, $\nu = 0.15$ and $M_s = 2450$ kg/m³, which are based upon a gravity steel structure (Zienkiewicz et al., 1978). The elastic modulus E_f , Poisson's ratio ν_f and mass density M_f of the the foundation are taken as $E_f = 130$ MPa, $\nu = 0.333$ and $M_f = 1750$ kg/m³, which are based upon typical seafloor sediments and viscoelastic soil features (Pande and Zienkiewicz, 1982). These assumptions were applicable to the subsea soil condition in the Beaufort Sea with the friction angle of 30° as discussed by Prodanovic (1979).

The applied average pack ice compressive stress was assumed to vary in 0.05 MPa (started from 0.2 MPa at the second time step of $t = 0.5$ sec.) and 0.1 MPa increments (started from 4.8 MPa at the second time step of $t = 1$ sec.) in the calculations for $\Delta t/t=0.5$ and $\Delta t/t=0.0$. The time step was assumed to vary in 0.5 seconds (in the case of $\Delta t/t = 0.5$) and 1 second (in the case of $\Delta t/t = 0.0$)

increments to examine the stress in the ice floe, the deformation of the structure, the maximum force acting on the structure and the deformation of the foundation.

4.2 Stress in the Ice Floe and Maximum Force Acting on the Structure

In Figure 4.2, the result for the maximum stress in the ice floe as a function of time, which is the tensile stress occurring on the top surface in the thinnest area of the floe (shown in Figure 4.3, points C), is shown for a variable-thickness ice floe of $\Delta t/t=0.5$. It can be seen that at $t=0$, when the structure did not contact the ice, the stress in the floe was zero. Upon contact, the stress in the ice became very large until the ice failed in tension at the thinnest place in the ice floe. The time of fracture of the floe was $t = 3$ seconds. During the first 0.5 seconds, the stress changed significantly as shown in Figure 4.2. However, for a uniform-thickness ice floe of $\Delta t/t=0.0$, the stress became compressive (a negative value) and the results are shown in Figure 4.4. The stress at points A and B of the ice/structure contact zone, shown in Figure 4.3, was increasing as shown in Figure 4.4. The stress increased as a function of time as shown in Figure 4.4. The stress lasted for a longer time than in the previous case of a variable thickness of ice floe (0.5 second). Compressive failure occurred in the ice floe when the time of fracture of the floe was 7.5 seconds. To compare both results of $\Delta t/t=0.5$ and $\Delta t/t=0.0$, the time elapsed to ice failure was longer for a uniform-thickness ice floe, than for a variable-thickness ice floe. The former was a compressive failure and the latter was a tensile failure. The same results were seen in Chapter 3 without the time function included.

The initial force acting on the structure was zero, and the maximum force in the first case was 118 MN at the failure time of $t = 3$ seconds. The force as a function of time for $\Delta t/t = 0.5$ is plotted in Figure 4.5. It is evident that the

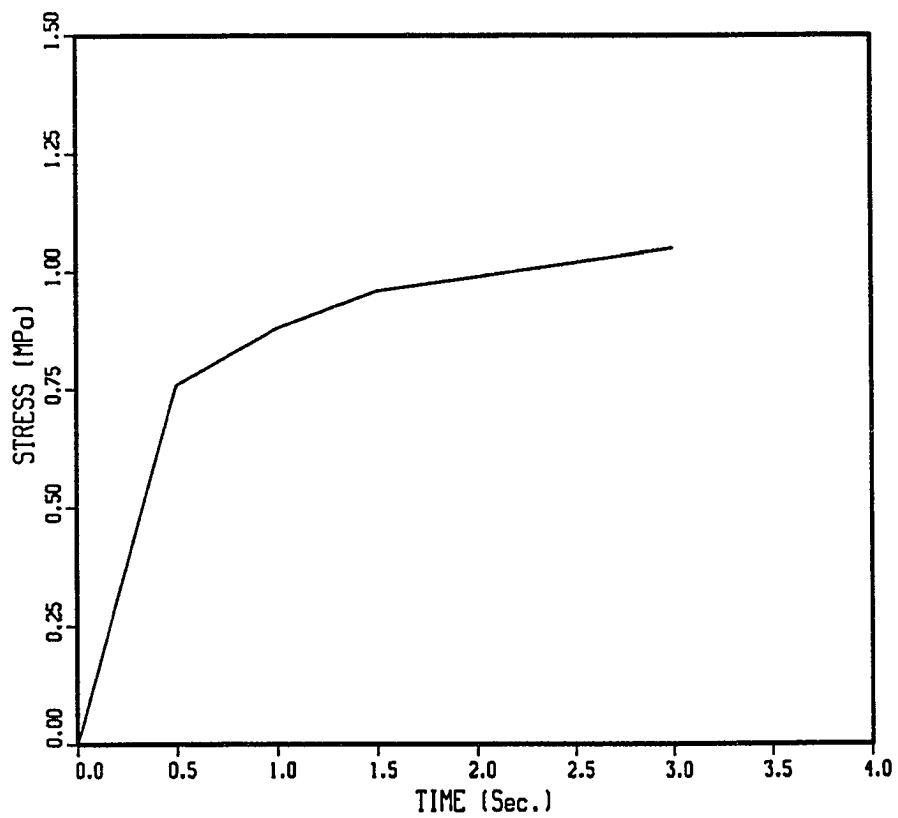


Fig. 4.2. The tensile stress in the ice floe at point C (Figure 4.3) as a function of time for variable thickness of $\Delta t/t=0.5$. Time of fracture of the floe was 3 seconds.

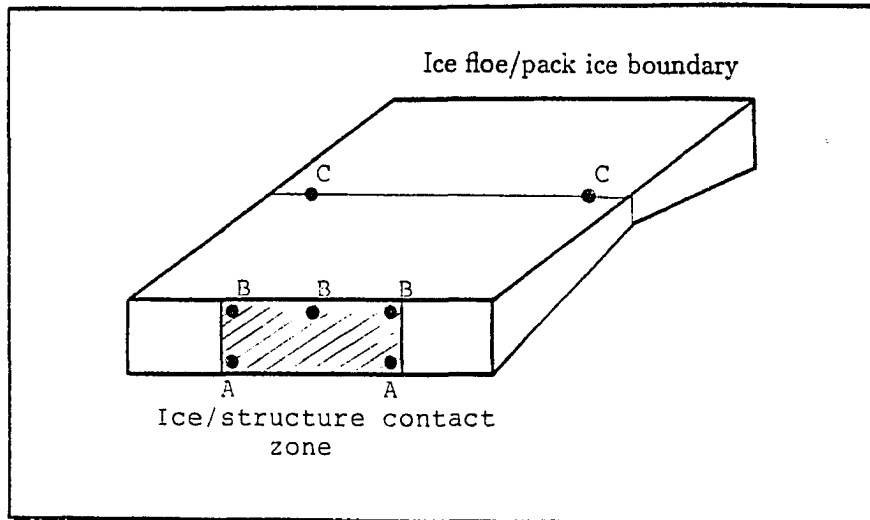


Fig. 4.3. Schematic diagram of structure localized maximum ice pressure computed at the points A and B regions of the ice/structure contact zone, and maximum ice tensile stress computed at points C.

forces acting on the structure rapidly changed from zero to the maximum load. In this study, a quasi-static analysis was used, and the acceleration, and period vibration of the structure were not included.

The maximum force acting on the structure as a function of time for $\Delta t/t = 0.0$, an uniform thickness of ice floe, is plotted in Figure 4.6. The value of maximum force was 1620 MN, which is much larger than that obtained for the variable thickness ice floe. About 7.5 seconds were required to reach the peak value. The ice floe failed in a compressive failure at points A and B (Figure 4.3) in the ice/structure contact zone.

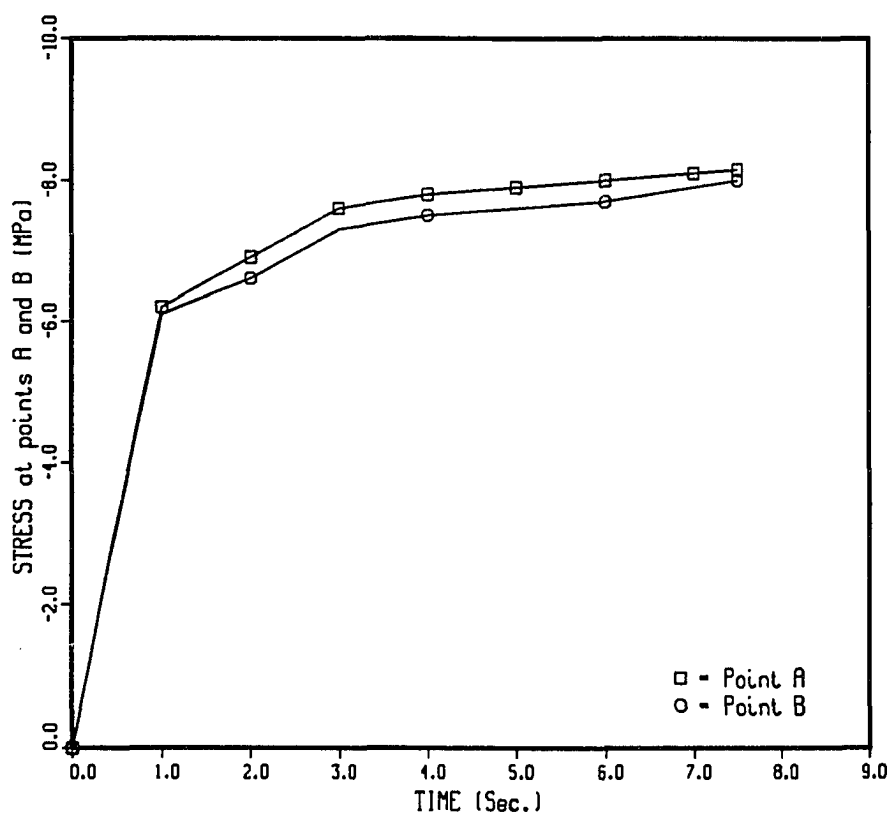


Fig. 4.4. The compressive stress in the ice floe at points A and B (Figure 4.3) as a function of time for uniform thickness of $\Delta t/t=0.0$. The time of fracture of the floe was 7.5 seconds.

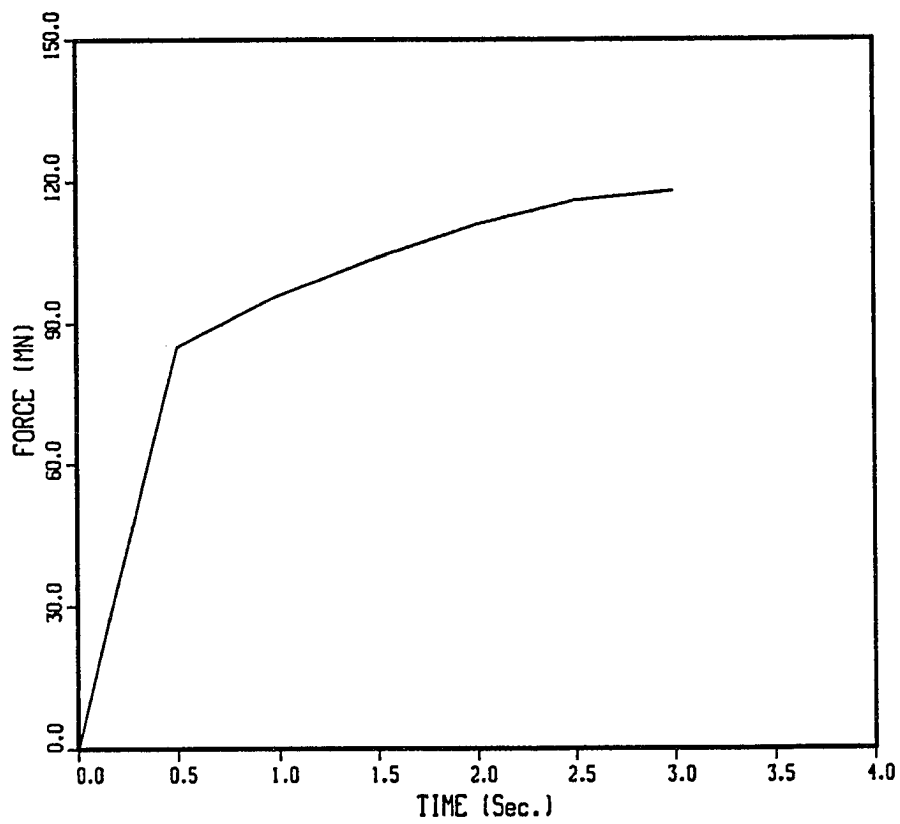


Fig. 4.5. The forces acting on the structure as a function of time for $\Delta t/t=0.5$.

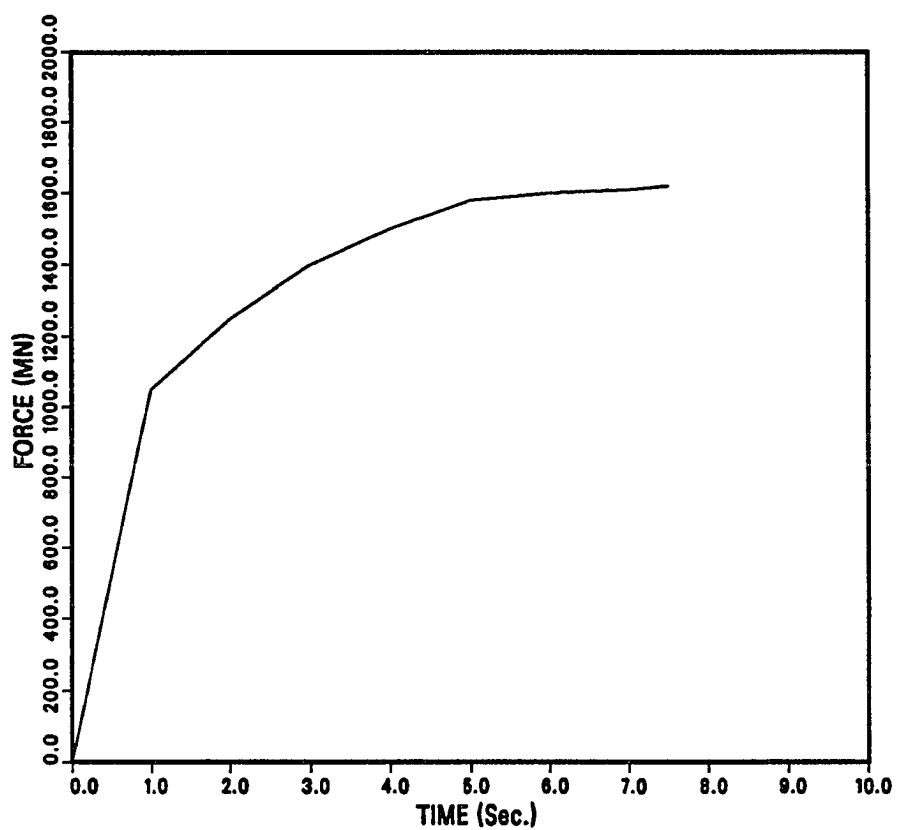


Fig. 4.6. The forces acting on the structure as a function of time for $\Delta t/t=0.0$.

4.3 Total Force on the Structure as a Function of the Deformation of the Structure

The total force acting on the compliant structure is presented in Figure 4.7 for the case of $\Delta t/t = 0.5$, a variable-thickness ice floe. It is evident that the total force acting on the structure increased as the deformation of the structure increased. The maximum displacement within the structure itself in the ice floe/structure contact zone was located at points D as shown in Figure 4.8. The displacement was 0.033 m at the time corresponding to the ice first tensile failure, at which the maximum force of $F = 118$ MN acted on the structure. The displacements of the structure at points E were nearly the same as at points D, but smaller by 0.5%, which are due to the deformation of the structure itself.

The displacement of the structure at point D was also plotted as a function of time in Figure 4.7 (b). The maximum displacement occurred at time $t = 3$ seconds, when the maximum force acted on the structure.

In Figure 4.9 (a), the total force acting on the structure as a function of displacement of the structure is for the case of $\Delta t/t = 0.0$. Results were similar to Figure 4.7 for $\Delta t/t = 0.5$, but the difference was that the total force acting on the structure, and the displacement at points D (Figure 4.8), were much larger. The maximum force acting on the structure in this case was $F = 1620$ MN, which is 14.2 times larger than the value for force due to an ice sheet of variable-thickness. The maximum displacement of the structure (at the same point D) was 0.112 m, which is 3.39 times larger than the displacement for an ice sheet of variable-thickness. The ice experienced compressive failure, and at that time the maximum ice force of $F = 1620$ MN occurred. In Figure 4.9(b), the displacement of the structure at points D (Figure 4.8) is plotted as a function of time for this case of $\Delta t/t = 0.0$. The maximum displacement of 0.112 m occurred at $t = 7.5$ seconds.

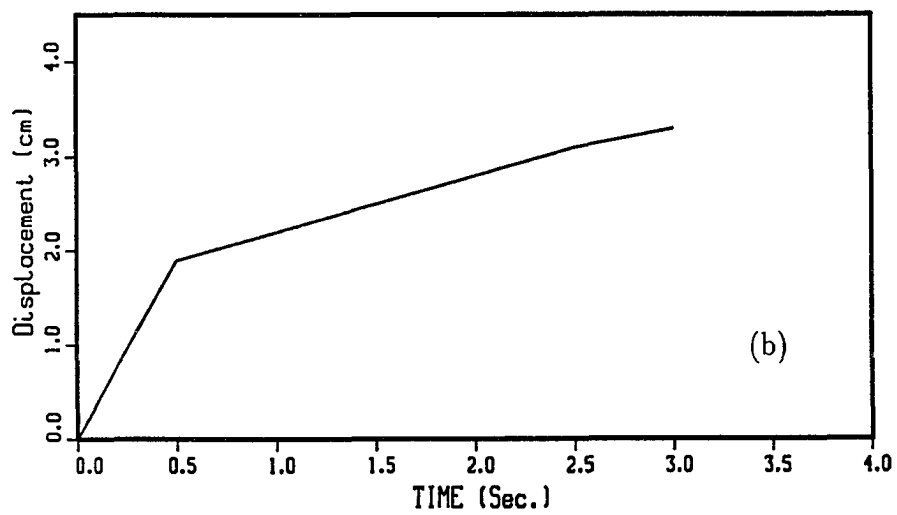
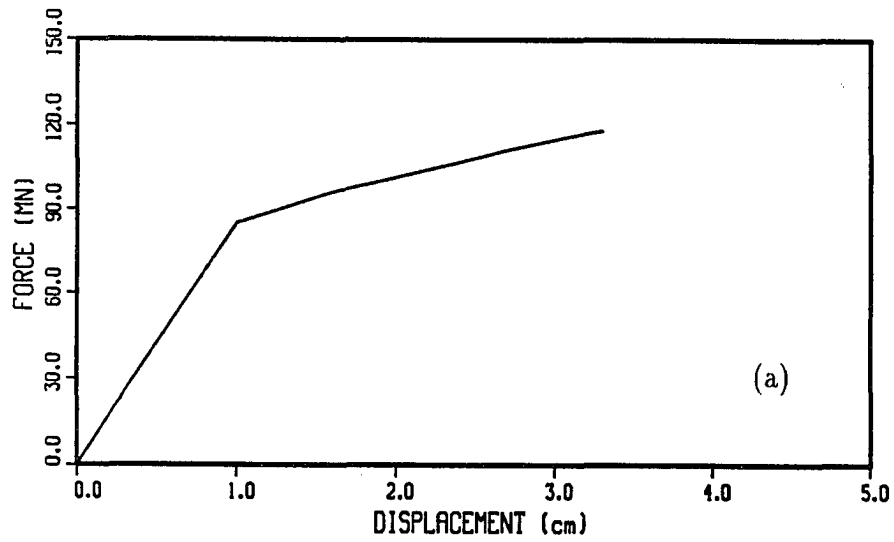


Fig. 4.7. (a) Ice forces action on the structure as a function of deformation of the structure for the case of $\Delta t/t=0.5$; (b) displacement of the structure at point D (Figure 4.8) as a function of time.

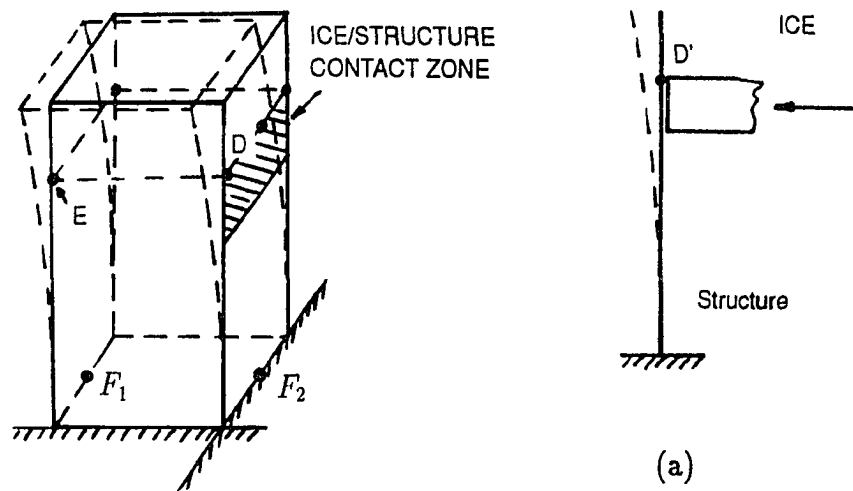


Fig. 4.8. The results of displacements in Figures 4.7 and 4.9 are located at points D in the ice/structure contact zone.

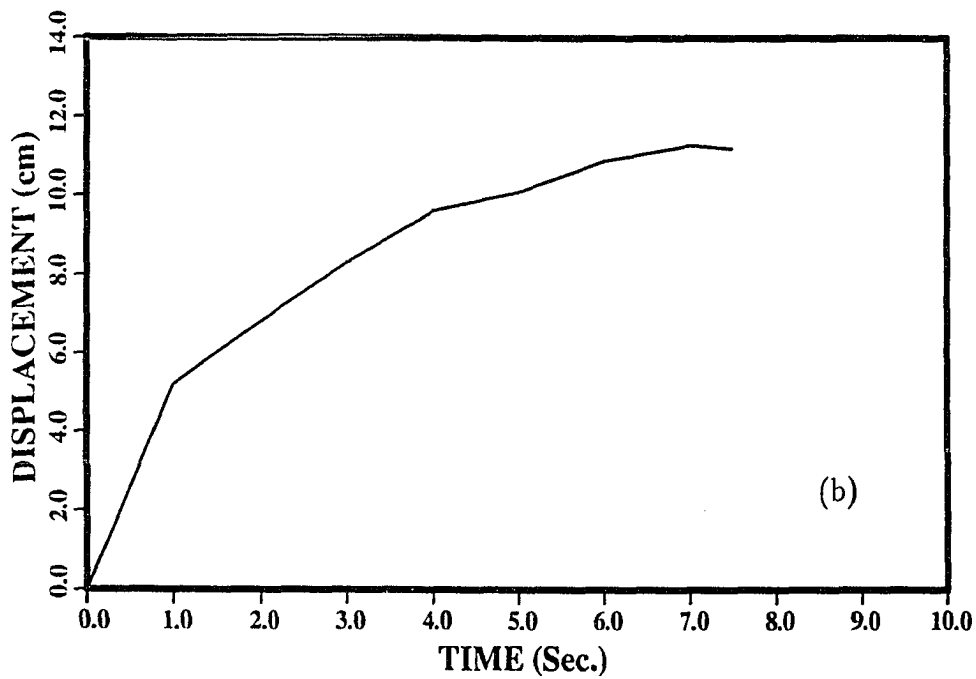
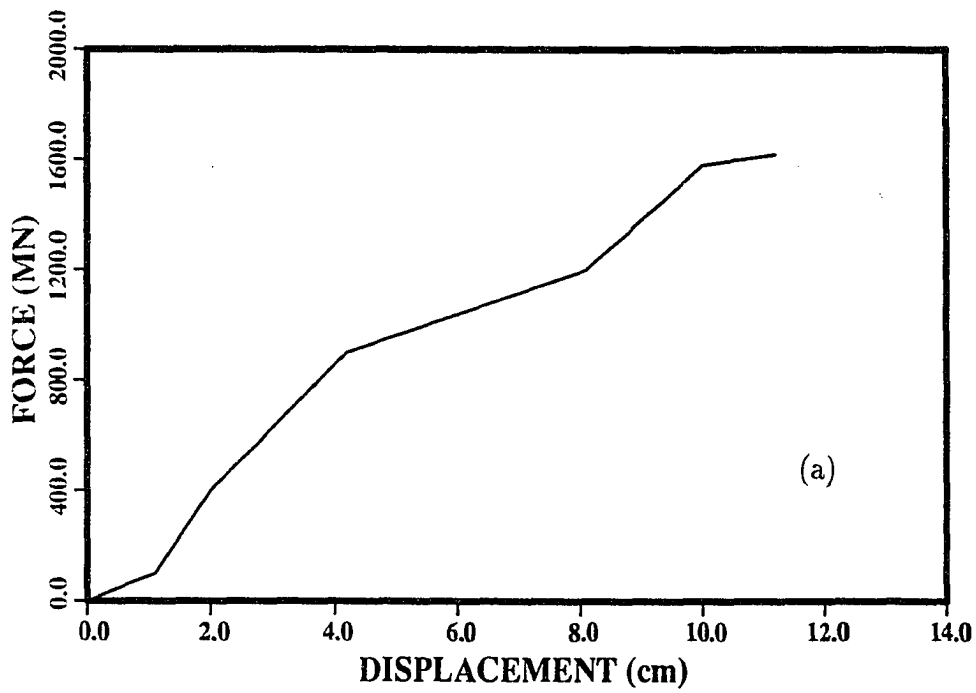


Fig. 4.9. (a) Ice forces acting on the structure as a function of deformation of structure for the case of $\Delta t/t=0.0$; (b) displacement of the structure at point D (Figure 4.8) as a function of time.

4.4 Deformation of the Foundation

At the time of the maximum force acting on the structure and the maximum displacement of the structure wall, one may present the maximum deformation of the foundation. The vertical displacements during the maximum ice load are shown in Figure 4.10 (a), and horizontal displacements during the maximum ice loads are shown in Figure 4.10 (b) for the case of $\Delta t/t=0.5$. The illustration is given as a two-dimensional deformation at the centerline of the foundation, due to the symmetry of the foundation. The dashed lines in the Figure are the idealized deformation, and the points are outputs from the calculations. The maximum vertical displacement occurred at point F_1 (Figure 4.8), which is 0.11 m as shown in Figure 4.10 (a). The maximum vertical displacement was located on the side of the structure foundation opposite the ice floe, at point F_1 as shown in Figure 4.8. The vertical displacement at F_1 was 1.22 times larger than that at point F_2 . The maximum horizontal displacement was 0.019 m, shown in Figure 4.10 (b), and was also located at point F_1 . The horizontal displacement at point F_2 , as shown in Figure 4.10 (b), was nearly the same as at point F_1 , as would be expected for lateral ice forces.

The vertical and horizontal displacements at points F_1 (Figure 4.8) in this case of $\Delta t/t=0.5$, are plotted as a function of time in Figure 4.11 (a) and (b). When $t = 3$ seconds was reached the maximum vertical and horizontal displacements occurred, corresponding to the first ice failure and to the maximum force acting on the structure.

In Figure 4.12 (a) and (b), the vertical and horizontal displacements are shown for the case of $\Delta t/t=0.0$, a uniform-thickness ice floe. The maximum vertical displacement was 0.23 m at the location of point F_1 (Figure 4.8), which is 2.09 times larger than the case of $\Delta t/t=0.5$, a variable-thickness ice floe. The maximum horizontal displacement at point F_1 was 0.081 m, which is 4.26 times larger than

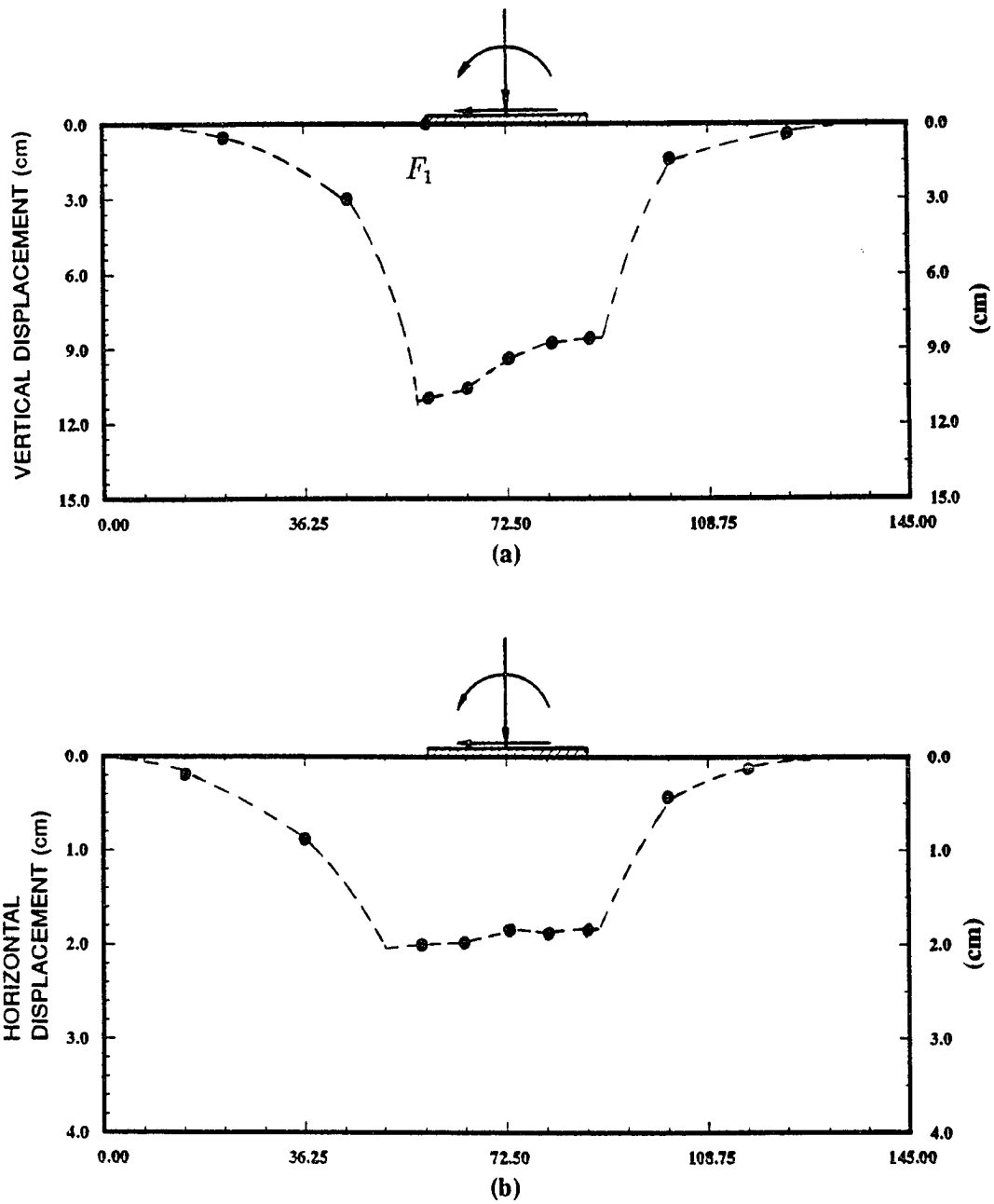


Fig. 4.10. The vertical and horizontal deformation of the foundation for the case of $\Delta t/t=0.5$. The horizontal axis of the figure presents the width of the foundation as shown in Figure 4.1. (a) vertical displacement beneath the bottom of the structure; (b) horizontal displacement beneath the bottom of the structure.

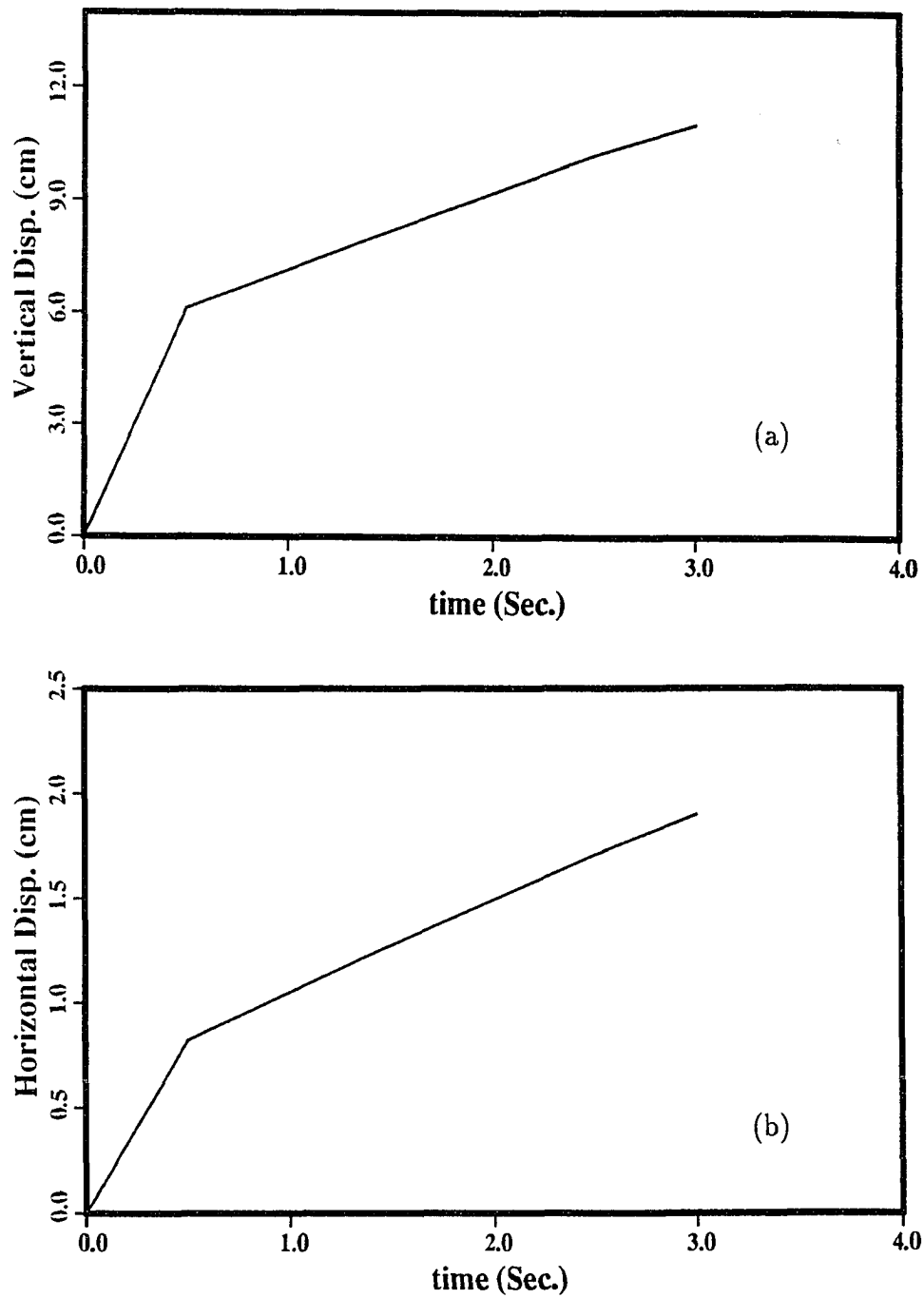


Fig. 4.11. The vertical and horizontal displacements at point F_1 (Figure 4.8) as a function of time for the case of $\Delta t/t=0.5$, (a) vertical displacement; (b) horizontal displacement.

that for the case of $\Delta t/t=0.5$. However, the deformations for both cases presented a similar pattern. One may compare the idealized deformation from the dashed lines in both Figures 4.10 and 4.12. Also, the deformation of the structure is small from the value of the displacement at point D, Figure 4.8 because of the horizontal displacement of the foundation. The maximum displacement of the structure itself is only 0.014 m for the case of $\Delta t/t=0.5$, and 0.031 m for the case of $\Delta t/t=0.0$. The corresponding cases gave maximum horizontal foundation displacements of 0.019 m and 0.081 meter.

The vertical and horizontal displacements at point F_1 (Figure 4.8) in this case of $\Delta t/t=0.0$, as a function of time, were shown in Figure 4.13 (a) and (b). When $t = 7.5$ seconds was reached the maximum vertical and horizontal displacements occurred, corresponding to the first ice failure and the maximum force acting on the structure.

Results on the deformation of the structure and the foundation have been presented in this Chapter. Two cases of $\Delta t/t = 0.5$ and $\Delta t/t = 0.0$ for the ice floe against the structure were considered. In the case of $\Delta t/t = 0.5$, a variable-thickness ice floe, the maximum force of $F = 118$ MN acted on the structure, corresponding to the ice floe first tensile failure. For that case, the maximum displacement of the structure was 0.033 m, and the maximum horizontal and vertical displacements of the foundation were 0.019 m and 0.11 m, respectively. In the case of $\Delta t/t = 0.0$, a uniform-thickness ice floe, the maximum force of $F = 1620$ MN acted on the structure, corresponding to the ice floe first compressive failure. For this second case, the maximum displacement of the structure was 0.112 m, and the maximum horizontal and vertical displacements of the foundation were 0.081 m and 0.23 m, respectively. The maximum deformations of the structure itself were 0.014 m and 0.031 m, respectively, because of the horizontal displacement

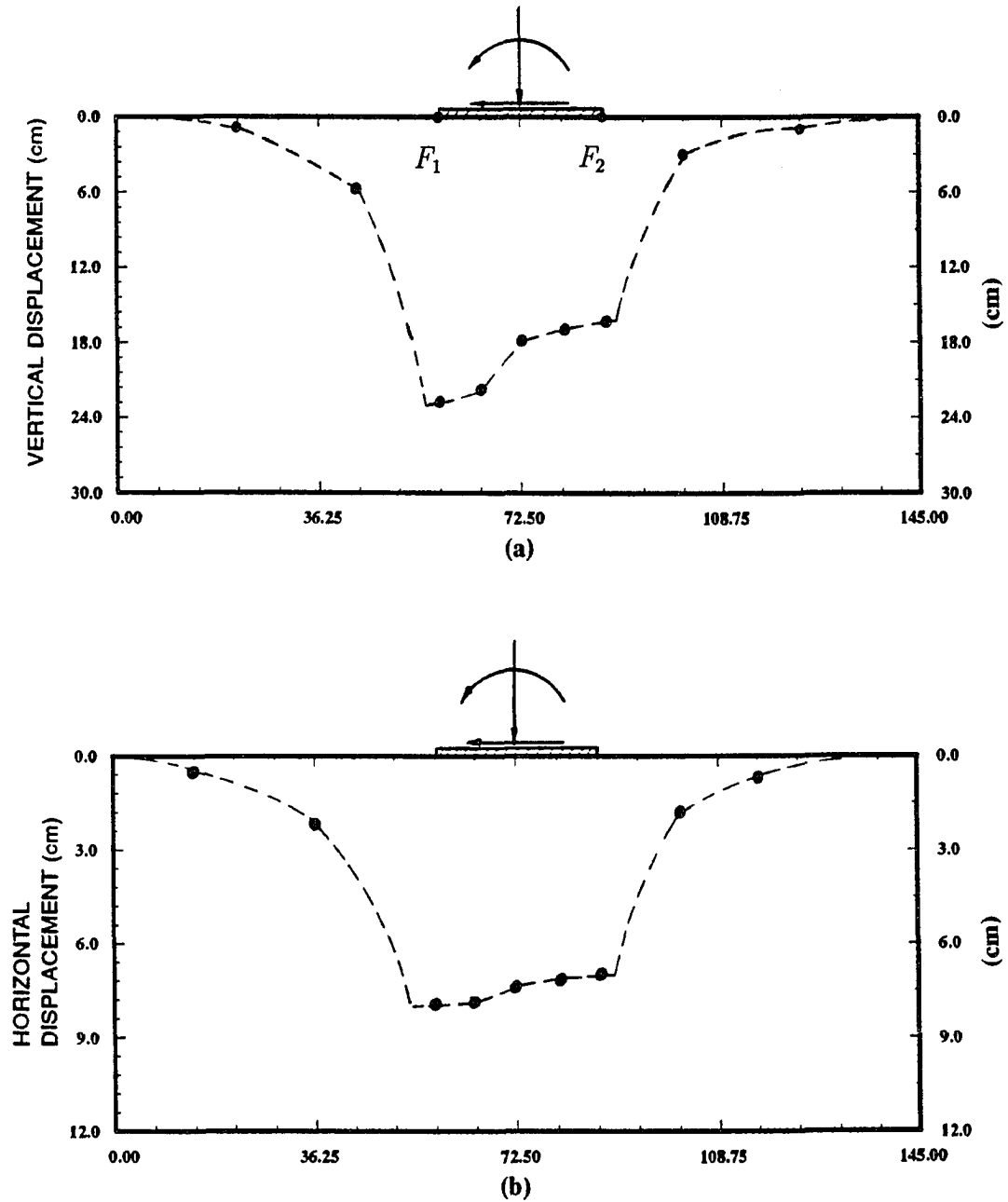


Fig. 4.12. The vertical and horizontal deformation of the foundation for the case of $\Delta t/t=0.0$. The horizontal axis of the figure presents the width of the foundation as shown in Figure 4.1. (a) vertical displacement beneath the bottom of the structure; (b) horizontal displacement beneath the bottom of the structure.

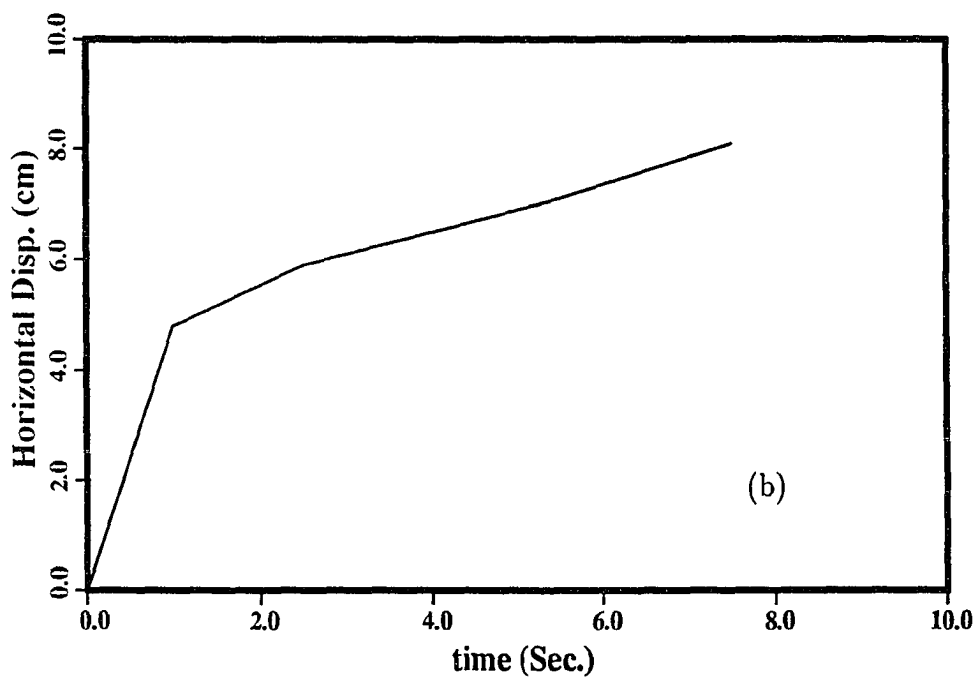
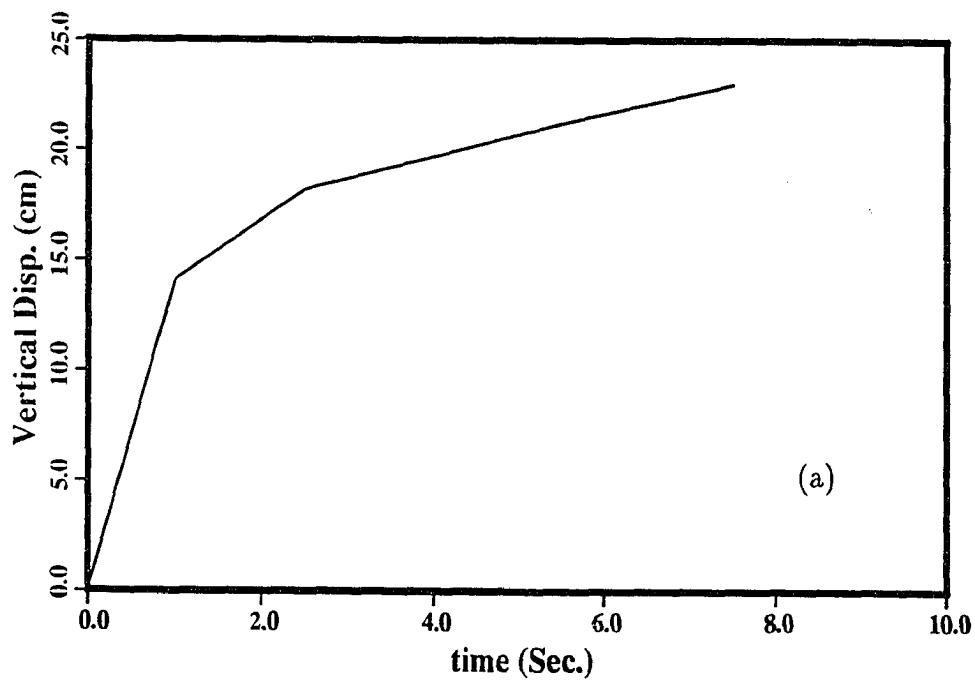


Fig. 4.13. The vertical and horizontal displacements at point F_1 (Figure 4.8) as a function of time for the case of $\Delta t/t=0.0$, (a) vertical displacement; (b) horizontal displacement.

of the foundation. It is interesting to note that the total ice floe forces acting on the compliant structure structure/foundation were 8% larger than those for a perfectly rigid structure. This may be due to a slightly different geometry at the ice/structure interface. However, the rigid structure approximation appears to be quite useful in preliminary design activities, with only the final design requiring the full compliant structure/foundation model.

CHAPTER 5

Analysis of Ice Island Forces on a Cylindrical Structure

5.1 Introduction

The most massive ice features in the Arctic Ocean are the natural ice islands or tabular icebergs which occasionally break off the ice shelves located on the north coast of Ellesmere Island, N. W. T., Canada (Sackinger and Jeffries, 1986). Because of their size, drift and longevity in the Arctic Ocean Beaufort Gyre, ice islands are recognized as a hazard to offshore petroleum development in the coastal waters of the Beaufort Sea and Chukchi Sea. With regard to the possible interaction of ice islands with offshore structures, recent research has focussed on ice island numbers, morphology and remote sensing (Sackinger and Yan, 1986; Jeffries and Sackinger, 1989), dynamics, motion and recurrence intervals (Lu, 1988; Li et al., 1989), physical structural characteristics and stratigraphy (Sackinger and Jeffries, 1987), and mechanical properties (Sackinger and Jeffries, 1986; Frederking et al., 1988; Jeffries et al., 1990).

The largest natural ice island presently known in the Arctic Ocean is the Hobson's Choice ice island, which broke off the East Ward Hunt Ice Shelf in 1982-83. The ice island has an area of almost 34 km^2 , a mass exceeding 700×10^6 tones and a thickness of up to 42.6 m (Jeffries et al., 1988).

The first published data on ice island mechanical properties were for several constant cross-head-rate uniaxial compressive strength tests at a nominal strain rate of $1 \times 10^{-5} \text{ s}^{-1}$ on specimens from the upper surface of the Hobson's Choice Ice Island (Frederking et al. 1988). Constant cross-head-rate uniaxial compressive strength tests at nominal strain rates of $1 \times 10^{-3} \text{ s}^{-1}$ and $1 \times 10^{-5} \text{ s}^{-1}$ on very old sea ice and brackish ice from the Ward Hunt Ice Shelf also have been reported (Jeffries et al., 1988). Subsequently, Jeffries et al. (1990) reported a preliminary analysis

of the constant strain rate (from $2 \times 10^{-7} s^{-1}$ to $1 \times 10^{-3} s^{-1}$) uniaxial compressive failure stress and failure modulus. Failure modulus (E_f) values range from 0.50 GPa to 6.59 GPa.

However, very few studies on ice island/structure interactions for the analysis of ice island forces against the structure have been published. It is the purpose of this study to present a preliminary analysis of such ice island loads. Both methods of theoretical analysis and three-dimensional finite element method calculations were used. An ice island model of 3000 m in length, 2500 m in width and 20 m in depth, as shown in Chapter 2 was assumed, and was impacted against a cylindrical rigid structure of a diameter of 150 m. To check size effects of the ice island, a smaller ice island model of $2500m \times 2000m \times 15m$ was also considered in the theoretical studies.

5.2 Theoretical Analysis of the Ice Island Loads Acting upon a Cylindrical Structure

Using theoretical analysis, there are many plausible and quite highly developed methods for calculating ice loads under a variety of loading conditions. All of them involve certain sets of assumptions. It is considered in this theoretical study that the analysis of dynamic impact involves progressive penetration and a growing area of contact during the impact process. The maximum penetration of an impacting floe, and hence its maximum contact area, depends on its initial kinetic energy and the rate at which this energy is dissipated during the impact process, as formulated by Sanderson (1988).

When an ice island impacts with a structure, the large mass of the ice island is travelling with a large amount of kinetic energy. The total force $F(x)$ as a function of penetration distance x can be given by (Sanderson, 1988)

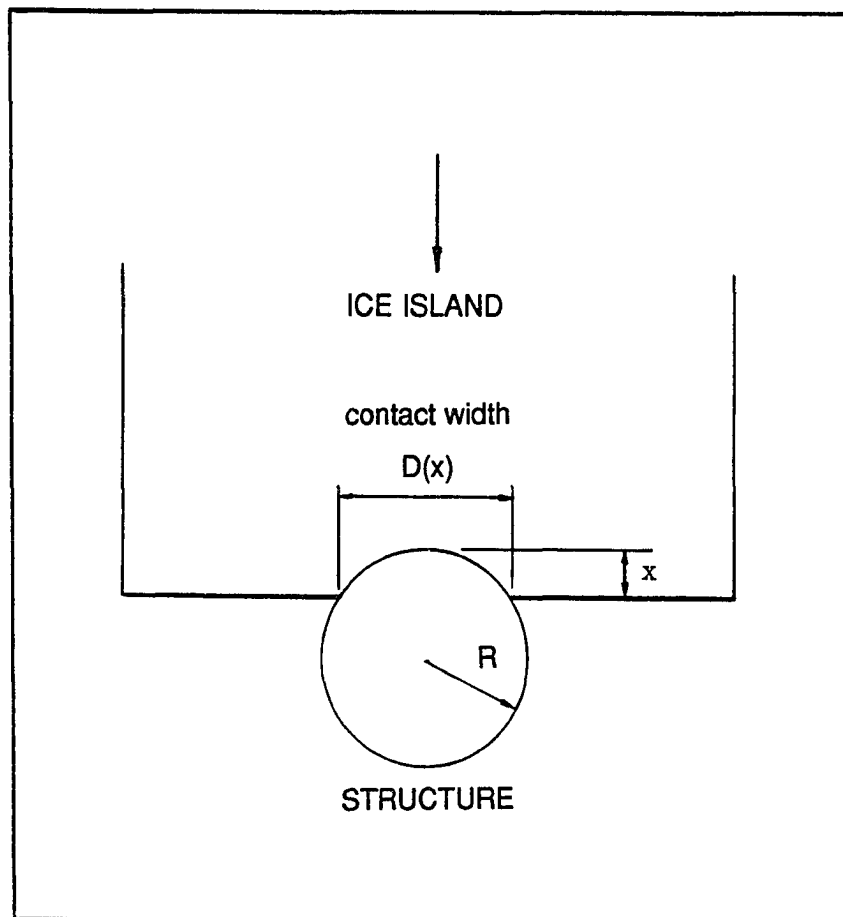


Fig. 5.1. Simplified interaction geometry for analytic model of progressive penetration.

$$F(x) = \bar{\sigma}(A) \times A(x), \quad (5-1)$$

where $F(x)$ is the total force exerted when the ice island has moved a distance x into the structure after the first contact, $A(x)$ is the contact area, and $\bar{\sigma}(A)$ is thus defined by this equation as the mean equivalent stress associated with this contact area achieved after penetration by a distance x . In Figure 5.1, the simplified interaction geometry for the analytical model of progressive penetration is shown, from which the contact width $D(x)$ can be written as

$$D(x) = 2\sqrt{x(2R - x)}, \quad (5-2)$$

where R is the radius of the cylindrical structure. The contact area $A(x)$ can be given by

$$A(x) = D(x) \times h, \quad (5-3)$$

where h is the thickness of the ice island. Substitution of equations (5-2) and (5-3) into equation (5-1) allows $F(x)$ to be rewritten as

$$F(x) = \bar{\sigma}(A) \times 2\sqrt{x(2R - x)} \times h. \quad (5-4)$$

During the collision process a widening area $A(x)$ of contact develops between the structure and the ice island as shown in Figure 5.1, and its kinetic energy is gradually absorbed until the ice island comes to rest or passes the structure. During the process of penetrating, the penetration distance x as a function of time elapsed t can be obtained. If the ice island impacts with a initial speed of $V_0(t)$ at time $t = 0$ changing to a speed of $V(t)$ at time t after a penetration distance x , then the initial kinetic energy can be set equal to the work done for the penetration distance x , plus the remaining kinetic energy; this can be written as

$$\frac{1}{2}M(V_0(t))^2 = \int_0^x F(x) dx + \frac{1}{2}M(V(t))^2, \quad (5-5)$$

where M is the mass of the ice island; (the effects of hydrodynamic added mass should be taken into account because of the large mass of the ice island and will be discussed later). When the ice island comes to rest, $V(t)$ is equal to zero, and the maximum penetration distance X_{max} is reached.

The mean equivalent stress of $\bar{\sigma}(A)$ in equations (5-1) and (5-4) can be approximately given by (Sanderson, 1988)

$$\bar{\sigma}(A) = \lambda_m \sigma_m \sqrt{A_0/A(x)}, \quad (5-6)$$

an empirical law, where λ_m is a factor expressing the average ratio of mean load to peak loads, and σ_m is the mean normalized stress at peak load over area A_0 . Sanderson (1988) showed the data for full-scale sea ice measurements of indentation pressure at peak load as a function of contact area with an offshore structure. If normalized to a reference area $A_0 = 100m^2$, then the data have a mean normalized stress σ_m of 0.92 MPa and a standard deviation of $\sigma_s = 0.45$ MPa. Because there is no data on ice island interaction with structures, the results of $A_0 = 100m^2$, $\lambda_m = 2/3$ and $\sigma_m = 0.92MPa$ for full scale sea ice measurements (Sanderson, 1988) will be used as a approximation to be substituted into our calculations. The shear stress at the ice island/structure interface, and the strain-rate dependence of ice strength, were neglected.

Substituting equation (5-4) and (5-6) into equation (5-5), we have

$$\frac{1}{2}MV_0^2 = \lambda_m \sigma_m \sqrt{A_0} \int_0^x \sqrt{2(x(2R-x))^{1/2} h} dx + \frac{1}{2}M\left(\frac{dx}{dt}\right)^2. \quad (5-7)$$

To solve this differential equation of (5-7), a numerical method using a computer program as shown in Appendix was applied. Results of the penetration distance

x as a function of elapsed time t are shown in Figure 5.2, obtained by solving equation (5-7). Values used were $h = 20$ m, $R = 75$ m, $\lambda_m = 2/3$, $\sigma_m = 0.92$ MPa, and $A_0 = 100m^2$. To examine the effects of the initial speed V_0 of the ice island when it just contacts the structure ($t=0$ and $x=0$), four different magnitudes of V_0 were considered in the calculations as shown in Figure 5.2, from which it can be seen that the magnitude of penetration distance x increases with elapsed time t . Also, penetration depends significantly on the initial speed V_0 of the ice island. For example, for $V_0=0.2$ m/s, the longest time elapsed t_{max} was 106 seconds and the maximum penetration distance X_{max} was 13.2 m. However, for $V_0=0.575$ m/s, the longest elapsed time t_{max} was 212 seconds and the maximum penetration distance X_{max} was about 75 m as shown in Figure 5.2.

The speed of the ice island as a function of the penetration distance x , and as a function of the time elapsed t , were also solved by equation (5-7) and plotted in Figure 5.3. It can be seen that the speed of the ice island decreased from the initial speed at $t=0$, until it came to rest and the penetration distance x reached a maximum value.

The results as shown above were found using the mass of $M = 1.305 \times 10^{11}$ kg, of the ice island alone. This was obtained by using a density of $870kgm^{-3}$ (Jeffries et al., 1988), and the length of 3000 m, the width of 2500 m and the depth of 20 m in this ice island example. It is valuable to present a comparison of this result with the effects if hydrodynamic added mass is included. The added mass is an effective mass associated with a body accelerating or decelerating in a fluid, and is caused by the changes that are necessary to the surrounding flow field as the body's motion alters. Luk (1983) described two types of hydrodynamic responses to a prescribed ice floe movement: (1) the hydrodynamic frequency response to a periodic motion of an ice floe, and (2) the hydrodynamic unit function response to an instantaneous change of the floe velocity. Many methods to determine the added

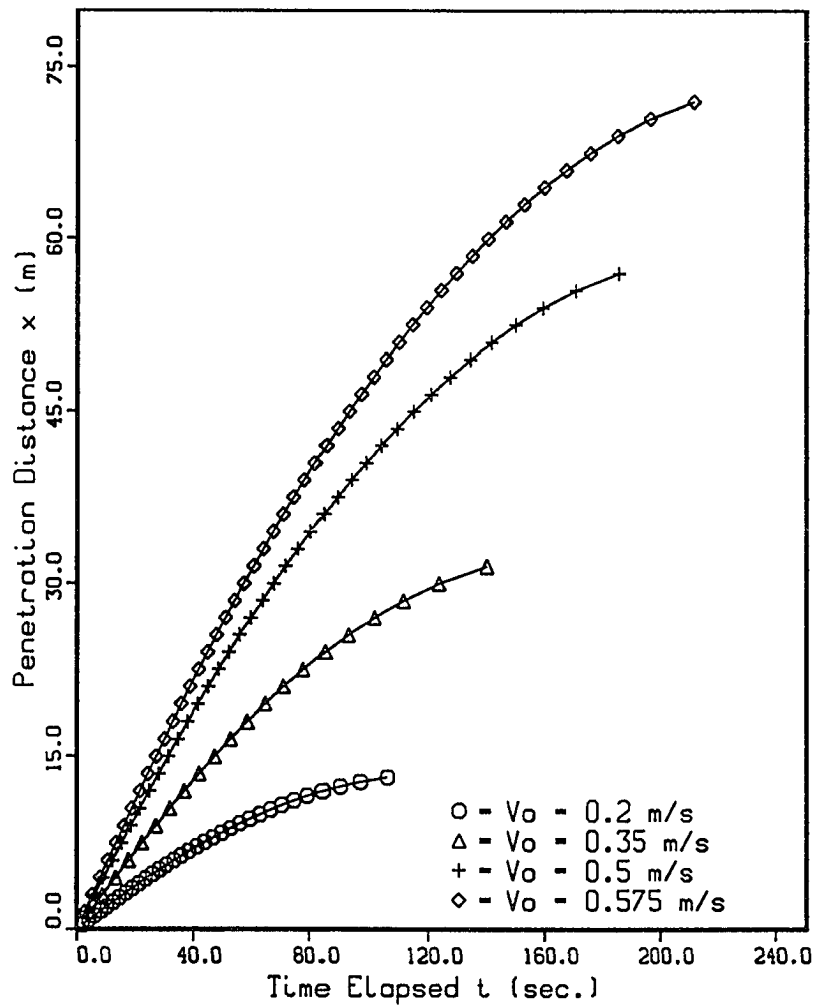


Fig. 5.2. The penetration distance x as a function of time elapsed t for four different initial speed V_0 of the ice island, in which the mass was from the ice island alone, and the added mass was not taken into account.

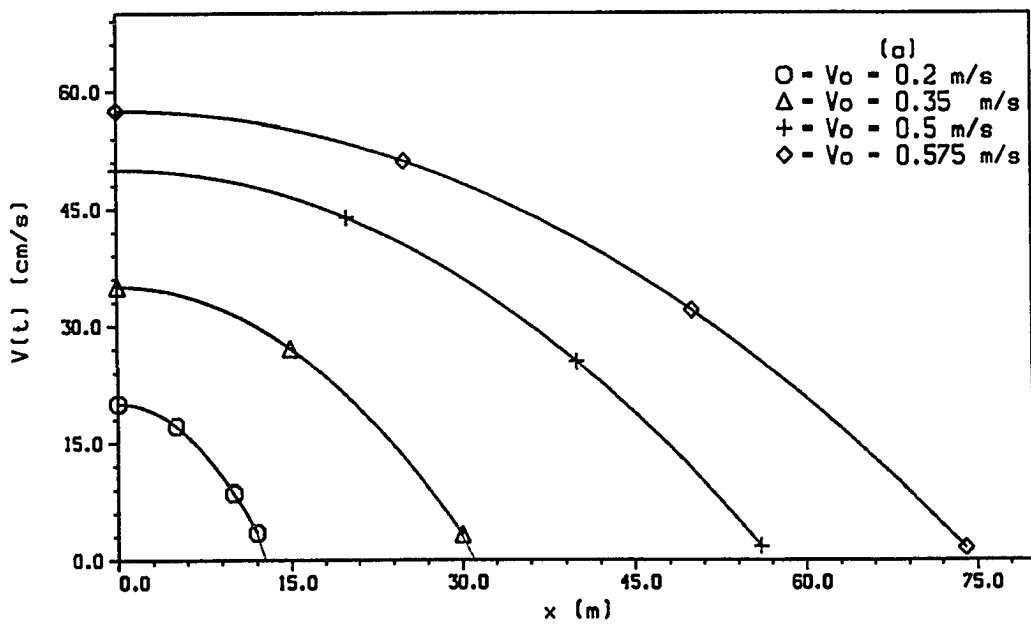
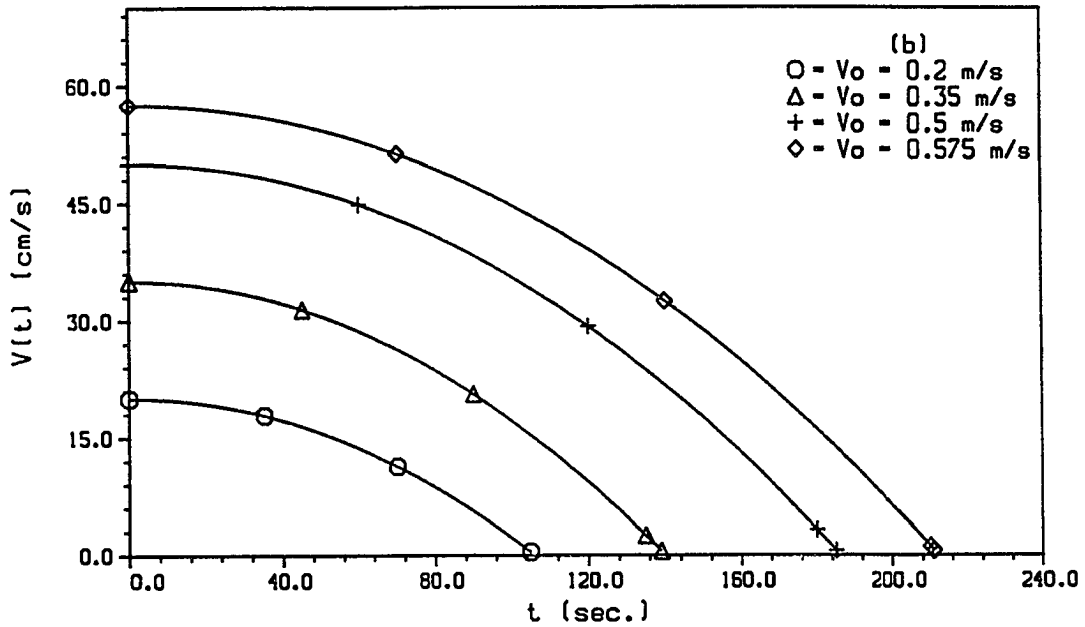


Fig. 5.3. The speed of the ice island $V(t)$ as a function of the penetration distance x , and as a function of the time elapsed t .

mass have been treated and discussed, such as the complex potential representation (Yu and Visell, 1961), the finite element method (Bai, 1977) and the numerical scheme (Garrison, 1975). However, most existing techniques require complicated numerical procedures.

A simplified method was presented by Marcellus and Morrison (1982), in which the added mass can be expressed simply as an additional mass which is added to the body's inertial mass. So, for a large, flat, smooth ice island of submerged thickness h_s in water depth H_s (Figure 5.4) the total effective mass of the ice island may be written as (Marcellus and Morrison, 1982)

$$M_e = \left(1 + \frac{h_s}{2H_s - h_s}\right)M, \quad (5-8)$$

where M is the mass of the ice island alone, and M_e is the total effective mass of the ice island. If the sea water density is taken as 1028 kgm^{-3} (Sanderson, 1988), then $h_s = 16.93 \text{ m}$ and $H_s = 32.93 \text{ m}$, and therefore $M_e = 1.76 \times 10^{11} \text{ kg}$, a change of 26% larger than the mass of the ice island alone.

Another simplified approach to determine the added mass was also presented (Luk, 1983), which was based on long water wave theory. He assumed that the water is incompressible, inviscid, and the water flow is irrotational. If the angular frequency of the ice floe motion is very little and taken to be zero, the water added mass can be simply given by

$$M_a = \rho V \left(\frac{h_s}{2H_s - h_s}\right), \quad (5-9)$$

then, the total effective mass of the ice island may be given by $M_e = M + M_a$, where ρ is the sea water density, V is the submerged volume of the ice island, and H_s and h_s are the same definitions in Figure 5.4. This equation (5-9) presents a

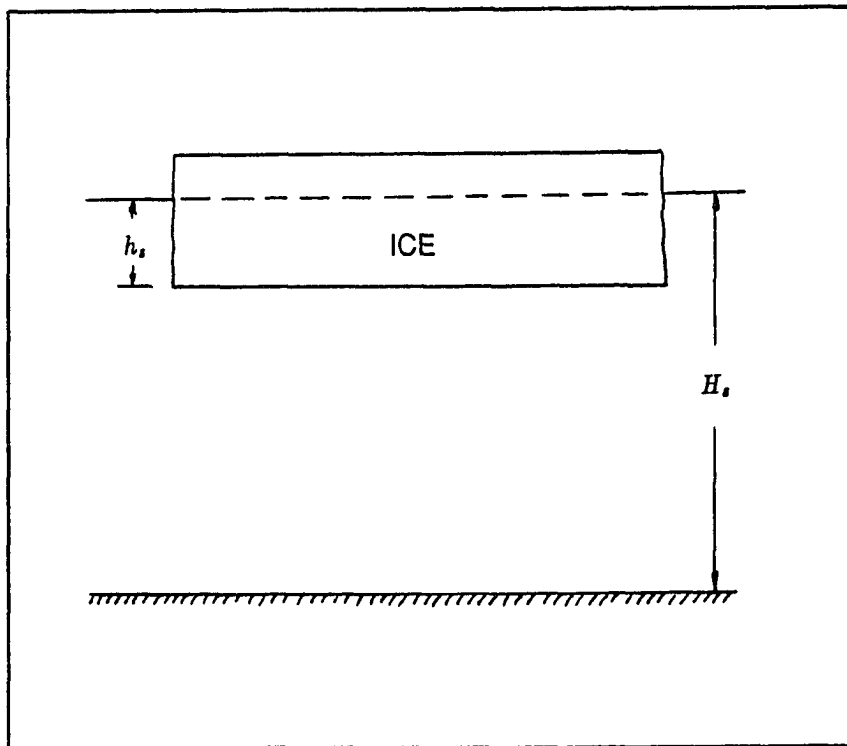


Fig. 5.4. Geometry for added mass calculation (Marcellus and Morrison, 1982).

result equal to equation (5-8). Therefore, the added mass considered in this study was based on equation (5-8) or (5-9).

Substituting the total effective mass M_e into equation (5-7) instead of M , ($M_e=1.76 \times 10^{11}$ kg), results of the penetration distance x as a function of elapsed time t are presented in Figure 5.5, in which four different values of V_0 were also considered. The penetration distance x was similar to that in Figure 5.2, and increased with elapsed time t , but the maximum penetration distance X_{max} was larger. For example, for $V_0=0.2$ m/s, X_{max} reached 16.5 m, rather than 13.2 m as in the earlier case without hydrodynamic added mass.

The ice island force was calculated from each maximum penetration distance by the use of equation (5-4), and was plotted as a function of penetration distance x in Figure 5.6 for M , and Figure 5.7 for M_e . It can be seen from comparison of Figures 5.6 and 5.7 that the maximum force acting on the structure depends on the penetration distance x , and the initial speed V_0 as well. For example, for $V_0=0.2$ m/s, the maximum force was 253 MN (Figure 5.6 (a)), but for $V_0=0.575$ m/s, the maximum force reached 336 MN (Figure 5.6 (d)). As a comparison with added hydrodynamic mass taken into account (Figure 5.7), the maximum force for the same speed of V_0 was larger. For $V_0=0.2$ m/s, the maximum force was 266 MN (Figure 5.7 (a)), about 1.05 times larger.

The forces acting on the structure as a function of elapsed time t were also plotted from the results discussed above. In Figure 5.8, the forces as a function of elapsed time t for the added mass not taken into account is shown, and in Figure 5.9, the added mass was taken into account. The complete comparison is made in Table 5.1 for the maximum force F_{max} acting upon the structure, and the maximum value of the penetration distance X_{max} , for both cases of the mass= M and mass= M_e . The effects of the initial speed V_0 of the ice island as it affects total elapsed time t are also included. For example, the maximum penetration distance

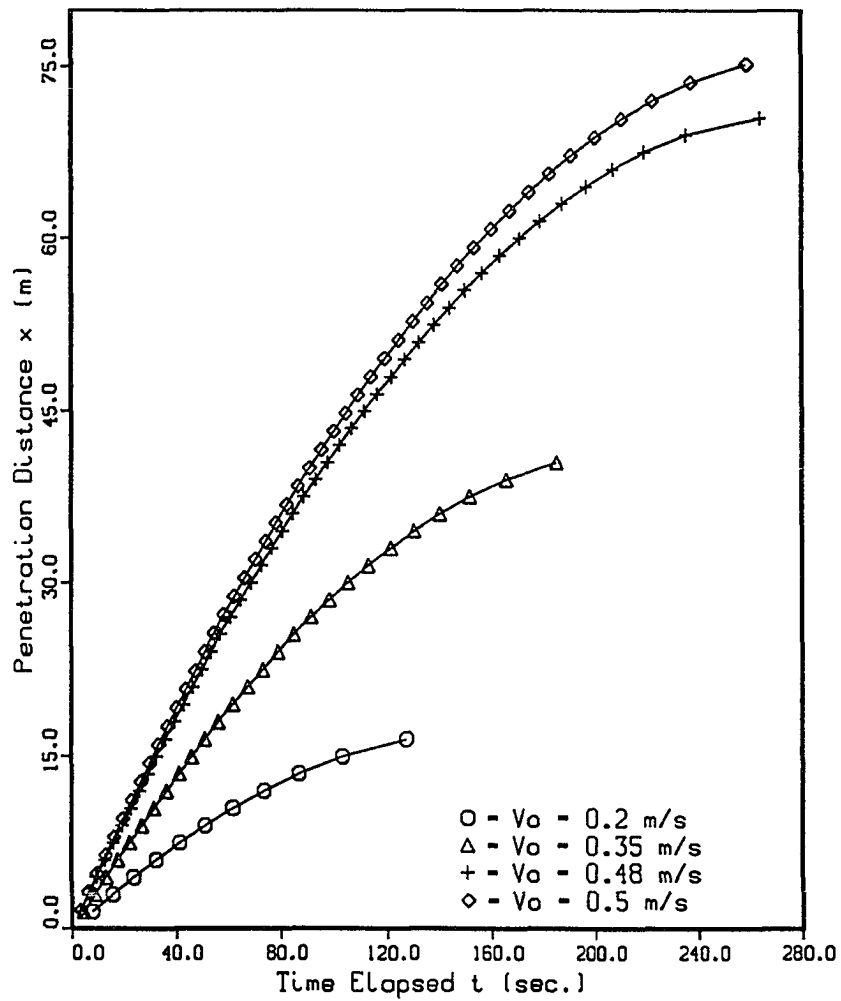


Fig. 5.5. The penetration distance x as a function of time elapsed t for four different initial speed V_0 of the ice island, in which the added mass was taken into account.

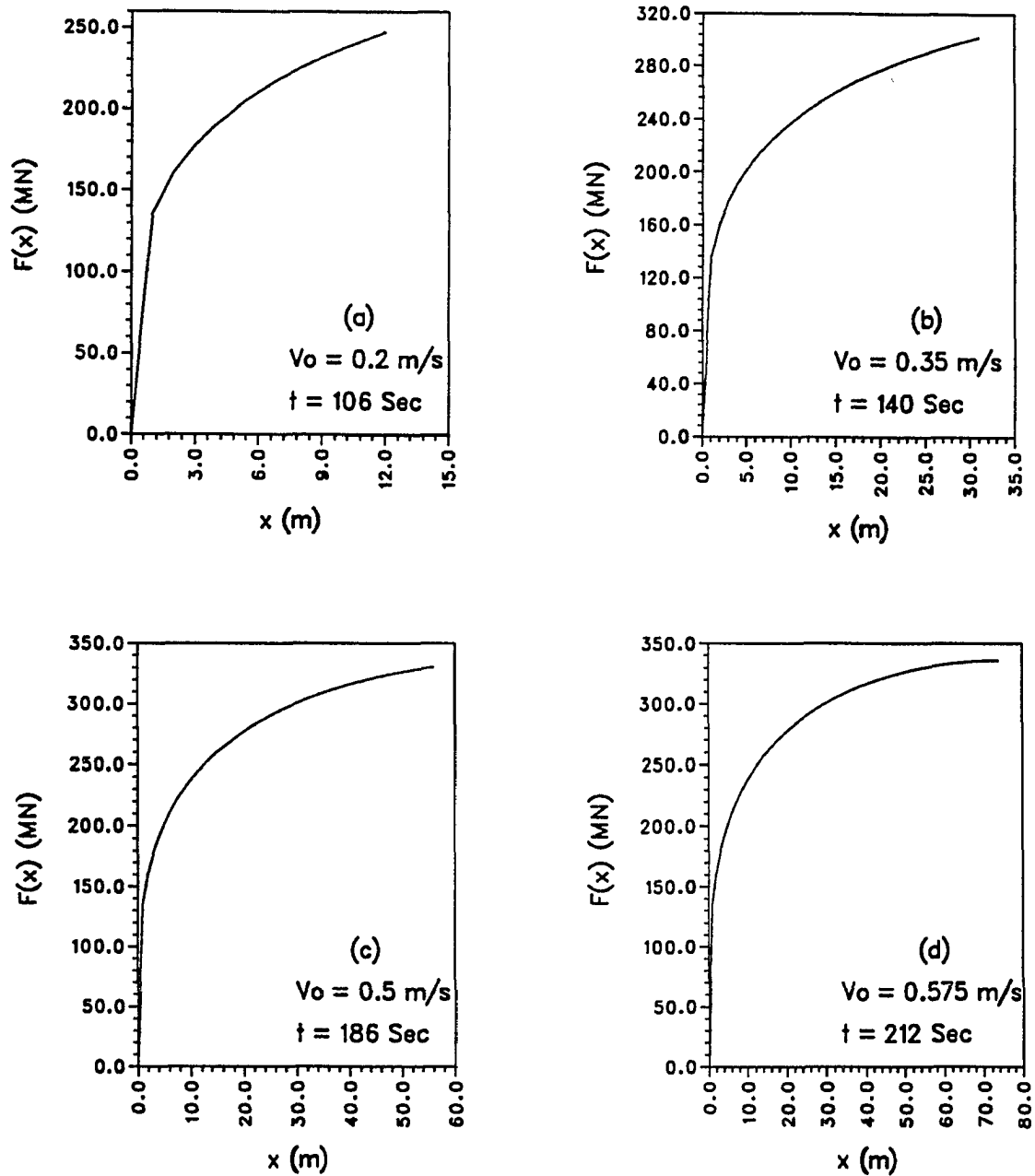


Fig. 5.6. The ice island forces as a function of penetration distance x , in which the added mass was not taken into account.

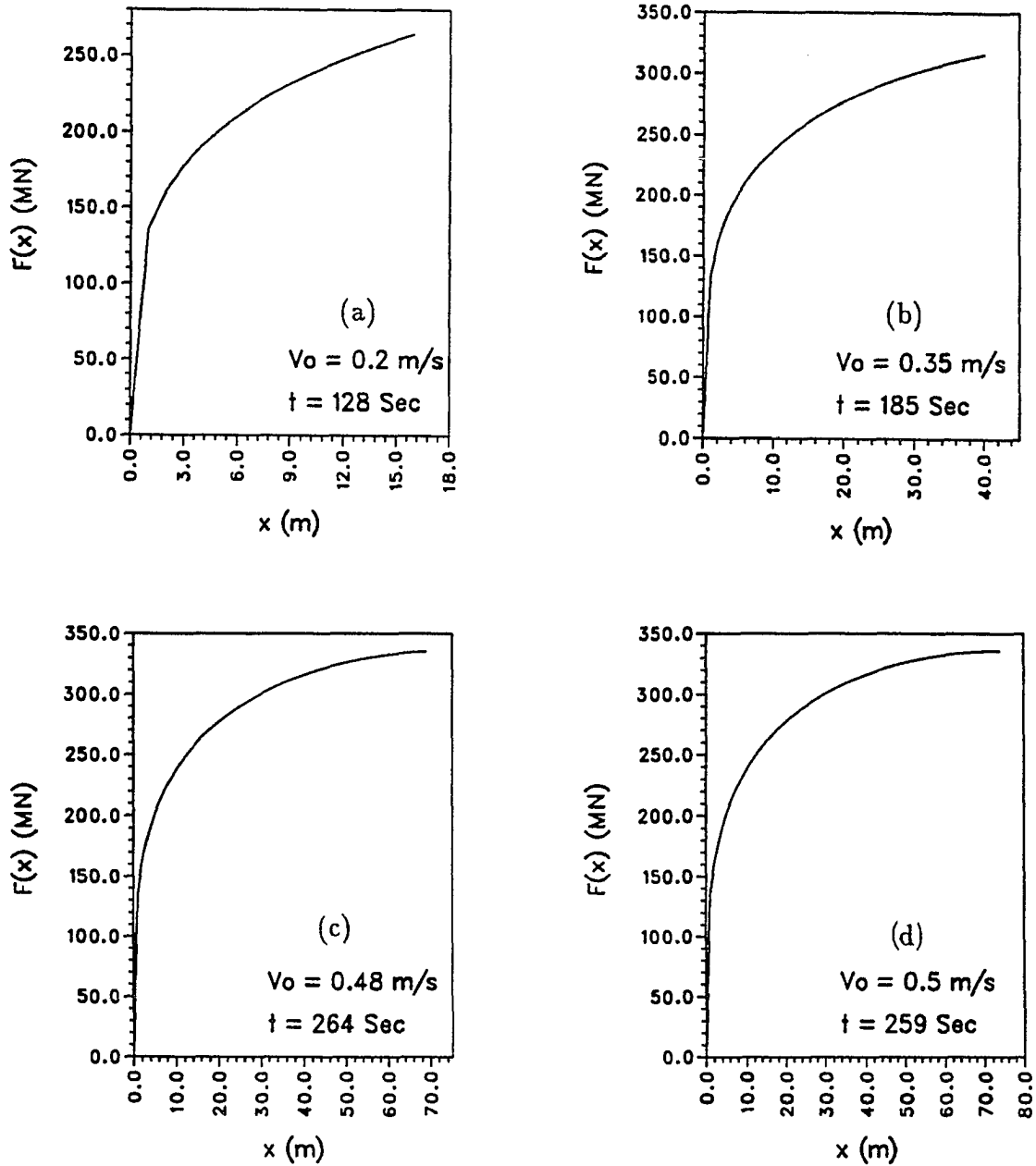


Fig. 5.7. The ice island forces as a function of penetration distance x , in which the added mass was taken into account.

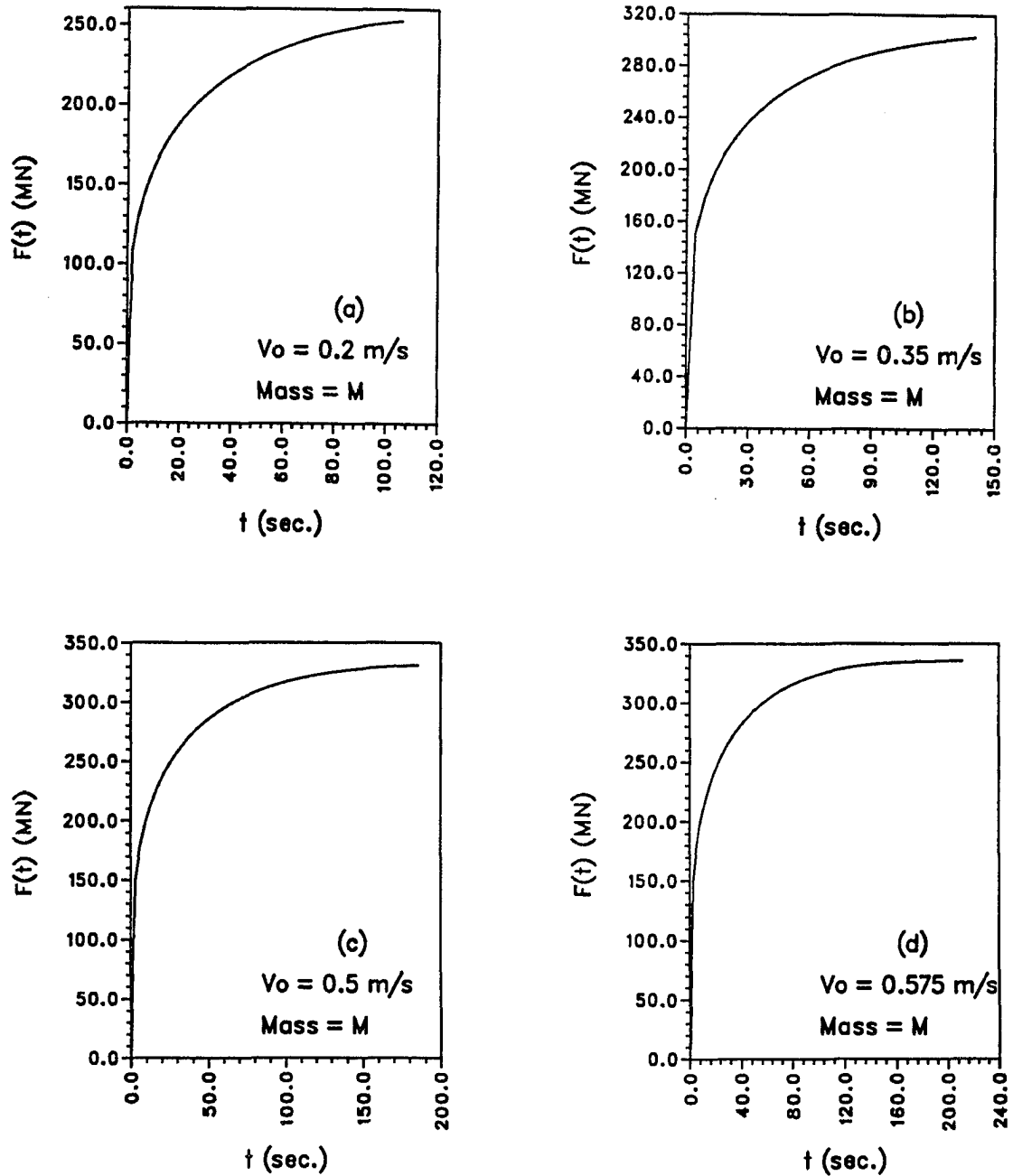


Fig. 5.8. The ice island forces as a function of time elapsed t , in which the added mass was not taken into account.

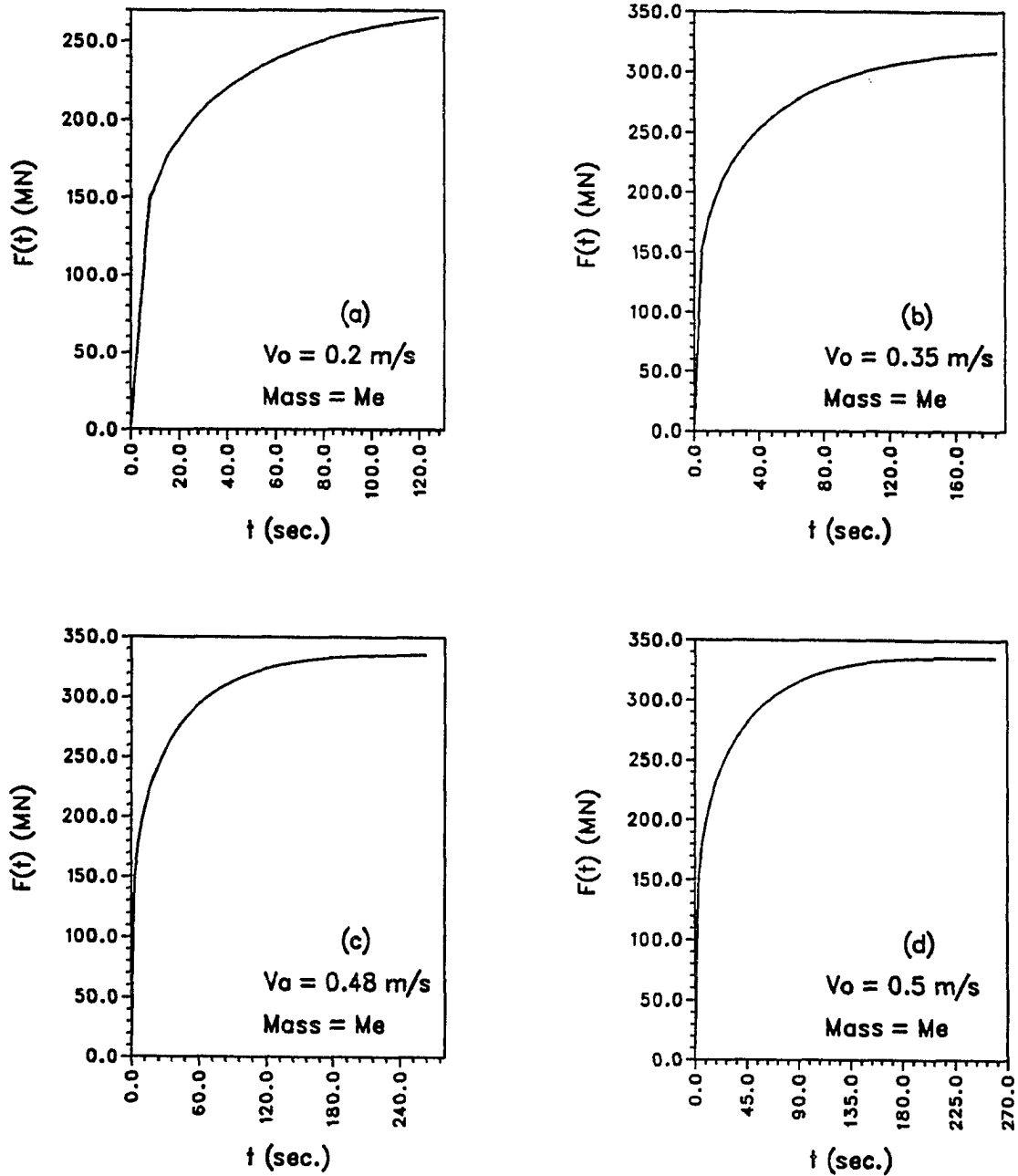


Fig. 5.9. The ice island forces as a function of time elapsed t , in which the added mass was taken into account.

TABLE 5.1. Results for the maximum force, the maximum penetration distance and maximum time elapsed for the ice island model of 3 km × 2.5 km × 20 m.

The complete comparison for the maximum force F_{max} and the maximum penetration distance X_{max} for both cases of the mass=M and mass= M_e , and as affected by the initial speed V_0 of the ice island, including the longest elapsed time t_{max} .

mass=M=1.305 × 10 ¹¹ kg			
V_0 (m/s)	X_{max} (m)	t_{max} (sec.)	F_{max} (MN)
0.20	13.2	106	253
0.35	31.5	140	303
0.50	57.0	186	331
0.575	75.0	212	336
mass= M_e =1.76 × 10 ¹¹ kg			
V_0 (m/s)	X_{max} (m)	t_{max} (sec.)	F_{max} (MN)
0.20	16.5	128	266
0.35	40.5	185	317
0.48	70.0	264	335
0.50	75.0	259	336

X_{max} with $V_0=0.2$ m/s was 13.2 m, the longest time elapsed was $t_{max}=106$ sec. and the maximum force acting on the structure $F_{max}=253$ MN for the case of mass=M; however, $X_{max}=16.5$ m, $t_{max}=128$ sec. and $F_{max}=266$ MN for the same $V_0=0.2$ m/s and the case of mass= M_e .

To check the size effects of the ice island, a smaller ice island of 2500m × 2000m × 15m, was also considered. The results for the maximum force F_{max} and the maximum penetration distance X_{max} are shown in Table 5.2. Comparing with both Tables 5.1 and 5.2, the smaller sized ice island showed smaller penetration distance, smaller force acting on the structure, and shorter elapsed time, with the same initial speed of the ice island. The ratio between the two ice island model

TABLE 5.2. Results for the maximum force, the maximum penetration distance and maximum elapsed time for the ice island model of 2.5 km × 2.0 km × 15 m.

The complete comparison for the maximum force F_{max} and the maximum penetration distance X_{max} for both cases of the mass= M and mass= M_e , and as affected by the initial speed V_0 of the ice island, including the longest elapsed time t_{max} .

mass= $M=6.525 \times 10^{10}$ kg			
V_0 (m/s)	X_{max} (m)	t_{max} (sec.)	F_{max} (MN)
0.20	8.0	59	225
0.35	20.8	96	279
0.50	36.8	125	312
0.575	46.4	145	323
mass= $M_e=8.378 \times 10^{10}$ kg			
V_0 (m/s)	X_{max} (m)	t_{max} (sec.)	F_{max} (MN)
0.20	8	55	225
0.35	22.4	108	284
0.48	36.8	130	312
0.50	38.4	121	314

volumes is 2. From both Tables 5.1 and 5.2, the ratios between the maximum penetration distances are 1.65, 1.51, 1.55 and 1.62, corresponding to the same initial speed of 0.2 m/s, 0.35 m/s, 0.5 m/s and 0.575 m/s, respectively; The ratios between the maximum forces are 1.12, 1.09, 1.06 and 1.04, corresponding to the same initial speed of 0.2 m/s, 0.35 m/s, 0.5 m/s and 0.575 m/s.

It therefore appears from this theoretical model that the maximum forces on the structure are mainly dependent upon the initial velocity of the ice island, and are only weakly dependent upon the mass (i.e. the size) of the ice island. These conclusions may be directly related to initial assumptions in the model, however, and an alternative model is presented in the next section.

5.3 Results for the Ice Island Loads by The Three-Dimensional Finite Element Method

The ice island forces acting on a cylindrical rigid structure were also analyzed and calculated by the three dimensional finite element method using the ice island model as shown in Chapter 2, in which the generation of ice powder fragments was considered within the zone where the ice island impacted the structure. The ice powder was located and treated in the area where the ice failed. From the results of the calculations, the area of ice powder formed was initially at the ice island/structure contact zone. This zone progressively grows in area and in extent. Stresses were transmitted through the ice powder to the structure until the composite ice island comes to rest. The method used to consider the ice powder in the calculations was by changing the material properties from normal ice to another material, ice powder, of weaker strength, for the continuum of small fragments in the zone where the ice failed.

Little information is available in the literature on ice powder properties. However, some studies related to ice rubble or broken ice pieces, and ridge pressure on structures have been presented (Keinonen and Nyman, 1978; Prodanovic, 1979; 1981), which were based upon model tests, field measurements and calculations. These results provided useful data in this preliminary study on ice powder formation during ice island crushing against the structure.

Ice rubble or broken ice is a contiguous, random collection of ice pieces; on a sufficiently large scale, ice rubble can be considered homogeneous and isotropic (Prodanovic, 1979). Sea ice rubble contains fragments of broken ice sheets that originally had a columnar-grained structure. Submerged rubble contains newly formed ice between broken ice pieces in a water-slush matrix. Drained rubble has locally-sintered ice pieces in an air-snow matrix. At very high confining pressures,

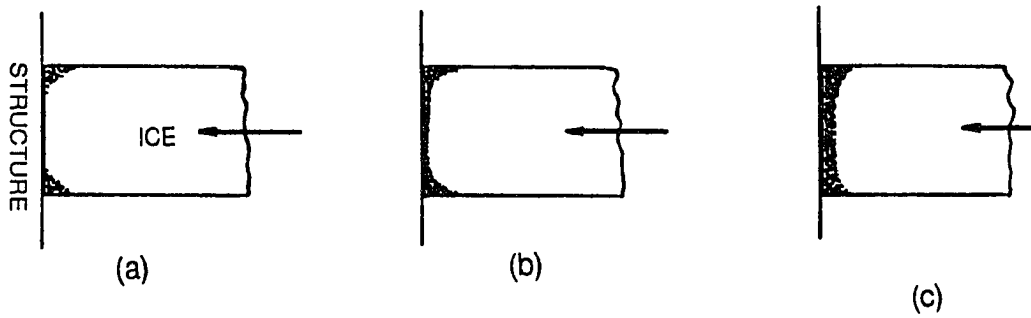
ice rubble could show volume decrease during the loading process and the yield surface could be limited (Prodanovic, 1979).

When an ice sheet was acting against a structure, the top surface of the broken ice pieces in the ice/structure contact zone would be easily moving out, and the strength of such a material should be reduced to a very low value. At the bottom surface of the ice sheet, broken ice pieces in the ice/structure contact zone would be submerged by sea water, and the strength of the fragmented material should also be reduced to very low values. However, for an ice island with a larger thickness against a structure, because of the confinement in the middle area of the ice island thickness, the strength of the broken ice pieces in that area should be larger than the strength both at the top surface and at the bottom surface in the ice/structure contact zone.

Interaction between a fixed cylindrical structure and an ice island is extremely complicated. But, the calculation in finite element analysis is simplified by assuming that an ice powder (broken ice pieces in the ice/structure contact zone) is homogeneous, isotropic, and uniform in thickness. The time function is divided by many steps. In each step the strength of the broken ice pieces (ice powder) that is newly formed would be reduced. The strength of the ice powder within 3 meters of the top surface was chosen to be 5% of the strength of unbroken ice. In the bottom surface region, 3 meters thick, the strength of the ice powder was chosen as 8% of the strength of unbroken ice. In the middle area, about 14 meters in thickness, a strength of 15% of that of the unbroken ice was chosen. These are based on the analysis as discussed above and the approximation consideration on the distribution of the pressure from the top to the bottom of the thickness, and the pressure reduction from the buoyancy at the bottom of the ice island.

In Figure 5.10, the results of calculations and processes of the formation of the ice powder are shown. Results from one typical run, from the beginning to the

Lateral view:



Top view:

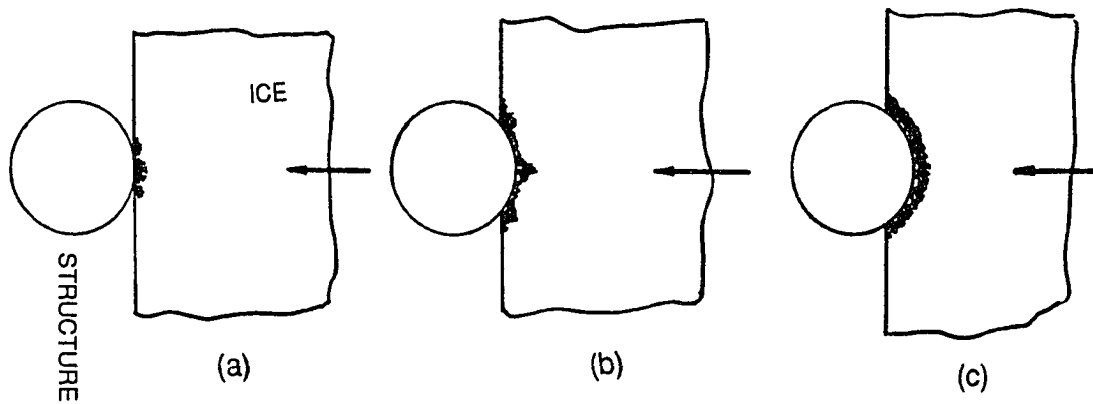


Fig. 5.10. The processes of the formation of the ice powder in the ice island structure contact zone, where the ice failure formed when the ice island impacted the structure.

end of the run are given. It is interesting to note that the ice powder was initially formed at the ice island/structure contact zone in the top and bottom area as shown in Figure 5.10 (a) from the lateral view; and in the center and lateral area as shown in Figure 5.10 (a) from the top view. The ice powder grows from Figure 5.10 (a), when the ice island just contacts the structure, to Figure 10 (b), when the ice island has impacted the structure for some time. Finally, all of the area of the ice island/structure contact zone became ice powder (Figure 5.10 (c)), which was squeezed, and the ice island was penetrating onto the structure until it came to rest.

The method used for the driving force in this finite element analysis was from a constant applied pack ice stress, which is different from the theoretical analysis (the initial speed of the ice island was the driving force in the theoretical analysis). This applied stress caused the ice failure at the ice/structure contact zone. From the processes of the ice island penetrating onto the structure, results of the analysis of ice island forces are given, and shown in Figure 5.11. For this first computation, the maximum force as a function of the maximum penetration distance is presented, and the final time was five seconds (time step = 0.5 sec.). The ice island was still moving after 5 seconds. When the maximum force acting on the structure was 6600 MN, the maximum penetration distance was only 6.8 m within 5 seconds, as shown in Figure 5.11. To examine the effects of a longer time, another computation was done, the final time being increased to 100 seconds (time step = 0.5 sec.) with results as shown in Figure 5.12. For this second computation, the penetration distance after 100 seconds was somewhat larger. With the final time increased to 100 seconds, the maximum penetration distance was 8.2 m (Figure 5.12), only 1.2 times larger than the value from the first run (5 sec.).

The penetration distance as a function of elapsed time is shown in Figure 5.13, in which the final time was treated as 5 seconds; and in Figure 5.14, the final time

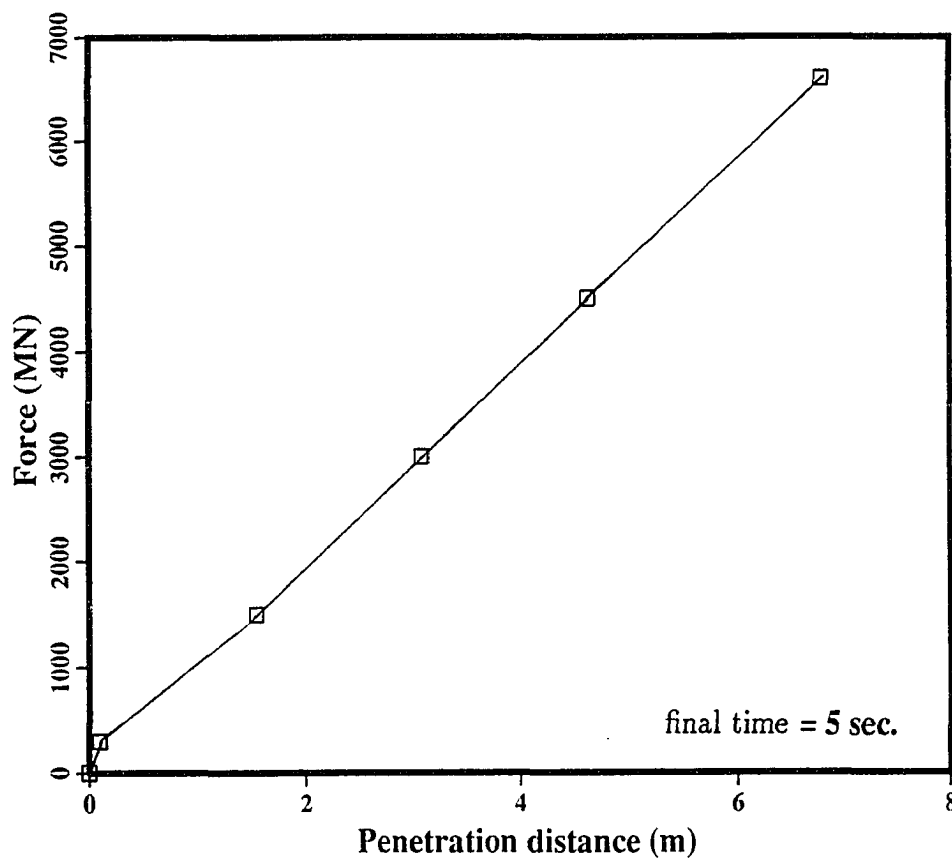


Fig. 5.11. The maximum ice island forces acting on the structure as a function of the maximum penetration distance, in which the final time was 5 seconds.

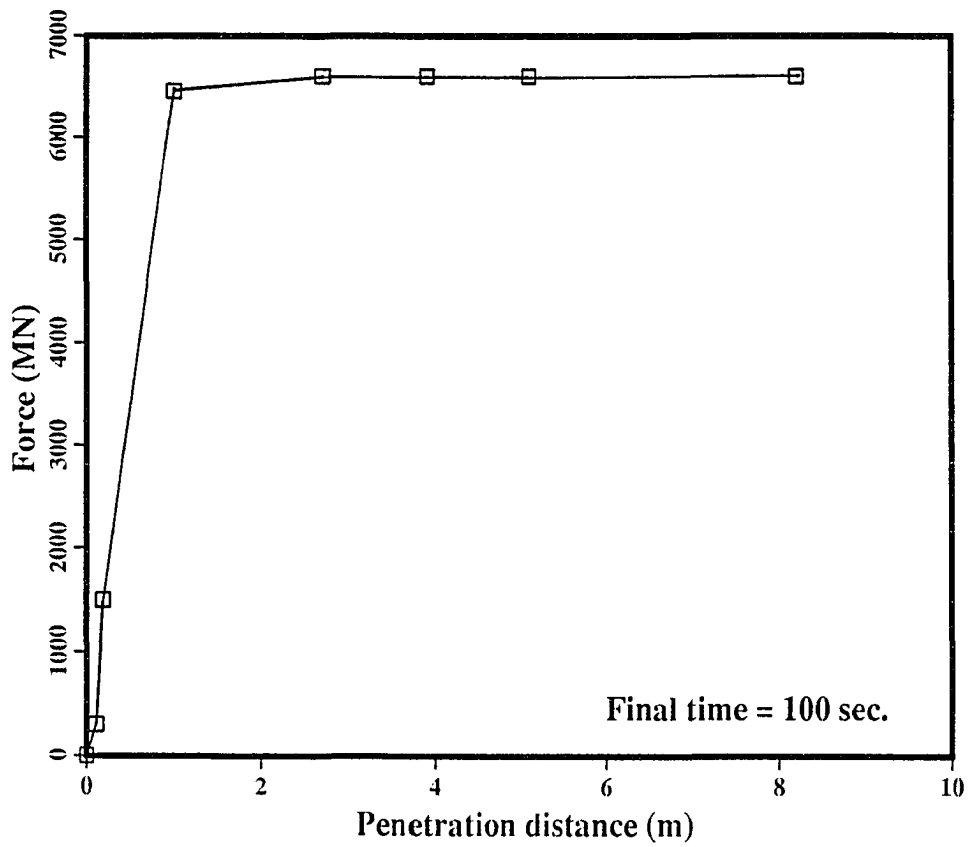


Fig. 5.12. The maximum ice island forces acting on the structure as a function of the maximum penetration distance, in which the final time was 100 seconds.

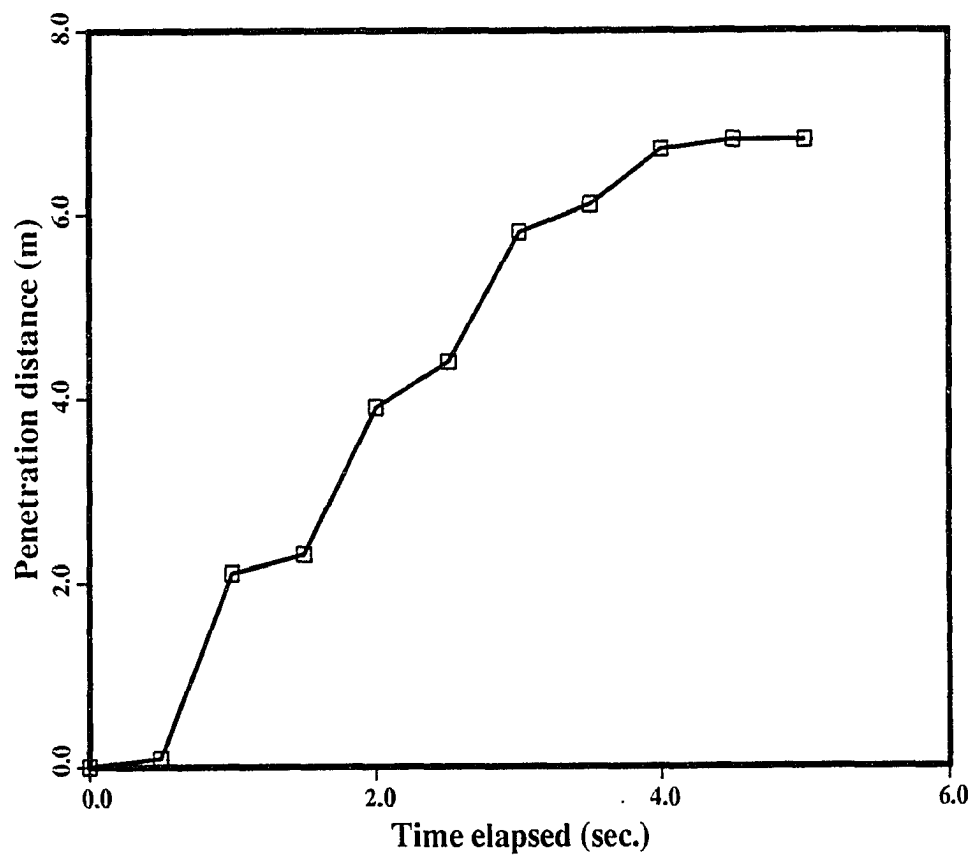


Fig. 5.13. The penetration distance as a function of time elapsed, in which the final time was 5 seconds.

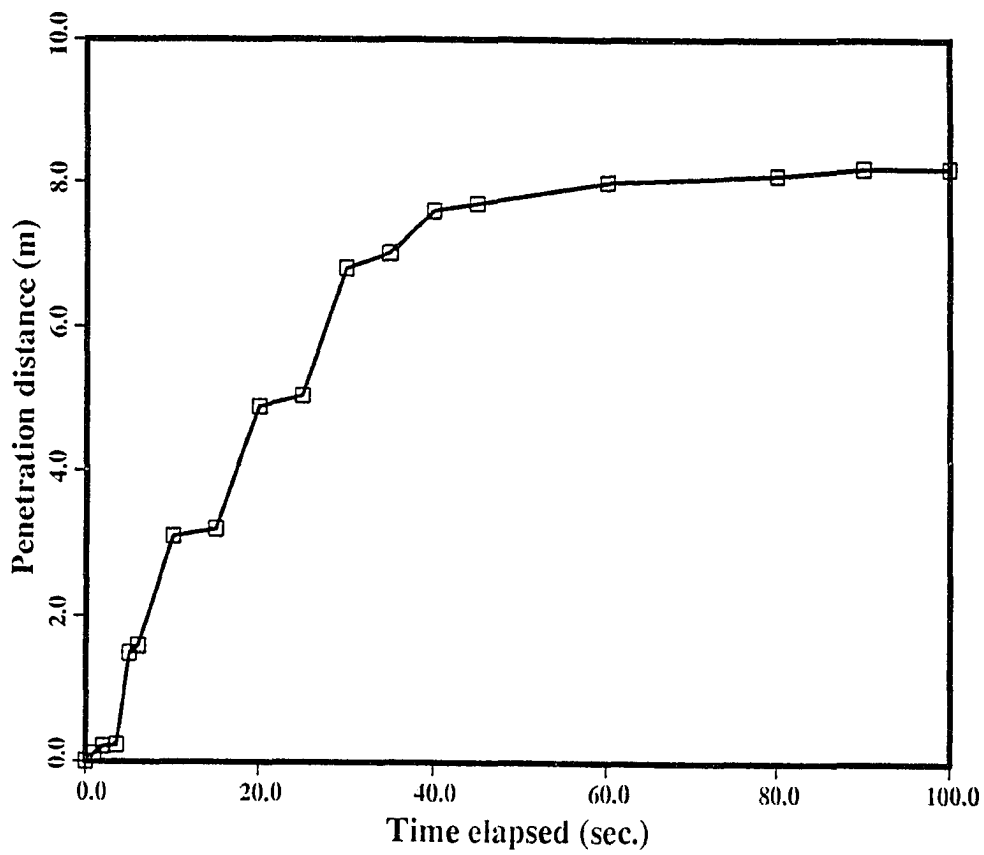


Fig. 5.14. The penetration distance as a function of time elapsed, in which the final time was 100 seconds.

was treated as 100 seconds. The irregularity in the curves of penetration distance versus time is caused by the choice of the length of the time step increment. When the ice failed, it was then treated as another material (ice powder) for the next time step, so that the larger penetration distance resulted on the next step.

The forces acting on the structure as a function of time elapsed are shown in Figure 5.15. The maximum force of 6600 MN was reached very quickly. It can be seen from Figure 5.15 that in the very beginning, when the ice island impacted the structure, the force changed from zero to 6500 MN after 4 seconds. The forces were then gradually increasing with time. The behavior from $t = 5$ seconds to $t = 100$ seconds is shown in Figure 5.15, in which it changed slowly with time and was maintained at 6600 MN.

The results by this three dimensional finite element method showed that it was very difficult to make the ice penetrate into the structure for a longer distance. The maximum penetration distance was only 6.8 m within 5 seconds, and was only 8.2 m when the final time increased to 100 seconds, for a maximum force of 6600 MN. The ice island velocity was 0.01 cm/sec at the 100-second time point.

The theoretical and three dimensional finite element results were analyzed and discussed for the ice island interaction with a structure in this chapter. In the theoretical analysis, the maximum force occurred and was obtained just before the ice island stopped, which was based on the initial kinetic energy and the rate at which this energy was dissipated during the impact process. The results showed that the added hydrodynamic mass affects the forces acting on the structure, but this was insignificant as compared with the effects of the initial speed of the ice island. In all cases, the initial speed of the ice island was the dominant factor in analysis of the penetration distance, and thus the maximum force acting on the structure. The maximum force acting on the structure for an ice island of

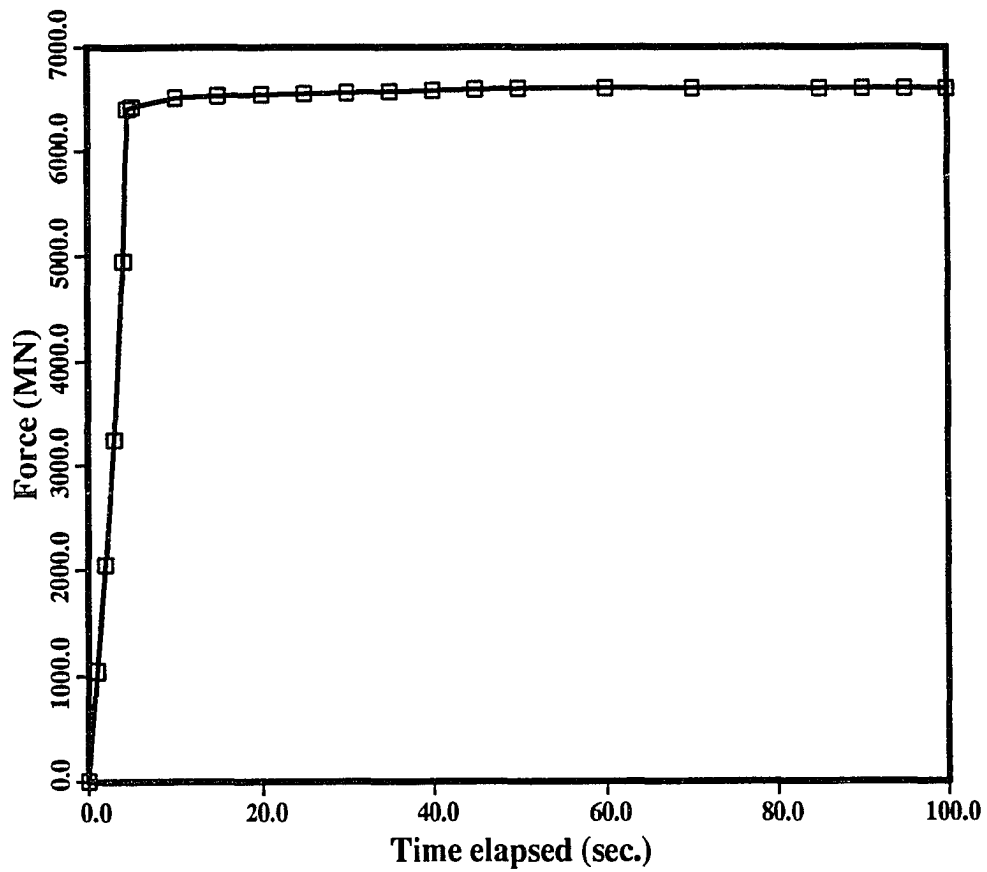


Fig. 5.15. The maximum force of 6600 MN reached by one typical run of the program for the final time of 100 seconds, as a function of time elapsed.

$3\text{ km} \times 2.5\text{ km} \times 20\text{ m}$ was 336 MN, and for an ice island of $2.5\text{ km} \times 2\text{ km} \times 15\text{ m}$ the maximum force was 323 MN.

In the finite element analysis, the total forces showed a larger value and the penetration distance showed a smaller value. The total forces acting on the structure were obtained by the applied stress which caused the ice to fail in the ice island/contact zone, in which ice powder was treated and penetration distance was increased.

The finite-element method has become a very effective stress analysis tool in the fields of structural and solid mechanics, and has proven to be a very effective discretization procedure (Bathe and Larsson, 1985). Most of the ice data parameters used in the theoretical method are from full-scale sea ice measurements, but were, as a approximation, substituted into the ice island force calculations. Because of the uncertainties in such field data, and the differences between sea ice and ice island ice, the result of the finite-element method is thought to be closer to reality.

CHAPTER 6

Conclusions

Two models of ice floes and ice islands were used in the analysis and calculations to find stresses and ice forces acting upon structures, using the three-dimensional finite-element method. Also, a theoretical analysis of ice island loads acting upon a cylindrical structure was made.

In the ice floe model, the interaction between a multiyear sea ice floe of variable thickness, and a rigid, vertical-wall offshore structure was treated. The nonuniform thickness of a sea ice floe does strongly affect the total force transmitted by ice against an offshore structure. Bending will be accentuated on the top surface of the thinnest area of the ice floe, and cause a tensile failure of ice in that area. The forces that can be transmitted to the structure from an ice floe of nonuniform thickness are much smaller than those from a uniform-thickness ice floe. As an example of a variable-thickness ice floe of $\Delta t/t = 0.5$ ($\Delta t/t$ is the ratio of the thinnest thickness in the floe to the floe thickness at the structure), a reduction factor of 13.9 in the maximum total force on the structure, as compared with a uniform-thickness ice floe, is attributed to the presence of the thin central region of the ice floe. Largest ice floe displacements occurred at the ice floe/pack ice boundary, and are primarily in the x and z directions for a variable-thickness ice floe, but are in the x-direction for a uniform-thickness ice floe. A compressive stress failure takes place, for uniform thickness ice, at the structure/ice contact area. For variable-thickness ice floes, however, tensile failure occurs at the top surface, in the thinnest place of the floe.

Examination of an ice/structure contact zone located in the eccentric region of the floe edge was made. In that case, the ice first tensile failure occurs only at one side of the top surface in the thinnest area of the floe. The total force acting on

the structure is smaller than for the case of the ice/structure contact zone located in the centric region.

A sliding boundary condition at the ice/structure interface causes a larger force to act upon the structure. The ice first tensile failure is at the same location as for the case of a fixed boundary condition. There is only a slight change of the localized maximum pressure, at the bottom of the floe at the structure/ice contact zone. Therefore, friction coefficient at the structure has little effect upon the force on the structure.

From simulations of two-dimensional ice thickness variation, the ice first tensile failure occurs at the top surface in the thinnest side of the floe. A compressive stress occurs on the top surface of the thicker part of the ice floe as well. Because of this two-dimensional ice thickness variation, the total force acting on the structure is reduced, and is smaller than that for a uniform thickness ice floe. However, the total force is larger than that for a one-dimensional ice thickness variation in the floe. Thus, the two-dimensional variations in ice floe thickness, as found in nature, will lead to reductions in force on the structure which, while significant, are less than that predicted by one-dimensional theory.

The sensitivity of the results to the assumed loading condition was examined by reducing the area over which the pack ice stress was applied. For the variable thickness floes of $\Delta t/t=0.4$, $\Delta t/t=0.5$ and $\Delta t/t = 0.65$ ($\Delta t/t$ is the ratio of the thinnest thickness in the floe to the thickness at the structure), the ice first failure is at the bottom of the floe in the thinnest area. The total force acting on the structure is from 2.53 to 12.1 times larger than for the same cases with the pack ice stress distributed over the full thickness of the ice floe. No tensile failure occurred in this case. Therefore, the mode of failure of the ice floe, and the ice forces on the structure, are not only sensitive to ice floe thickness but also are sensitive to the geometry of the boundary contact between the ice floe and the adjacent pack ice.

Examination of the assumption of elastic modulus was done by changing elastic modulus from 4 GPa to 8 GPa. This causes the value of normalized stress in the floe, S_r , to change from 1.5% to 2.2%. As elastic modulus is allowed to vary as a function of depth in the floe, two results are obtained. With the elastic modulus of 6 GPa at the top surface and 3 GPa at the bottom of the ice, for the condition of a uniform-thickness ice floe, ice first failure occurs only at the top region at the ice/structure contact zone. An average pack ice compressive stress of $P = 3.9$ MPa causes this failure. This is 22% of the value obtained when $E=6$ GPa is a constant from the top to the bottom of the ice floe. In another case of a variable thickness floe of $\Delta t/t = 0.5$, ice first tensile failure still occurs at the top surface of the thinnest area of the ice floe, but the average pack ice compressive stress is only $P = 0.25$ MPa. This is a 30% change as compared with a case of constant elastic modulus $E=6$ GPa from the top to the bottom of the ice floe. Therefore, the low elastic modulus present in the warm lower part of the ice sheet causes tensile failure and is contributing significantly to the reduction of ice force on the structure.

Many stress analyses for uniform thickness and variable thickness ice floes against a rigid, vertical-wall structure, were done as mentioned above. Analysis and calculation on the ice forces acting on a compliant structure and foundation were also completed using the three-dimensional finite element method. The maximum force acting on the compliant structure is 118 MN for a variable-thickness ice floe of $\Delta t/t=0.5$, corresponding to the maximum displacement of the structure of 0.033 m at the ice floe/structure contact zone. The maximum force acting on the structure is 1620 MN for a uniform-thickness ice floe, corresponding to the maximum displacement of the structure of 0.112 m. The results for ice forces on a compliant structure are very close to those obtained for a rigid structure. This may not be true for more flexible structures, however, that are excited into vibration.

Analysis of ice island forces on a cylindrical structure was another main topic in this study, in which both a theoretical method and a three-dimensional finite-element method were used in the calculations. In the theoretical analysis, the progressive penetration and growing area of contact during the ice island impacting process was considered. Results show a maximum force on a cylindrical structure of 336 MN, corresponding to a maximum penetration distance of 75 m, which is the radius of the cylindrical structure. The results obtained using the three-dimensional finite-element method show a maximum force on the structure which is much larger. The maximum penetration distance is very small (8.2 m) and the peak force is 6600 MN. The finite-element method has proven to be a very effective discretization procedure (Bathe and Larsson, 1985). Most of the ice data parameters used in the theoretical method are from full-scale sea ice measurements, but were, as a approximation, substituted into the ice island force calculations. Because of the uncertainties in such field data, and the differences between sea ice and ice island ice, the result of the finite-element method is thought to be closer to reality.

The calculations, while oriented towards a multiyear floe interacting with a structure, also illustrate the principles of annual ice floe failure against structures, grounded ice rubble piles, gravel islands, and against massive, slowly-moving ice features such as consolidated ridges and ice islands.

Future research may involve models which simulate reality even more closely. It would be well to include the effects of the cracks pre-existing in the floe, temperature influence upon floe properties, and other more random geometries of ice floes and structure interaction areas.

References

- Ashby, M. F. and P. Duval, 1985, The Creep of Polycrystalline Ice, *Cold Regions Science and Technology* 11, pp 285-300.
- Ashby, M. F. and S. D. Hallam, 1986, The Failure of Brittle Solids Containing Small Cracks under Compressive Stress-states, *Acta Metallurgica* 34 (3), pp 497-510.
- Ashton, G., 1986, River and Lake Ice Engineering, *Littleton, Colorado: Water Resources Publications*.
- Bai, K. J., 1977, The Added Mass of Two-dimensional Cylinders Heaving in Water of Finite Depth, *J. Fluid Mechanics*, Vol. 81, pp. 85-101.
- Bathe, K. J. and G. Larsson, 1985, The Use of ADINA in Engineering Practice, in *Handbook Finite Element System*, C. A. Brebbia, ed., Springer-Verlag, 1985.
- Bercha, F.G., T. G. Brown and M. S. Cheung, 1985, Local Pressure in Ice-Structure Interaction, *Civil Engineering in the Arctic Offshore*, Proceedings of the Conference Arctic'85, pp 1243-1251. Pritchard, University of Washington Press.
- Buslov, V. M. and N. W. Krahl, 1983, Fifty-one New Concepts for Arctic Drilling and Production, *Ocean Industry*, August, 1983, pp 46-50.
- Cox, G. F. N., J. A. Richter-Menge, W. F. Weeks, M. Mellor and H. Bosworth, 1984, Mechanical Properties of Multi-year Sea Ice, Phase 1: test results, *CRREL Report*, No. 84-9.
- Cox, G. F. N. and J. A. Richter-Menge, 1985, Tensile Strength of Multi-year Pressure Ridge Sea Ice Samples, *Proc. of 4th International Symposium on Offshore Mechanics and Arctic Engineering*, Vol. 2, pp. 186-193.
- Cox, J. R., 1985, Ice Floe Impact Force on Vertical Sided structures, *Civil Engineering in the Arctic Offshore*, Proceedings of the Conference Arctic'85, pp 211-219.
- Croasdale, K. R., 1980, Ice Forces on Fixed, Rigid Structures, *CRREL Special Report*, No. 80-26, pp. 34-106.

- Duthinh, D.**, 1989, Parametric Study of Iceberg Impact Loads, *Proceedings of Port and Ocean Engineering under Arctic Conditions*, 1989, Vol. 1, pp 492-503.
- Engelbrektsson, A.**, 1989, An Ice-structure Interaction Model Based on Observations in the Gulf of Bothnia, *Proceedings of Port and Ocean Engineering under Arctic Conditions*, 1989, Vol. 1, pp 504-517.
- Frederking, R. M. W.**, 1980, Dynamic Forces on An Inclined Structure, *Proceedings of the IUTAM Symposium on the Physics and Mechanics of Ice*, Copenhagen, Aug. 1979, Berlin: Springer-Verlag, pp 104-116.
- Frederking, R. M. W., G. Timco, M. O. Jeffries and W. M. Sackinger**, 1988, Initial Measurements of Physical and Mechanical Properties of Ice from Hobson's Choice Ice Island, *Proceedings of the International Association for Hydraulic Research (IAHR) Symposium on Ice*, Aug. 23-27, 1988, Sapporo, Japan, Vol. 1, pp 188-198.
- Garrison, C. J.**, 1975, Hydrodynamics of Large Objects in the Sea, Part II - Motions of Free Floating Bodies, *J. Hydronautics*, Vol. 9, pp. 58-63.
- Gerwick, B. C.**, 1986, Construction of Offshore Structures, A Wiley - Interscience Publication.
- Gerwick, B. C. and S. Sakhuja**, 1985, Development of a Methodology for the Design of an Offshore Oil Production Platform on the Alaskan Arctic Continental Shelf, Construction Engineering Division, Dept. of Civil Engineering, University of California, Berkeley.
- Gold, L. W.**, 1977, Engineering Properties of Freshwater Ice, *J. of Glaciology*, 19(81), pp. 197-212.
- Hallam, S. D.**, 1986, The Role of Fracture in Limiting Ice Forces, *Proceedings of int. Assoc. of Hydraulic Research Ice Symposium*, Vol. 2, pp. 287-319.
- Hallam, S. D. and J. P. Nadreau**, 1987, Failure Maps for Ice, *Port and Ocean Engineering under Arctic Conditions*, edited by **W. M. Sackinger and M. O. Jeffries**, The Geophysical Inst., University of Alaska, Vol. III, pp. 45-56.
- Hallam, S. D., N. Jones and M. W. Howard**, 1987, The Effect of Sub-surface Irregularities on the Strength of Multiyear Ice, *Proc. of the 10th*

- International Symposium on Offshore Mechanics and Arctic Engineering*, Houston, Texas, Vol. 4, pp. 235-238.
- Hocking, G., J. R. Williams and G. W. Mustoe**, 1985, Dynamic Global Forces on an Offshore Structure from Multi-year Ice Floe Impacts, *Civil Engineering in the Arctic Offshore*, Proceedings of the Conference Arctic'85, pp 202-210.
- Jeffries, M. O., N. K. Sinha and W. M. Sackinger**, 1990, Failure Stress and Failure Modulus of Natural Ice Island Ice under Uniaxial Compression at Constant Strain Rates, *Proceedings of the 9th International Conference on Offshore Mechanics and Arctic Engineering*, Feb. 18-23, 1990, pp 223-229.
- Jeffries, M. O. and W. M. Sackinger**, 1989, Analysis and Interpretation of an Airborne Synthetic Aperture Radar Image of Hobson's Choice Ice Island, *Proceedings of the 10th International Conference on Port and Ocean Engineering under Arctic Conditions*, June 12-16, 1989, Lulea, Sweden, Vol. 2, pp 1032-1041.
- Jeffries, M. O., W. M. Sackinger and H. Shoemaker**, 1988, Geometry and Physical Properties of Ice Islands, *Port and Ocean Engineering under Arctic Conditions*, edited by **W. M. Sackinger and M. O. Jeffries**, The Geophysical Inst., University of Alaska, Vol. 1, 69-83.
- Jefferies, M. G., H. R. Stewart, R. A. Thomson and B. T. Rogers**, 1985, Molikpaq Development at Tarsiut P-45, *Civil Engineering in the Arctic Offshore*, Proceedings of the Conference Arctic'85, pp 1-27.
- Johnson, R. C. and A. Prodanovic**, 1989, Calculation of Iceberg Impact Forces, *Proceedings of Port and Ocean Engineering under Arctic Conditions*, 1989, Vol. 1, pp 546-556.
- Keinonen, A. and T. Nyman**, 1978, An Experimental Model-Scale Study of the Compressible, Frictional and Cohesive Behaviour of Broken Ice Mass, *Proceedings of IAHR Symposium on Ice Problems*, Lulea, Sweden, Vol. 2, pp. 335-353.
- Kovacs, A.**, 1983, Characteristics of Multi-year Pressure Ridges, *Proceedings of Port and Ocean Engineering under Arctic Conditions*, 1983, Vol. III, pp 173-182.

- Li, F-C, W. M. Sackinger, M. O. Jeffries and Mingchi Lu, 1989, Computer Simulations of the Probability of Ice Island Movements in the Arctic Ocean. *Proceedings of the 10th International Conference on Port and Ocean Engineering under Arctic Conditions*, June 12-16, Lulea, Sweden, Vol. 2, pp. 1063-1072.
- Li, F-C and W. M. Sackinger, 1991, Simulations Study of Ice Island Trajectories in the Arctic Ocean. *Proceedings of the 11th International Conference on Port and Ocean Engineering under Arctic Conditions*, Sept. 24-28, 1991, St. John's, Canada, Vol. 2, pp. 848-858.
- Lu, M., 1988, Analysis of Ice Island Movement, *M.S. Thesis*, University of Alaska Fairbanks.
- Luk, C-H, 1983, Added Mass and Damping for Ice Floes by Long Water Wave Theory, *Proceedings of the Offshore Technology Conference*, OTC 4458, pp. 133-142.
- Lyon, W., 1967, Under-surface Profiles of Sea Ice Observed by Submarine, *Physics of Snow and Ice*, Vol. I, pp 707-711.
- Määttänen, M, 1981, Experiences with Vibration Isolated Lighthouses, *POAC 81*, Vol. 1, pp 491-501.
- Määttänen, M, 1983, Dynamic Ice-structure Interaction during Continuous Crushing, *CRREL Report*, No. 83-5.
- Marcellus, R. W. and T. B. Morrison, 1982, Ice Design Statistics for the Canadian Beaufort Sea, *Beaufort Sea Environmental Impact Statement (EIS)*, Report No. RWI 15. Calgary: Pallister Resource Management Ltd.
- Maykut, G. A., 1986, The Surface heat and mass balance, *The Geophysics of Sea Ice*, University of Washington Press, pp 395-463.
- McPhee, M. G., 1982, Sea Ice Drag Laws and Simple Boundary Layer Concepts, Including Application to Rapid Melting, USA Cold Regions Research and Engineering Laboratory, *CRREL Report* 82-4, 52pp.
- Mellor, M., 1983, Mechanical Behavior of Sea Ice, *CRREL*, Monograph 83-1.
- Mellor, M., 1986, Mechanical Behavior of Sea Ice, *The Geophysics of Sea Ice*, edited by N. Untersteiner, University of Washington Press, pp 165-282.

- Mills, D.A., 1972, On Waves in a Sea Ice Cover, Horace Lamb Centre for Oceanographic Research, Flinders University, Bedford Park, Research Paper 53, 64 p.
- Pande, G. N. and O. C. Zienkiewicz, 1982, Soil Mechanics—Transient and Cyclic Loads, A Wiley-Interscience Publication, Dept. of Civil Engineering, University of Wales, Swansea.
- Parmeter, R. R. and M. D. Coon, 1972, Model of Pressure Ridge Formation in Sea Ice, *J. of Geophysical Research*, 77(33), pp 6565-6575.
- Prodanovic, A., 1979, Geotechnical Criteria, *Technical Seminar on Alaskan Beaufort Sea Gravel Island Design*, EXXON, 1979.
- Prodanovic, A., 1981, Upper Bounds of Ridge Pressure on Structure, *Proceedings of The Sixth International Conference on Port and Ocean Engineering under Arctic Conditions*, Vol. III, pp. 1288-1302.
- Riska, K and R. Frederking, 1987, Ice Load Penetration Modelling, *Port and Ocean Engineering under Arctic Conditions*, Edited by W. M. Sackinger and M. O. Jeffries, Vol. 1, pp 317-327.
- Sackinger, W. M., 1985, Engineering and Environmental Factors in the Alaskan Offshore, *Arctic Ocean Engineering for the 21st Century*, pp 44-49.
- Sackinger, W. M. and M. O. Jeffries, 1987, Ice Island Characterization, Dec. 83–Sept. 87, Geophysical Institute, University of Alaska Fairbanks.
- Sackinger, W. M. and M. Yan, 1986, Generation and Movement of Ice Island near the Canadian Archipelago, *Proc. of the Arctic Oceanography Conference*, Bay ST. Louis, Ms., pp 44-99.
- Sackinger, W. M. and M. O. Jeffries, 1986, Arctic Ice Island and Sea Ice Movements and Mechanical Properties, 12th Quarterly Report (1 July - 30 September, 1986), U. S. Department of Energy, Morgantown Energy Technology Centre, Western Virginia.
- Sackinger, W. M., M. O. Jeffries, Fucheng Li and Mingchi Lu, 1991, Ice Island Creation, Drift, Recurrences, Mechanical Properties and Interactions with Arctic Offshore Oil Production Structures, *Final Report*, the Geophysical Institute, University of Alaska Fairbanks.

- Sackinger, W. M. and W. J. Stringer, 1983, Arctic Ice Island and Sea Ice Movements and Mechanical Properties, First Quarterly Report, Univ. of Alaska-Fairbanks, 122 pp.
- Sanderson, T. J. O., 1984, Theoretical and Measured Ice Forces on Wide Structures, *IAHR Ice Symposium*, Hamburg, Vol. 4, pp. 151-207.
- Sanderson, T. J. O., 1988, Ice Mechanics Risks to Offshore Structures, *BP Petroleum Development Ltd, London*.
- Sanderson, T. J. O. and A. J. Child, 1986, Ice Loads on Offshore Structures: the Transition from Creep to Fracture, *Cold Regions Science and Technology 12*, pp. 157-161.
- Sinha, N. K., 1983a, Creep Model of Ice for Monotonically Increasing Stress, *Cold Regions Science and Technology 8*, pp 25-33.
- Sinha, N. K., 1983b, Field Test on Rate Sensitivity of Vertical Strength and Deformation of First-year Columnar-grained Ice, *Proceedings of Port and Ocean Engineering under Arctic Conditions' 83*, Vol. I, pp 231-242.
- Tabata, T. and K. Tusima, 1981, Friction Measurements of Sea Ice on Some Plastics and Coatings, *Proceedings of the 6th International Conference on Port and Ocean Engineering under Arctic Conditions*, July 27-31, 1981, Quebec, Canada, Vol. 1, pp. 526-535.
- Takeuchi, T. and L. H. Shapiro, 1989, The Deformation of Floating Ice Sheets of Variable Thickness under in-plane Compressive Loading, *Proceedings of the 10th International Conf. on Port and Ocean Engineering under Arctic Conditions*, Lulea, Sweden, Vol. I, pp 385-407.
- Takeuchi, T., 1990, Deformation of Floating Ice of Variable Thickness under In-plane Compressive Loading, *M. S. Thesis*, University of Alaska Fairbanks, Fairbanks.
- Voelker, R. P., F. W. DeBord, F. A. Geisel, J. L. Coburn and K. E. Dane, 1981, Winter 1981 Trafficability Tests of the USCGC Polar Sea, Vol. II, Environmental Data, *Report to Maritime Administration, Arctec, Inc.*, Columbia, Md.
- Wadhams, P., 1986, The Second Ice Zone, *The Geophysics of Sea Ice*, University of Washington Press, pp 825-992.

- Wang, Y. S., 1979, Crystallographic Studies and Strength Tests of Field Ice in the Alaskan Beaufort Sea, *Proceedings of the 5th Conference on Port and Ocean Engineering under Arctic Conditions*, pp. 651-665.
- Weeks, W. F. and M. Mellor, 1984, Mechanical Properties of Ice in the Arctic Seas, *Arctic Technology and Policy*, pp 235-259.
- Weeks, W. F. and S. F. Ackley, 1986, The Growth, Structure, and Properties of Sea Ice, *The Geophysics of Sea Ice*, edited by N. Untersteiner, University of Washington Press, pp 9-164.
- Yan, M., 1986, The Relationship between Ice Island Movement and Weather Condition, *M. S. Thesis*, University of Alaska-Fairbanks.
- Yu, Y. S. and F. Visell, 1961, Surface Waves Generated by an Oscillatory Circular Cylinder on Water of Finite Depth, *J. Fluid Mechanics*, Vol. II, pp. 529-551.
- Zienkiewicz, O. C., R. W. Lewis and K. G. Stagg, 1978, Numerical Method in Offshore Engineering, *A Wiley-Interscience Publication*, University of Wales, Swansea.

APPENDIX

Computer Calculation Programs

A.1 Fortran Programs

```

PROGRAM FORCE
PARAMETER (M1=5, M2=6, N=140)
dimension x(N),p(N),XX(2,N),AA(M1),S(M1,M2)
do i=1,N
  x(i)= float(i-1)
  p(i)=(150.0*(x(i))-(x(i))*(x(i)))**0.25
enddo
open(unit=93,status='new',file='for093.dat')
write(93,8)
do 30 i=1,N
write(93,2) x(i),p(i)
2  format(3x,2E11.4)
8  format(9x,'X',10x,'P',/)
30 continue
close(93)
DO 40 J=1,N
XX(1,J)=X(J)
XX(2,J)=P(J)
40 CONTINUE
CALL LSTM(N,M1,M2,XX,AA,S,FAIL)
PRINT *, (AA(L), L=1,M1)
WRITE (94, *) (AA(L), L=1,M1)
stop
end

```

```

SUBROUTINE LSTM(N,M1,M2,X,A,S,FAIL)
DIMENSION X(2,N),A(M1),S(M1,M2)
M=M1-1
DO 5 I=1,M1
DO 5 J=1,M2
5  S(I,J)=0.0
S(1,1)=N
DO 6 J=1,N
6  S(1,M2)=S(1,M2)+X(2,J)
DO 7 I=2,M1
I1=I-1
MI=M1+I-2
DO 7 J=1,N
S(I,1)=S(I,1)+X(1,J)**I1
S(M1,I)=S(M1,I)+X(1,J)**MI
7  S(I,M2)=S(I,M2)+X(1,J)**I1*X(2,J)

```

```

DO 8 J=2,M
DO 8 I=J,M
8 S(I,J)=S(I+1,J-1)
DO 9 I=1,M
I1=I+1
DO 9 J=I1,M1
9 S(I,J)=S(J,I)
CALL GS(M1,S,A,M2,FAIL)
RETURN
END
SUBROUTINE GS(N,A,X,N1,FAIL)
DIMENSION A(N,N1),X(N)
DO 11 K=1,N
DO 5 I=K,N
IF (A(I,K).EQ.0.0) GO TO 6
I0=I
GO TO 7
6 CONTINUE
FAIL=-1.
RETURN
7 IF (I0.EQ.K) GO TO 9
DO 8 J=K,N1
T=A(K,J)
A(K,J)=A(I0,J)
8 A(I0,J)=T
9 K1=K+1
DO 10 J=K1,N1
10 A(K,J)=A(K,J)/A(K,K)
DO 11 I=K1,N
DO 11 J=K1,N1
11 A(I,J)=A(I,J)-A(I,K)*A(K,J)
X(N)=A(N,N1)
NI=N-1
DO 12 K=1,N1
K1=NI-K+1
X(K1)=A(K1,N1)
K2=K1+1
DO 12 J=K2,N
12 X(K1)=X(K1)-A(K1,J)*X(J)
FAIL=0.
RETURN
END

```

```

program lu
parameter (n=100, x0=0.0, x2=80.0, nn=50)

C -----
C   the following parameters are for the mass M
C -----
c   parameter (c1=4.0D-02,c2=-2.05D-03,c3=-0.8D-04)
c   parameter (c1=0.1225,c2=-2.05D-03,c3=-0.8D-04)
c   parameter (c1=0.25,c2=-2.05D-03,c3=-0.8D-04)
c   parameter (c1=0.3249,c2=-2.05D-03,c3=-0.8D-04)
c   parameter (c4=1.05D-06,c5=-6.8D-09,c6=1.78D-11)
C -----
C   the following parameters are for the mass Me
C -----
c   parameter (c1=4.0D-02,c2=-1.52D-03,c3=-0.59D-04)
c   parameter (c1=0.1225,c2=-1.52D-03,c3=-0.59D-04)
c   parameter (c1=0.2304,c2=-1.52D-03,c3=-0.59D-04)
c   parameter (c1=0.25,c2=-1.52D-03,c3=-0.59D-04)
c   parameter (c4=7.77D-07,c5=-5.04D-09,c6=1.32D-11)

implicit real*8 (a-h, o-z)
do 18 ii=1, nn
  xl= (x2-x0)/float(nn)*float(ii)
C -----
C   the hh is the length of the integral step.
C -----
  hh=(x1-x0)/float(n*2)
C -----
C   here we use Simpson integral formular
C -----
  tt=0.0E+00
  do 1 I=1,n-1
    h1=hh*float(2*I-1)+x0
    h2=hh*float(2*I)+x0
    tt= tt + 4.0E+00*efx(h1,c1,c2,c3,c4,c5,c6)
    $   + 2.0E+00*efx(h2,c1,c2,c3,c4,c5,c6)
  1  continue
    h3=x0+hh*float(2*n-1)
    tt = (tt + efx(x0,c1,c2,c3,c4,c5,c6) +
    $     4.0E+00*efx(h3,c1,c2,c3,c4,c5,c6) +
    $     efx(x1,c1,c2,c3,c4,c5,c6)) *hh/3.0E+00
  11  print 11, x0,x1,tt
    $   format(1x,'x0=', F6.2, 2h,
    $         'x1=', F6.2, 2h, 'time=', F10.5)
  18  continue
  stop
end

C -----END OF THE DRIVER-----
C -----FUNCTION F(x)-----
double precision function efx(x,c1,c2,c3,c4,c5,c6)
implicit real*8 (a-h, o-z)
efx=(c1+c2*x+c3*x**2.0+c4*x**3.0+c5*x**4.0+c6*x**5.0)**(-0.5)
return
end
C -----END OF F(x)-----

```


A.2 Adina Programs

C This is for the results of $\Delta t/t = 0.5$,
 C fixed B.C., constant E, ice/structure located
 C in the central region and $t_1/t = 1$, in
 C which each important command is followed by
 C a note.

```

C RUN ADINA
$ADINAINSM
DATABASE CREATE
C INPUT DEVICE # AND SYSTEM #
CONTROL BAUDRATE=9600 DEVICE=50 SYSTEM=1
C PEN CHOSEN
COLORS
C TITLE OF THE PROGRAM
HEADING S='3D ICE STRUCTURE INTERACTION MODEL'
C BOUUDARY CONDITION FOR OUTPUTS
MASTER IDOF=000111 REACTION=YES
KINEMATICS DISP=SMALL STRAIN=SMALL
ANALYSIS TYPE=STATIC
C OUTPUTS FOR EVERYTHING INCLUDING STRESSES, DISP., AND
C FORCES IN THREE DIMEN. FROM EACH NODE.
PRINTOUT MAX
C NODES INPUT IN GLOBAL SYSTEM
COORDINATES
ENT NODE  X  Y  Z
1  0  0  0
2  12.0  0  0
3  24  0  0
4  25.0  0  0
5  26  0  0
6  38  0  0
7  50  0  0
8  50  12.5  0
9  50  25  0
10  50  37.5  0
11  50  50  0
12  38.0  50  0
13  26.0  50  0
14  25.0  50  0
15  24  50  0
16  12.0  50  0
17  0  50  0
18  0  37.5  0
19  0  25  0
20  0  12.5  0
21  12  12.5  0
22  24  12.5  0

```

23	25	12.5	0	75	26	0	13
24	26	12.5	0	76	38	0	13
25	38	12.5	0	77	50	0	13
26	38	25	0	78	50	12.5	13
27	38	37.5	0	79	50	25	13
28	26	37.5	0	80	50	37.5	13
29	25	37.5	0	81	50	50	13
30	24	37.5	0	82	38	50	13
31	12	37.5	0	83	26	50	13
32	12	25	0	84	25	50	13
33	24	25	0	85	24	50	13
34	25	25	0	86	12	50	13
35	26	25	0	87	0	50	13
36	0	0	16	88	0	37.5	13
37	12	0	16	89	0	25	13
38	24	0	16	90	0	12.5	13
39	25	0	16	91	12	12.5	13
40	26	0	16	92	24	12.5	13
41	38	0	16	93	25	12.5	13
42	50	0	16	94	26	12.5	13
43	50	12.5	16	95	38	12.5	13
44	50	25	16	96	38	25	13
45	50	37.5	16	97	38	37.5	13
46	50	50	16	98	26	37.5	13
47	38	50	16	99	25	37.5	13
48	26	50	16	100	24	37.5	13
49	25	50	16	101	12	37.5	13
50	24	50	16	102	12	25	13
51	12	50	16	103	24	25	13
52	0	50	16	104	25	25	13
53	0	37.5	16	105	26	25	13
54	0	25	16	106	0	0	10
55	0	12.5	16	107	12	0	10
56	12	12.5	16	108	24	0	10
57	24	12.5	16	109	25	0	10
58	25	12.5	16	110	26	0	10
59	26	12.5	16	111	38	0	10
60	38	12.5	16	112	50	0	10
61	38	25	16	113	50	12.5	10
62	38	37.5	16	114	50	25	10
63	26	37.5	16	115	50	37.5	10
64	25	37.5	16	116	50	50	10
65	24	37.5	16	117	38	50	10
66	12	37.5	16	118	26	50	10
67	12	25	16	119	25	50	10
68	24	25	16	120	24	50	10
69	25	25	16	121	12	50	10
70	26	25	16	122	0	50	10
71	0	0	13	123	0	37.5	10
72	12	0	13	124	0	25	10
73	24	0	13	125	0	12.5	10
74	25	0	13	126	12	12.5	10

127	24	12.5	10
128	25	12.5	10
129	26	12.5	10
130	38	12.5	10
131	38	25	10
132	38	37.5	10
133	26	37.5	10
134	25	37.5	10
135	24	37.5	10
136	12	37.5	10
137	12	25	10
138	24	25	10
139	25	25	10
140	26	25	10

C INPUT ELEMENTS, GROUP, CALCULA. METHOD.

EG N=1 SOLID DISP=SMALL STRAINS=SMALL MAT=1 RSINT=2 TINT=2
ENODE

ENT	EL	N1	N2	N3	N4	N5	N6	N7	N8
1	43	60	41	42	78	95	76	77	
2	44	61	60	43	79	96	95	78	
3	45	62	61	44	80	97	96	79	
4	46	47	62	45	81	82	97	80	
5	47	48	63	62	82	83	98	97	
6	48	49	64	63	83	84	99	98	
7	49	50	65	64	84	85	100	99	
8	50	51	66	65	85	86	101	100	
9	51	52	53	66	86	87	88	101	
10	66	53	54	67	101	88	89	102	
11	67	54	55	56	102	89	90	91	
12	56	55	36	37	91	90	71	72	
13	57	56	37	38	92	91	72	73	
14	58	57	38	39	93	92	73	74	
15	59	58	39	40	94	93	74	75	
16	60	59	40	41	95	94	75	76	
17	61	70	59	60	96	105	94	95	
18	62	63	70	61	97	98	105	96	
19	63	64	69	70	98	99	104	105	
20	64	65	68	69	99	100	103	104	
21	65	66	67	68	100	101	102	103	
22	68	67	56	57	103	102	91	92	
23	69	68	57	58	104	103	92	93	
24	70	69	58	59	105	104	94	94	

C THE SECOND GROUP

EG N=2 SOLID DISP=SMALL STRAINS=SMALL MAT=1 RSINT=2 TINT=2
ENODE

ENT	EL	N1	N2	N3	N4	N5	N6	N7	N8
1	78	95	76	77	113	130	111	112	
2	79	96	95	78	114	131	130	113	
3	80	97	96	79	115	132	131	114	
4	81	82	97	80	116	117	132	115	
5	82	83	98	97	117	118	133	132	
6	83	84	99	98	118	119	134	133	

```

7 84 85 100 99 119 120 135 134
8 85 86 101 100 120 121 136 135
9 86 87 88 101 121 122 123 136
10 101 88 89 102 136 123 124 137
11 102 89 90 91 137 124 125 126
12 91 90 71 72 126 125 106 107
13 92 91 72 73 127 126 107 108
14 93 92 73 74 128 127 108 109
15 94 93 74 75 129 128 109 110
16 95 94 75 76 130 129 110 111
17 96 105 94 95 131 140 129 130
18 97 98 105 96 132 133 140 131
19 98 99 104 105 133 134 139 140
20 99 100 103 104 134 135 138 139
21 100 101 102 103 135 136 137 138
22 103 102 91 92 138 137 126 127
23 104 103 92 93 139 138 127 128
24 105 104 93 94 140 139 128 129

```

C MAT PROPERTIES

MAT N=1 ELASTIC E=6E9 NU=0.3 SE OF PLASTIC-MULTILINEAR IN

MAT N=2 ELASTIC E=6E9 NU=0.3 SOTROPIC

EG N=3 SPRING RESULT=FORCE R HARDENING=ISO E=6E9 NU=0.3

PROPERTYSET 1 K=367500 R HARDENING=ISO E=6E9 NU=0.3

PROPERTYSET 2 K=735000

PROPERTYSET 3 K=398125

PROPERTYSET 4 K=61250

PROPERTYSET 5 K=398125

PROPERTYSET 6 K=735000

PROPERTYSET 7 K=367500

PROPERTYSET 8 K=735000

PROPERTYSET 9 K=735000

PROPERTYSET 10 K=735000

PROPERTYSET 11 K=367500

PROPERTYSET 12 K=735000

PROPERTYSET 13 K=398125

PROPERTYSET 14 K=61250

PROPERTYSET 15 K=398125

PROPERTYSET 16 K=735000

PROPERTYSET 17 K=367500

PROPERTYSET 18 K=735000

PROPERTYSET 19 K=735000

PROPERTYSET 20 K=735000

PROPERTYSET 21 K=1470000

PROPERTYSET 22 K=796250

PROPERTYSET 23 K=122500

PROPERTYSET 24 K=796250

PROPERTYSET 25 K=1470000

PROPERTYSET 26 K=1470000

PROPERTYSET 27 K=1470000

PROPERTYSET 28 K=796250

PROPERTYSET 29 K=122500

PROPERTYSET 30 K=796250

PROPERTYSET 31 K=1470000
 PROPERTYSET 32 K=1470000
 PROPERTYSET 33 K=796250
 PROPERTYSET 34 K=122500
 PROPERTYSET 35 K=796250

ENODE

1 1 3 106 3
 2 2 3 107 3
 3 3 3 108 3
 4 4 3 109 3
 5 5 3 110 3
 6 6 3 111 3
 7 7 3 112 3
 8 8 3 113 3
 9 9 3 114 3
 10 10 3 115 3
 11 11 3 116 3
 12 12 3 117 3
 13 13 3 118 3
 14 14 3 119 3
 15 15 3 120 3
 16 16 3 121 3
 17 17 3 122 3
 18 18 3 123 3
 19 19 3 124 3
 20 20 3 125 3
 21 21 3 126 3
 22 22 3 127 3
 23 23 3 128 3
 24 24 3 129 3
 25 25 3 130 3
 26 26 3 131 3
 27 27 3 132 3
 28 28 3 133 3
 29 29 3 134 3
 30 30 3 135 3
 31 31 3 136 3
 32 32 3 137 3
 33 33 3 138 3
 34 34 3 139 3
 35 35 3 140 3

EDATA

ENT EL PROPERTYSET

1	1	6	6
2	2	7	7
3	3	8	8
4	4	9	9
5	5	10	10
6	6	11	11
7	7	12	12
8	8	13	13
		14	14

9 9
10 10
11 11
12 12
13 13
14 14
15 15
16 16
17 17
18 18
19 19
20 20
21 21
22 22
23 23
24 24
25 25
26 26
27 27
28 28
29 29
30 30
31 31
32 32
33 33
34 34
35 35

C BOUNDARY CONDITIONS FOR FIXED

FIXBOUNDARY 123 TYPE=NODE

1/2/3/4/5/6/7/8/9/10/11/12/13/14/15/16/17/

18/19/20/21/22/23/24/25/26/27/28/

29/30/31/32/33/34/35/

FIXBOUNDARY 123 TYPE=NODE

43/44/45/78/79/80/113/114/115/

C LOAD CONDITION AND INPUT METHOD THIS IS FOR T1/1=1

EG N=1

LOAD ELEMENT

9 -1 0.5E6

10 -1 0.5E6

11 -1 0.5E6

12 -1 0.5E6

EG N=2

LOAD ELEMENT

9 -1 0.5E6

10 -1 0.5E6

11 -1 0.5E6

12 -1 0.5E6

ADINA

END

```
C -----  
C The following program is for the display of the  
C finite element mesh.  
C -----
```

```
$ALLOCATE TTA2:  
$ASSIGN TTA2: FOR050  
$ADINAINSMML  
CONTROL BAUDRATE=9600 SYSTEM=1 DEVICE=50  
FRAME HEADING=2  
TEXT SUBFRAME=1121 X=0.5 Y=0.5 A=0,  
STRING='3D FINITE ELEMENT MESH'  
TEXT SUBFRAME=1122 X=0.5 Y=0.5 A=0,  
STRING='ICE-STRUCTURE BOUNDARY CONDITIONS'  
MESH ORIGINAL=1 DEFORMED=0 NODES=0 ELEMENTS=0,  
TEXT=1 AXES=1 SUBFRAME=1121  
MESH ORIGINAL=1 DEFORMED=0 NODES=0 ELEMENTS=0,  
GSCALE=-1 LINES=1 BCODE=ALL SUBFRAME=1122  
PLOT  
$DEASSIGN FOR050  
$DEALLOCATE TTA2:
```

```
C -----  
C The following program is for the display and list  
C of all of output results by ADINA.  
C -----
```

```
$ ALLOCATE TTA2:  
$ ASSIGN TTA2: FOR050  
$ ADINAPLOTSML  
DATABASE OPERATION=CREATE FILE=70  
CONTROL BAUDRATE=9600 SYSTEM=1 DEVICE=50 MODE=BATCH
```

```
FRAME HEADING=2  
EGZ N=A1  
1  
EGZ N=A2  
2  
TEXT SUB=1121 X=0.5 Y=0.5 A=0,  
ST='DEFORMED MESH'  
MESH O=2 DE=0 L=1 S=1121  
MESH O=0 DE=1 G=-1,  
DM=0.1 S=1121  
TEXT SUB=1122 X=0.5 Y=0.5 A=0,  
ST='PRINCIPAL STRESSES'  
MESH O=1 DE=0 G=-1,  
L=1 S=1122  
EVECTOR KIND=1 OUTPUT=PLOT TEXT=YES  
PLOT  
FILE LIST=71  
EINFO NODENUMBERS=NO POINTCOORDINATES=YES  
FILE LIST=6  
FRAME  
MESH ORIGINAL=1 DEFORMED=0 LINES=1  
FILE LIST=72  
EVECTOR KIND=1 OUTPUT=LIST  
FILE LIST=6  
END
```

```
$DEASSIGN FOR050  
$DEALLOCATE TTA2:  
$EXIT
```



```

C-----
C This program plots Sr distributions on the top
C surface of the floe in three-dimension.

      PARAMETER (M=5,N=5)
      DIMENSION SrDAT(M,N)
      DATA SrDAT/-0.9,-1.2,2.6,-1.2,-1.,-1.3,-1.22,2.65,
*      -1.1,-1.,-1.38,-1.22,2.6,-1.16,-1.,-1.3,-1.22,
*      2.65,-1.1,-1.,-0.9,-1.2,2.6,-1.2,-1./
      COMMON WORK(40000)
      CALL RESET ('ALL')
      CALL COMPRS
      CALL SWISSM
      CALL PAGE (11.,8.5)
C SET AXIS PARAMETERS AND ALPHABETS
      CALL INTAXS
      CALL ZAXANG (90.)
      CALL COMPLX
      CALL BASALF ('L/CST')
      CALL MIXALF ('STAND')
C DEFINE 3-D WORK AREA AND AXIS
      CALL AREA2D (10.,6.9)
      CALL SWISSL
      CALL HEADIN (' ',100,1.5,2)
C      CALL HEADIN ('STRESS RATIO $',100,1.5,2)
      CALL RESET ('HEIGHT')
      CALL X3NAME ('(X)$',100)
      CALL Y3NAME ('(Y)$',100)
      CALL Z3NAME ('(Sr)$',100)
      CALL VOLM3D (10.,10.,8.)
C DEFINE 3-D VIEW POINT
      CALL VIEW (-1100.,-1400.,50.)
      CALL GRAF3D (0.0,10.,50.,0.,10.,50.,-3.0,1.,5.)
C SUBROUTINE SORDAT CONTAINS THE CONTOURING DATA
C FOR THIS PARTICULAR PLOT
C?      CALL SORDAT (SrDAT)
C DEFINE THE SURFACE VIA A MATRIX
      CALL BLSUR
      CALL SURMAT (SrDAT,1,M,1,N,0)
      CALL DASH
      XDEL=0.
      DO 231 I=1,3
      CALL BSHIFT (XDEL,0.)
C DRAW BEDPOST EFFECT
      XDEL=XDEL+.005

```

```

231 CONTINUE
    CALL RESET ('DOT')
    CALL RESET ('BSHIFT')
C   ENTER GRFITI LOOP AND DEFINE 2-D PLOT
    CALL GRFITI (0.,0.,0.0,1.,0.,0.0,0.,1.,0.)
    CALL INTAXS
    CALL AREA2D (10.,10.)
    CALL GRAF (0.,100.,500.,0.,100.,500.)
C   CONTOURING IS OPTIONAL FEATURE
C   SET CONTUR PARAMETERS
    CALL BCOMON (40000)
c!!!   CALL CONANG (90.)
    CALL FRAME
    CALL HEIGHT (.3)
C?    CALL CONTUR (2,'LABELS','DRAW')
C   END GRFITI LOOP
    CALL END3GR(0)
    CALL ENDPL (0)
    CALL DONEPL
C-    RETURN
    STOP
    END

C-----
C This program plots Sr as a function of X in the middle
C area of Y direction in the ice floe model
C
    INCLUDE 'UACN:[SXLIB.POSTSCRIPT]PS.FOR'
    PARAMETER (NX=7,NC=3,NF=4)
    DIMENSION X(NX),Y1(NX),Y2(NX),Y3(NX),Y4(NX),
*           Y21(NX),Y22(NX),Y23(NX),Y24(NX),Y31(NX),
*           Y32(NX),Y33(NX),Y34(NX),Y41(NX),Y42(NX),
*           Y43(NX),Y44(NX)
    DATA X/0.0,12.0,24.5,25.0,25.5,38.0,50.0/
    DATA Y1/-1.46,-1.36,2.06,2.6,2.0,-1.16,-1.0/
    DATA Y2/-1.56,-1.94,-1.83,-1.73,-1.84,-1.98,-1./
    DATA Y3/-1.7,-2.3,-6.4,-6.8,-6.3,-2.7,-1.1/
c   DATA Y4/1.,1.,1.,1.,1.1,3.2,3.8/
    DATA Y21/-1.38,-1.2,-1.2,-1.2,-1.27,-1.24,-1.0/
    DATA Y22/-1.38,-1.1,-1.1,-1.2,-1.2,-1.2,-1.1/
    DATA Y23/-1.4,-1.19,-1.2,-1.16,-1.18,-1.19,-1.1/
c   DATA Y24/1.,1.,1.,1.,1.1,3.2,3.8/
    DATA Y31/-1.4,-1.2,-1.4,-1.4,-1.4,-1.6,-1.0/
    DATA Y32/-1.4,-1.2,-1.4,-1.4,-1.4,-1.6,-1.0/
    DATA Y33/-1.4,-1.12,-1.2,-1.2,-1.2,-1.6,-1.0/
c   DATA Y34/1.1,3.2,3.8,1.,1.,1.,1./
    DATA Y41/-1.4,-1.2,-1.4,-1.4,-1.4,-1.6,-1.0/
    DATA Y42/-1.4,-1.2,-1.4,-1.4,-1.4,-1.6,-1.0/
    DATA Y43/-1.4,-1.12,-1.2,-1.2,-1.2,-1.6,-1.0/
c   DATA Y44/1.1,3.2,3.8,1.,1.,1.,1./

```

```

OMIN=0.0
OMAX=50.0
YMIN=-7.0
YMAX=3.0
OSTEP=12.5
YSTEP=2.0
CALL COMPRS
C CALL UAFPS('PLOT2.PS',10,3,0.01)
CALL PAGE(8.5,11.)
C CALL HWROT('AUTO')
CALL NOBRDR
CALL DUPLX
CALL XAXANG(90.)
CALL YAXANG(0.)
OAXIS=2.0
XAXIS=2.50
CALL THKFRM(0.015)
DO 1004 IE=1,4
  if (ie.eq.1) CALL PHYSOR(1.90,2.20)
  if (ie.eq.2) CALL PHYSOR(5.50,2.20)
  if (ie.eq.3) CALL PHYSOR(1.90,6.10)
  if (ie.eq.4) CALL PHYSOR(5.5,6.10)
    CALL AREA2D(OAXIS,XAXIS)
      call height(0.1)
c call mx5alf('greek','%')
  IF (IE.EQ.1) THEN
    CALL XNAME(' X (m) ',100)
    CALL YNAME(' Sr ',100)
  ELSEIF (IE.EQ.2) THEN
    CALL XNAME(' X (m) ',100)
    CALL YNAME(' Sr ',100)
  ELSEIF (IE.EQ.3) THEN
    CALL XNAME(' X (m) ',100)
    CALL YNAME(' Sr',100)
  ELSEIF (IE.EQ.4) THEN
    CALL XNAME(' X (m) ',100)
    CALL YNAME(' Sr',100)
  ENDIF
  if (ie.eq.1) then
    call height(0.12)
    CALL messag('Sr is a function of X$',100,1.8,7.5)
      call messag(' Figure 4 ',100,2.1,-1.1)
      call height(0.1)
    call messag('Variable thickness $',100,0.5,2.60)
c call messag(' GPa $',100,'abut','abut')
  endif
  if (ie.eq.2) then
c call messag('Uniform thickness $',100,0.5,2.60)
c call messag(' GPa $',100,'abut','abut')
  endif
  if (ie.eq.3) then
    call messag('Uniform thickness $',100,0.5,2.60)

```

```

C          call realno(e,1,'abut','abut')
c          call messag(' GPa $',100,'abut','abut')
endif
if (ie.eq.4) then
call messag('Uniform thickness $',100,0.5,2.60)
c          call messag(' GPa $',100,'abut','abut')
endif
C          CALL MIXALF('INSTRU')
c          CALL ANGLE(90.)
          CALL XTICKS(5)
          CALL YTICKS(5)
if (ie.eq.1) then
          CALL GRAF(OMIN,OSTEP,OMAX,YMIN,YSTEP,YMAX)
          CALL FRAME
endif
if (ie.eq.2) then
          CALL GRAF(OMIN,OSTEP,OMAX,YMIN,YSTEP,YMAX)
          CALL FRAME
endif
if (ie.eq.3) then
          CALL GRAF(OMIN,OSTEP,OMAX,YMIN,YSTEP,YMAX)
          CALL FRAME
endif
if (ie.eq.4) then
          CALL GRAF(OMIN,OSTEP,OMAX,YMIN,YSTEP,YMAX)
          CALL FRAME
endif
call height(0.07)
CALL LINE$P(2.2)
CALL LINES('Top',ILEGN,1)
CALL LINES('Middle',ILEGN,2)
CALL LINES('Bottom',ILEGN,3)
XW=XLEGND(ILEGN,3)
YW=YLEGND(ILEGN,3)
CALL LEGLIN
CALL MYLEGN('POSITIONS',9)
          IF (IE.EQ.1) THEN
                                CALL CURVE(X,Y1,NX,0)
                                CALL DOT
                                CALL CURVE(X,Y2,NX,0)
                                CALL DASH
                                CALL CURVE(X,Y3,NX,0)
c                                CALL CHNDSH
c                                CALL CURVE(X,Y4,NX,0)
c                                CALL RESET ('CHNDSH')
                                call reset ('dash')
          ENDIF
          IF (IE.EQ.2) THEN
                                CALL CURVE(X,Y21,NX,0)
                                call dot
                                CALL CURVE(X,Y22,NX,0)
                                call dash
                                CALL CURVE(X,Y23,NX,0)

```

```

c          call chndsh
          call reset ('dash')
c          CALL CURVE (X, Y24, NX, 0)
          ENDIF
          IF (IE.EQ.3) THEN
          CALL CURVE (X, Y31, NX, 0)
          call dot
          CALL CURVE (X, Y32, NX, 0)
          call dash
          CALL CURVE (X, Y33, NX, 0)
c          call chndsh
c          CALL CURVE (X, Y34, NX, 0)
          call reset ('dash')
          ENDIF
          IF (IE.EQ.4) THEN
          CALL CURVE (X, Y41, NX, 0)
          call dot
          CALL CURVE (X, Y42, NX, 0)
          call dash
          CALL CURVE (X, Y43, NX, 0)
c          call chndsh
c          CALL CURVE (X, Y44, NX, 0)
          call reset ('dash')
          ENDIF
          CALL LEGEND (ILEGN, 5, 1.37, 1.86)
          CALL endgr (0)
1004      CONTINUE
          CALL DONEPL
          STOP
          END

```